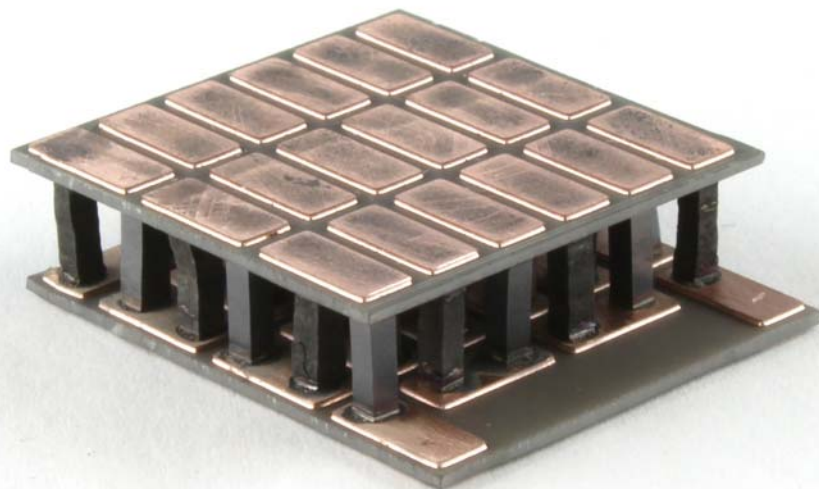




Final report

Thermoelectric On-Board Power Generation from Exhaust Heat





Date: submitted January 31 2018, final version March 31 2018

Town: Bern

Publisher:

Swiss Federal Office of Energy SFOE
Research Programme «Electricity Technology»
CH-3003 Bern
www.bfe.admin.ch

Agent:

Empa, Materials for Energy Conversion & Automotive Powertrain Technologies
Überlandstrasse 129, 8600 Dübendorf
<http://www.empa.ch/>

Autoneum Management AG
Schlosstalstrasse 43, 8406 Winterthur
<http://www.autoneum.com/>

Georg Fischer Automotive AG
Amsler-Laffonstrasse 9, 8200 Schaffhausen
<http://www.georgfischer.com/>

Author:

Dr. Yinglu Tang, Empa, yinglu.tang@empa.ch
Daniel Landmann, Empa, daniel.landmann@empa.ch
Benjamin Kunz, Empa, benjamin.kunz@empa.ch
Daniel Widner, Empa, daniel.widner@empa.ch
Renato Huber, Empa, renato.huber@empa.ch
Dr. Peter Rickhaus, Empa, peter.rickhaus@empa.ch
Remo Widmer, Empa, remo.widmer@empa.ch
Dr. Eduardo Cuervo Reyes, Empa, eduardo.cuervoreyes@empa.ch
Thibaut Durand, Empa, thibaut.durand@empa.ch
Jimmy Hu, Empa, jimmy.hu@empa.ch
Dr. Yujun Liao, Empa, Yujun.Liao@empa.ch
Ermanno Lo Schiavo, Autoneum, ermanno.loschiavo@autoneum.com
Michael Hauenstein, Autoneum, michael.hauenstein@autoneum.com
Cyril Rovath, Autoneum, cyril.rovath@autoneum.com
Christian Graf, Georg Fischer, christian.graf@georgfischer.com
Ilias Papadimitriou, Georg Fischer, ilias.papadimitriou@georgfischer.com
Dr. Panayotis Dimopoulos Eggenschwiler, Empa, panayotis.dimopoulos@empa.ch
Dr. Corsin Battaglia, Empa, corsin.battaglia@empa.ch

SFOE head of domain: Michael Moser, michael.moser@bfe.admin.ch

SFOE programme manager: Roland Brüniger, roland.brueeniger@brueniger.swiss

SFOE contract number: SI/501310-01

The authors of this report bear the entire responsibility for the content and for the conclusions drawn therefrom.

Swiss Federal Office of Energy SFOE

Mühlestrasse 4, CH-3063 Ittigen; postal address: CH-3003 Bern
Phone +41 58 462 56 11 · Fax +41 58 463 25 00 · contact@bfe.admin.ch · www.bfe.admin.ch



Contents

Summary/Zusammenfassung/Résumé.....	4
Executive Summary	5
Work undertaken and findings obtained	9
1 High-throughput materials synthesis.....	9
1.1 Install high-throughput synthesis equipment.....	9
1.2 Establish baseline for p-type Half-Heusler with zT near unity.....	11
1.3 Establish baseline for n-type Half-Heusler with zT near unity.....	13
2 Streamline module fabrication.....	16
2.1 Develop scalable module platform.....	16
2.2 Development of net shape manufacturing technique.....	26
2.3 Modelling assisted thermoelectric module design.....	28
2.4 Module test bench upgrades.....	37
3 Thermal design and vehicle integration.....	38
3.1 Module integration into exhaust gas manifold.....	38
3.2 Design and construction of heat exchanger for integration after exhaust gas manifold and impact on engine performance.....	40
3.3 Module integration into heat exchanger downstream of exhaust gas manifold and the related thermal management and packaging space assessment of total exhaust gas system.....	50
3.4 Design water cooling circuit.....	52
4 Evaluation and validation.....	52
4.1 Adaptation of engine or car test stand system, performance evaluation under standard driving cycles, energy balance assessment for thermoelectric system integrated into exhaust gas manifold.....	52
4.2 Adaptation of engine or car test stand system, performance evaluation under standard driving cycles, energy balance assessment for thermoelectric system integrated downstream of exhaust gas manifold.....	56
4.3 Comparison of performance of thermoelectric system integrated into exhaust manifold and downstream of exhaust manifold	62
Outlook	63
Acknowledgements	64
References.....	64



Summary

Thermoelectric materials enable the direct conversion of heat flux into electric energy. The aim of this project was the development of Half-Heusler thermoelectrics for on-board electric power generation from exhaust heat generated by internal combustion engines by developing all necessary steps for establishing a technological platform that bridges materials research and application. Half-Heusler materials are particularly promising thermoelectrics as they are based on abundant, non-toxic elements, combine thermal stability with mechanical robustness and demonstrate respectable performance in the relevant temperature range.

Zusammenfassung

Thermoelektrische Materialien ermöglichen die direkte Umwandlung von Wärmeflüssen in elektrische Energie. Ziel dieses Projektes war die Entwicklung von Halb-Heusler Thermoelektrika zur On-Board Stromgewinnung durch die Rückgewinnung der Energie in der Abgaswärme von Verbrennungsmotoren. Halb-Heusler Thermoelektrika sind speziell für diese Anwendung geeignet, da sie auf häufig vorkommenden und nicht giftigen Elementen basieren, thermische Stabilität mit mechanischer Robustheit verbinden und hohe Wirkungsgrade in den relevanten Temperaturbereichen erreichen.

Résumé

Les matériaux thermoélectriques permettent la conversion directe de flux de chaleur en énergie électrique. Le but de ce projet était le développement de matériaux thermoélectriques du type semi-Heusler pour des applications de récupération d'énergie produite par des moteurs à combustion interne en développant toutes les étapes nécessaires pour établir une plateforme technologique qui lie la recherche de matériaux à l'application. Les matériaux semi-Heusler représentent une classe de matériaux particulièrement prometteuse pour ces applications, puisque elle se compose d'éléments abondants, non-toxiques, possédant une haute stabilité thermique, des propriétés mécaniques robustes et a démontré des performances respectables dans les gammes de températures pertinentes.



Executive Summary

Traditional on-board power generation is highly inefficient. 60-80% of the chemical energy supplied to an internal combustion engine is ultimately converted to heat. Only the remaining 20-40% is converted into mechanical energy, which is used partially to generate on-board electrical power. Typically, 200 W of electrical power need to be generated on-board to supply the different electric functions in a vehicle. Currently used alternators have efficiencies around 70%. In order to deliver the electrical energy demanded they consume in average 285 W. These are generated by the engine. Taking into account the engine efficiencies of 20-40%, additional fuel energy of roughly 900 W is required. This translates into an additional fuel consumption of 0.08 l/h (respectively an increase of 1.5 – 3.0 % of the fuel consumption of a 5.5 l/100 km vehicle), which could in principle be eliminated by thermoelectrics.

Waste heat recovery from internal combustion engines represents an ideal test bed for Half-Heusler thermoelectrics.

- Combustion engines provide a strong heat source in the temperature range where Half-Heuslers perform optimally.
- The availability of the on-board engine cooling system allows maximization of the heat flux across the thermoelectrics.
- The inefficiency of traditional on-board power generation provides a multiplicative leverage that is expected to significantly improve the overall energy balance.
- Competing waste heat recovery processes such as Rankine cycles are too complex for on-board systems.
- Increasingly stringent CO₂ regulations result in pressure on manufacturers to explore alternative concepts.
- Immense energy savings due to the size of the global combustion engine market.

The TEcar project aimed at delivering materials, electrical and thermal design principles for the application of thermoelectric converters for on-board applications. It identifies the power generation potential of Half-Heusler thermoelectrics on exhaust gas streams in the temperature range between 400-800°C under standard driving cycles and reveals opportunities and challenges for industrialization and market introduction. This final report describes the progress made throughout the two-year project supported by the Swiss Federal Office of Energy.

In work package 1, after installation of equipment enabling high-throughput synthesis of Half-Heusler materials at the beginning of the project, baseline processes for the synthesis, processing, and characterization of n-type and p-type Half-Heusler materials with zT values of 0.7 were established. At a very early stage of the project we decided to shift focus on the development of Zr- and Hf-free n-type Half-Heusler material, as a new promising p-type Half-Heusler based on abundant raw materials was reported in literature shortly before the start of the project. Eliminating Zr and Hf from the n-type Half-Heusler reduces the estimated raw materials costs from estimated 221 \$/kg to 14 \$/kg and matches the raw materials cost of the p-type material estimated at 16 \$/kg. Based on a detailed phase diagram analysis of the n-type TiNiSn Half-Heusler system, we were able to demonstrate zT values up to 0.6 and explain the large spread of thermoelectric transport data of the (Ti,Zr,Hf)NiSn Half-Heusler system reported in literature as being due to small fluctuations in Ni content. We also proposed a route to precisely control the Ni content in TiNiSn Half-Heusler materials by identifying stable boundary compositions, an important aspect when scaling synthesis to industrial volumes. This study was accepted for publication in the prestigious scientific journal Energy & Environmental Science.



In work package 2, a scalable module platform was established. Developing a contact scheme that allows brazing of Half-Heusler thermoelectric legs into modules turned out to be a major challenge. We finally developed a contacting and brazing process which provides simultaneously high mechanical stability, high thermal stability, and low contact resistance. The contacting process is currently considered for a patent application. Although not planned in the original proposal, we developed further a three-dimensional numerical multi-physics model of the thermoelectric modules to maximize power output by numerical design. Due to the extremely high current densities in excess of 80 A/cm^2 generated by the Half-Heusler modules at the maximum power point (compare to high-performance silicon photovoltaics generating on the order of 40 mA/cm^2), minimization of ohmic losses was key to reach power output levels in excess of 2 W per 36 legs module at a temperature difference of 575°C . The model was also crucial to match the module architecture to a given set of hot and cold side heat exchanger characterized by their heat transfer coefficients. An important lesson learned is that the optimum module architecture differs significantly depending on whether hot and cold side temperature or heat transfer coefficients are imposed as boundary conditions. Several additive manufacturing approaches were investigated to simplify module manufacturing. At present, the preferred route for module manufacturing remains a subtractive approach, in which the thermoelectrics legs are cut by diamond wire or diamond blade sawing from a sintered pellet and modules are assembled from individual n-type and p-type legs.

In work package 3 and 4, two strategies for integration of the thermoelectric modules into a compact van were investigated and validated. The first strategy consisted in integrating Half-Heusler thermoelectric modules into a water-cooled exhaust gas manifold located on the exhaust side of the engine. The second strategy consisted in integrating the Half-Heusler modules into the heat exchanger mounted downstream of the exhaust after-treatment system. Integration of the thermoelectric modules into the heat exchanger after the exhaust after-treatment system was first simulated within a one-dimensional numerical model to determine exhaust gas mass flow and exhaust gas temperature in steady-state operation at 100 km/h vehicle speed and during a worldwide harmonized light duty vehicle test cycle (WLTC). These data were employed as input for a three-dimensional numerical flow simulation to determine the optimum geometry for the heat exchangers that extract heat from the exhaust gas stream. For the cold side, air cooling was discarded in favour of water cooling to establish a sufficiently high heat flux and temperature gradient. The heat transfer coefficients resulting from this simulation, were introduced as boundary conditions into the three-dimensional numerical model developed for the modules in work package 2 to optimally match module architecture to the heat exchangers. The thermoelectric generator system comprising hot side exhaust gas heat exchangers, up to ten 36 legs thermoelectric modules, water cooling, and various sensor units was built and integrated into a compact van for testing under steady-state conditions at 100 km/h and over the WLTC.

At 100 km/h steady-state driving, an estimated 2200 W of thermal power is extracted from the exhaust gas stream causing a temperature drop of about 60°C along the thermoelectric generator assembly mounted after the exhaust after-treatment system. 700 W of thermal power is estimated to be guided through the thermoelectric modules. Average measured power output from a single module was about 1.5 W or 2.5 kW/m^2 at exhaust gas temperatures corresponding to a vehicle speed of 100 km/h. To compensate for the temperature drop in the exhaust gas of 125°C due to the additional piping, that was introduced between the exhaust after-treatment system and the thermoelectric generator assembly for practical reasons, an exhaust gas mass flow corresponding to 120 km/h was used. Without this correction module output power drops to 0.75 W. This result corresponds well to the values expected from the numerical modelling. Along the WLTC an average uncorrected power output of 0.4 W or 0.7 kW/m^2 is measured.



These values are expected to increase significantly if the thermoelectric generator is integrated closer to the exhaust gas after-treatment system to avoid the temperature drop of the exhaust gas due to the additional piping which converges to 150 °C during the second half of the WLTC. Note that the WLTC duration is 30 min starting from a cold start condition. Consequently this is a very unfavourable test protocol for waste heat recovery systems as the thermoelectric generator mounted after the exhaust after-treatment system hardly reaches sufficient temperatures for efficient waste heat recovery. Steady-state engine dynamometer cycles, such as the world harmonized stationary cycle (WHSC) for heavy duty vehicles prescribing an engine preconditioning step before the start of the cycle (hot start) are more favorable for waste heat recovery. Fuel saving potential was not corrected for the temperature loss due to the additional piping determined for ten 36 legs modules over the WLTC is 0.1%, but reaches 0.5% under high load conditions.

With the help of the numerical modelling tools developed during this project, an estimation of the potential performance improvements can be given. Replacing the Half-Heusler materials developed for the baseline process of this project with the best reported Half-Heusler materials in literature, an increase in power output of 30-40% is expected. Heat transfer coefficients for the hot side heat exchangers may be improved to values $>900 \text{ W/m}^2\cdot\text{K}$. Improved thermal management in the thermoelectric generator assembly to guide a larger fraction of the 2200 W of thermal power extracted from the exhaust gas flow through the thermoelectric modules may yield additional performance gains. Mounting the thermoelectric generator assembly directly after the exhaust gas after-treatment system to eliminate the additional piping will increase the exhaust gas temperatures by 125-150 °C and consequently improve module output power. For the corrected steady-state test at 100 km/h, the output power of the modules increased by a factor of 2. A more detailed study is necessary to determine the correction factor for the transient WLTC. Finally there is sufficient space available in a vehicle for the integration of more than ten 36 legs modules. At an electric output power density of 2.5 kW/m^2 measured in this project, already an area of $30 \times 30 \text{ cm}^2$ would yield an output power of 225 W at a constant speed of 100 km/h in a compact van factoring in improved thermal design. The weight of an individual module with 36 $1.75 \times 1.75 \text{ mm}^2$ legs is 13.5 g, including the weight of the oxidation barrier with 2.5 g. Its total area including optimized leg spacing is 5.7 cm^2 . Thus a total of 158 modules is required to cover an area of $30 \times 30 \text{ cm}^2$ resulting in an additional weight of 2.1 kg (not including cables, heat exchanger, and cooling assembly). The cost for the raw materials of the thermoelectric legs will not exceed 30 \$/kg for such a thermoelectric generator.

Comparable fuel saving potential is predicted for the modules integrated into the water-cooled exhaust manifold. Module output power at steady-state 100 km/h driving was comparable to output power of modules mounted after the exhaust after-treatment system. This indicates that the thermal design of the manifold needs to be significantly improved, such that the modules can operate at higher hot-side temperatures and consequently higher efficiency. Average module power output over the transient WLTC is about twice as high for the modules integrated into the manifold compared to the modules after the exhaust after-treatment system due to reduced thermal inertia closer to the engine.

From the WLTC results it is clear, that waste heat recovery remains primarily an option for vehicles serving long duration operation ideally at high engine loads, such as long distance delivery vehicles, trucks, busses, construction and mining vehicles or ferries and other marine vessels. The results of this project demonstrate that major gains in electric power output are achieved through careful matching of the module architecture to the heat exchanger design. However, optimization of such a coupled system even with the assistance of numerical modelling remains a difficult task due to the many variables involved.



On the materials side, research should focus on improving the medium and low temperature performance of thermoelectric materials based on abundant non-toxic raw materials. At hot side temperatures of up to 200-250 °C, Bi_2Te_3 based materials remain the best performing materials class, followed by PbTe with optimum performance between 300-400 °C. Our temperature measurements on the vehicle show that these temperatures are exceeded during the WLTC, so these materials are not an option without installation of an exhaust bias to control maximum hot side temperature. In addition due to the high cost of Te and toxicity of Pb, these materials are not an option for high volume markets. For hot side temperatures above 500 °C, Co- and Sb-based skutterudites materials have been investigated intensively, but the use of Co is a handicap in view of the increasing demand for Co from the lithium-ion battery industry. Thus Half-Heusler materials remain a very interesting materials class in this temperature range and new compositions may still be discovered. The present project demonstrated the importance of understanding the phase diagram of these materials. The methodology established within this project to analyse the phase diagram of n-type TiNiSn should also be applied to p-type FeNbSb to identify a robust production window. Heusler materials including the Full-Heuslers may also hold the key to extend high zT values to lower temperatures. Two interesting examples are FeVAl Full-Heusler and MgAgSb alloys, which convert to a Half-Heusler structure above 360 °C. The latter material class achieves $zT > 1$ already at temperature of 100 °C. For more details on the potential of these materials classes, the interested reader is referred to the report of a previous SFOE project "Potential of Thermoelectrics for Waste Heat Recovery".

The TEcar project lays the foundation for further steps towards the industrial manufacturing of thermoelectric generators based on Half-Heusler materials. For the assembly of a full-scale fully-integrated thermoelectric generator demonstrator, materials synthesis (arc melting or induction melting) and processing capacities (milling and sintering) need to be increased to kg scale. Cutting of sintered Half-Heusler pellets into individual legs e.g. via diamond wire sawing needs to be parallelized as e.g. in the photovoltaic industry. Pick-and-place technology would be an efficient strategy for the automated assembly of the modules in analogy with printed circuit-board assembly technology. Brazing strategies need to be adapted for higher throughput and additional quality control steps need to be implemented. Encapsulation strategies (e.g. oxidation barrier) and strategies for integration into heat exchanger should also be improved. A fully integrated 200 W thermoelectric generator for integration into a vehicle with an estimated 158 modules with a total of 5688 legs to cover an area of $30 \times 30 \text{ cm}^2$ is thus within reach and would allow a more detailed analysis of the fuel saving potential.

We thank the Swiss Federal Office of Energy for financial support of this project.



Work undertaken and findings obtained

1. High-throughput materials synthesis

1.1 Install high-throughput synthesis equipment

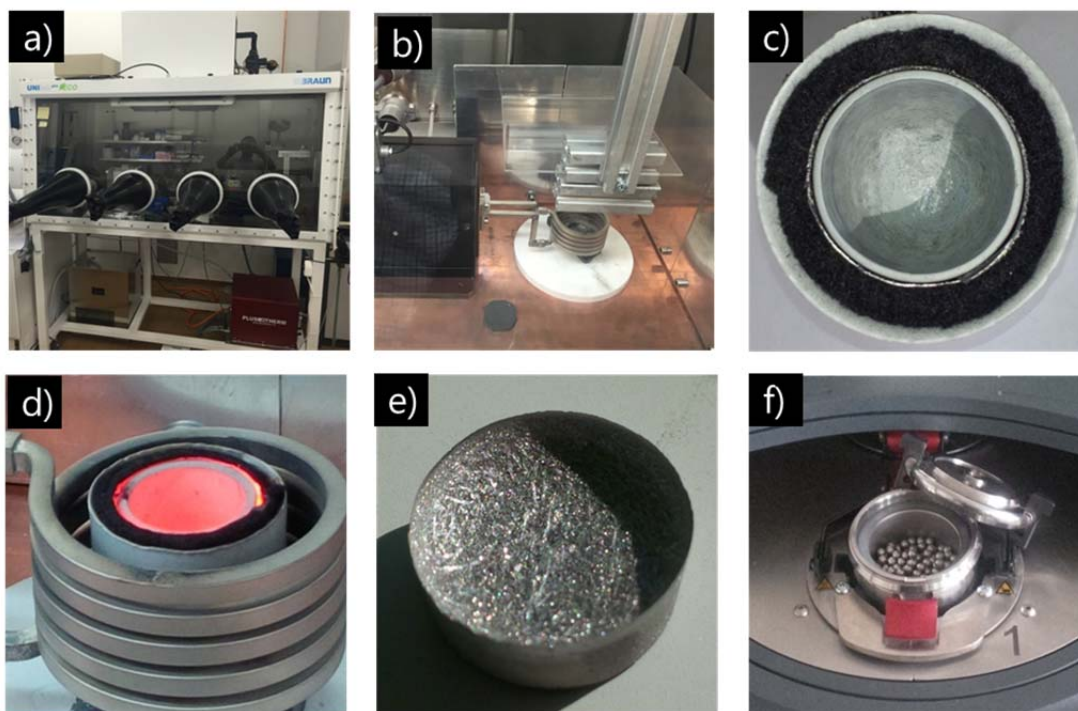


Figure 1: a) Glove box with induction and arc melting furnace for handling and melting of metal powders under inert argon atmosphere, b) induction furnace installed inside of glove box, c) boron nitride crucible embedded into carbon paper and carbon felt to improve heat coupling uniformity, d) crucible with hot melt heated by induction coil, e) Half-Heusler ingot synthesized from the elements by induction melting, f) newly installed automatic ball mill.

For the synthesis of thermoelectric materials from the elements, we designed and installed an induction furnace system located inside a glove box (Fig. 1a and 1b), providing inert argon atmosphere. Inert atmosphere is important when handling elemental metal powders, some of which tend to oxidize rapidly in air. The Swiss company plusTherm, which manufactured the 5kW furnace, offers also large industrial inductive furnace systems up to 600 kW, employed e.g. for metal recycling at a scale of several 100 kg per batch. Induction melting thus offers a direct route to scale the processes developed in this project to industrial scale. A high-precision balance also installed in the glove box allows weighing of samples under inert atmosphere enabling high-throughput synthesis as time consuming transfers between systems and pumping and flushing cycles can be avoided.

We initially experienced difficulties in establishing homogenous heating of the melt inside the crucible. This problem was solved by wrapping the crucible with carbon paper as well as a carbon felt. This ensemble was placed into an outer crucible, which serves as a second containment for the melt in the case of a breakdown of the inner crucible during melting (Fig. 1c and 1d).

A Half-Heusler ingot synthesized from the elements is shown in Fig. 1e. Unmolding of the ingot from the crucible after synthesis turned out to be a major challenge. We tested several crucibles for the synthesis of Half-Heusler materials. Ideally, a crucible minimizes wetting of the melt to facilitate unmolding, offers high thermal shock resistance, and does not react with the melt. If any of these

conditions is not met, it is either difficult to unmold the ingot without breaking the crucible (Fig. 2a and 2d), causes crucible cracking during cooling (Fig. 2b), or destruction of the crucible through reaction with the melt (Fig. 2c). Especially Half-Heusler materials containing high melting point elements such as Ti and Ni which require melting temperatures above 1400°C are challenging. In addition, due to the high reactivity of liquid titanium, it is very difficult to find a suitable crucible that does not react with the melt at such high temperatures. We determined boron nitride crucibles (Fig. 2f) to offer the best trade-off for the synthesis of Half-Heusler materials. Alumina titanate crucibles should be retested with carbon paper and felt, which facilitate heat transfer.

After synthesis and unmolding from the crucible, the resulting Half-Heusler ingot is crushed and milled to micrometer-sized powders in the newly acquired automatic planetary ball mill (Fig. 1f). Milling is an important step towards the fabrication of ceramic thermoelectric elements that minimize the thermal conductivity of the Half-Heusler material. The ball mill vials can be loaded and sealed under inert argon atmosphere avoiding oxidation of the Half-Heusler powder in air. We developed two milling processes, a wet process in isopropanol and a dry process in argon atmosphere, the latter has the advantage that the powder does not need to be dried after milling. A drying process avoiding air exposure was also developed by transferring the powder into a glass bulb equipped with a valve that can be evacuated and heated in connection with a Schlenk line.



Figure 2: Series of tested crucibles after melting and unmolding: a) glassy carbon (melt wetting), b) zirconium oxide (low thermoshock resistance), c) silicon nitride (reacts with n-type melt), d) zirconia coated silica/alumina/silicon carbide composite ceramics (melt wetting), e) aluminum titanate (non uniform heating, to be retested with carbon paper and felt), f) boron nitride (good performance).

In order to avoid the contamination of Half-Heusler alloys by components of the crucible during induction melting, we switched to arc melting (Fig. 3a), in which the reaction of melting material and crucible is minimized by cooling of the copper crucible by a constant water flow. A mini arc melter was integrated in Empa's argon filled glovebox. Sample synthesis is accelerated, as multiple samples can be melted in the same batch and evacuation time between each melting step is shortened to 20 s as compared to 20 min for an arc melting system exposed to air.

In addition, a high temperature Hall measurement system, unique in Switzerland, with maximum temperature up to 800 K was acquired (Fig. 3b) allowing the determination of carrier density and mobility of Half-Heusler alloys. This data is critical to elucidate electronic transport and scattering mechanisms in thermoelectric materials. In combination with a physical property measurements



system system already available at Empa, Hall effect measurements are now possible in a temperature range from below 10 K up to 800 K.

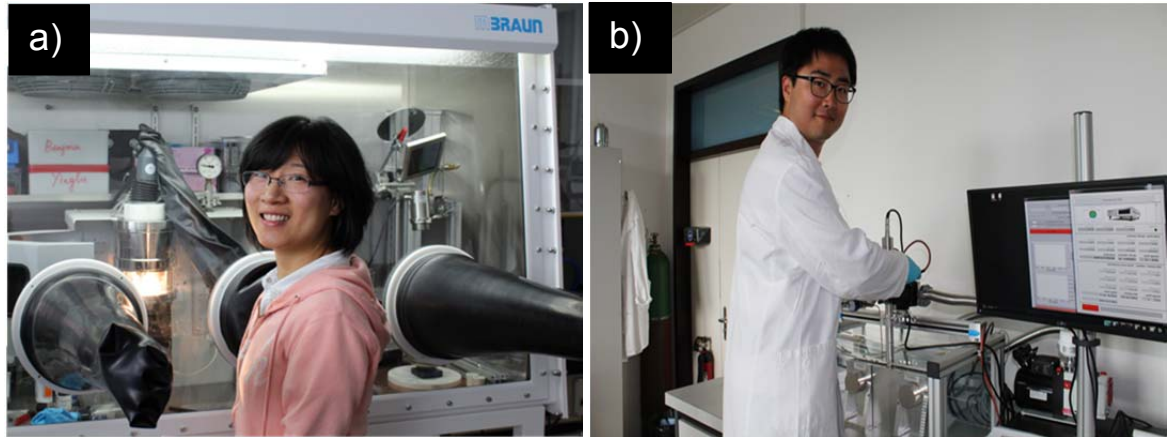


Figure 3: a) Newly installed arc melting furnace inside glovebox for the contamination-free synthesis of Half-Heusler alloys under inert argon atmosphere, b) newly installed high-temperature Hall effect measurement system with maximum temperature up to 800 K for the determination of carrier density and mobility in Half-Heusler alloys.

1.2 Establish baseline for p-type Half-Heusler with zT near unity

Rapid advances in zT for p-type Half-Heusler have been achieved by the thermoelectric community over recent months (see Fig. 4). While n-type Half-Heuslers based on (Hf,Zr)NiSn had already reached zT values above unity in 2013, no p-type Half-Heusler material was available that could match this performance benchmark (less than 0.5 at 627°C for p-type ZrCoSb). During the last few years however, interesting new families of p-type Half-Heusler materials with good performance were discovered. In particular p-type Fe(Nb,Ti)Sb was discovered to exhibit zT values close to one, offering a promising partner to n-type (Hf,Zr)NiSn (Fig. 4). A compound obtained by partially substituting Nb in Fe(Nb,Ti)Sb by V also shows promising performance.

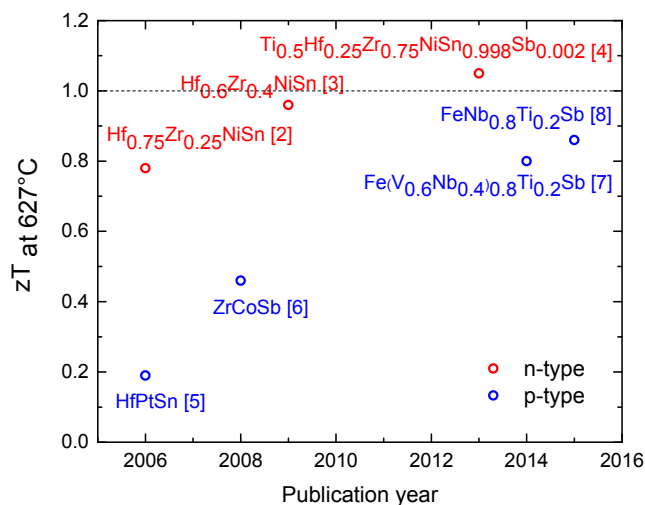


Figure 4: Evolution of zT for n-type and p-type Half-Heuslers over the last ten years¹⁻⁷.



These results are even more remarkable taking into account the fact that these p-type materials do not rely on Zr and Hf. With a price of 86 \$/kg and 608 \$/kg in 2015 respectively⁸, these two elements are prohibitively expensive and represent thus a major hurdle for the large scale deployment of Half-Heusler thermoelectrics.

During the first year of the project, we established in-house baseline synthesis processes for both n-type and p-type Half-Heusler materials. The status of development is summarized in Fig. 5. Fig. 5a and 5b show X-ray diffraction (XRD) patterns of n-type and p-type Half-Heusler materials directly after synthesis by melting from the elements (black line) and after subsequent ball milling and spark plasma sintering (SPS) into a dense Half-Heusler ceramic (red and blue curve). Also shown are calculated reflections based on the Half-Heusler structure, which show good correspondence with the experimental data. In the diffractograms of the as synthesized compounds, we observe additional reflections, which we identify as additional non-Half-Heusler phases crystallizing out of the melt due to composition segregation during cooling. While these additional phases may be difficult to suppress completely, we found that their fraction is minimized by subjecting the materials to ball milling and subsequent spark plasma sintering. The formation of a fine powder and mixing during milling leads to an additional homogenisation of the material at the micrometer scale that is then converted into Half-Heusler material during the high-temperature spark plasma sintering step.

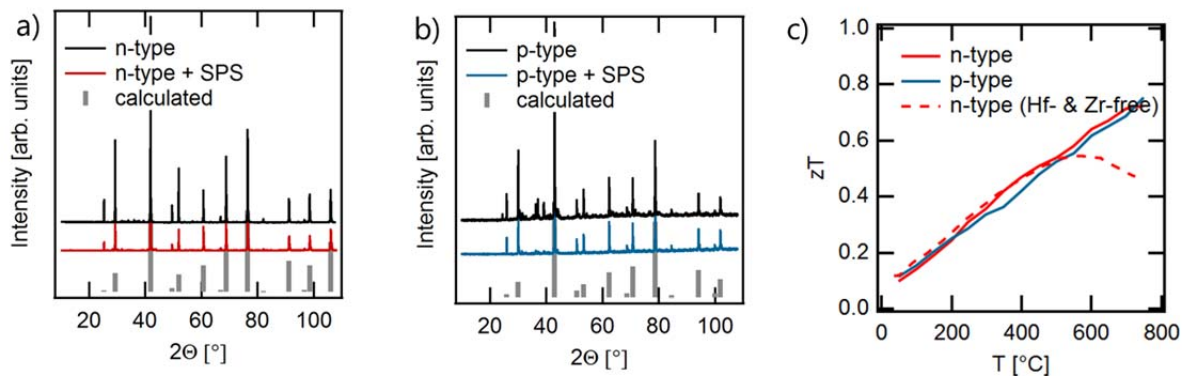


Figure 5: X-ray diffraction patterns before and after spark plasma sintering of (a) n-type and (b) p-type Half-Heusler thermoelectrics, diffraction peak positions calculated from the Half-Heusler structure are also shown. c) Thermoelectric figure of merit (zT) of in-house developed n-type and p-type Half-Heusler baseline processes.

The temperature dependence of the thermoelectric figure of merit zT for these baseline materials after spark plasma sintering is shown in Fig. 5c. Both n-type and p-type Half-Heusler materials show zT values >0.7 at 750°C. These results represent an excellent starting point for the module development activities described in section 2. Also shown in Fig. 5c is the temperature dependence of zT for Zr- and Hf-free Half-Heusler material based on TiNiSn developed in this project, which by the end of the project reaches zT values comparable to the Hf- and Zr- containing n-type material from our baseline up to temperatures of 500°C relevant for the applications studied in this project (see section 1.3 for more details).

A comparison of the raw materials cost for the Half-Heusler materials chosen for the baseline processes is shown in Table 1. As a consequence of the developments in the field, we decided early in the project to shift our efforts initially allocated to the development of high zT p-type Half-Heusler materials to the development of Zr- and Hf-free n-type Half-Heusler materials. With the achievement of high zT values in n-type TiNiSn compounds, we now dispose of a materials baseline for both n-type and p-type Half-Heuslers at a low raw materials cost of ~15\$/kg.

Table 1: Estimated gravimetric raw materials cost for Half-Heusler compositions chosen for the baseline process¹.



	n-type		p-type	
Composition	TiNiSn	Hf _{0.6} Zr _{0.4} NiSn _{0.98} Sb _{0.02}	FeTi _{0.2} Nb _{0.8} Sb	(Ti _{0.5} Zr _{0.5})(Fe _{0.2} Co _{0.8})Sb
Price (\$/kg)	14	221	16	26

1.3 Establish baseline for n-type Half-Heusler with zT near unity

Already 12 years ago, Sakura et al.¹⁰ reported a very high peak zT value of 1.45 for the (Ti,Zr,Hf)NiSn Half-Heusler system, which triggered intense research on Half-Heusler thermoelectrics. Yet this record was never reproduced and consequently intensely debated in the community. In 2013, Schwall et al.¹¹ achieved a peak zT value of 1.2, which confirmed the potential of this material. However, thermoelectric transport properties for the (Ti,Zr,Hf)NiSn system reported by many other groups exhibit a wide spread in values, which has so far not been explained in a unified framework. Furthermore, due to the relatively high cost of Zr and in particular of Hf, we decided to investigate the Zr- and Hf-free TiNiSn system in more detail. Preliminary results of this phase diagram study were already reported in the annual report 2016 and annual report 2017, but are integrated here in a unified framework including the link to thermoelectric transport properties.

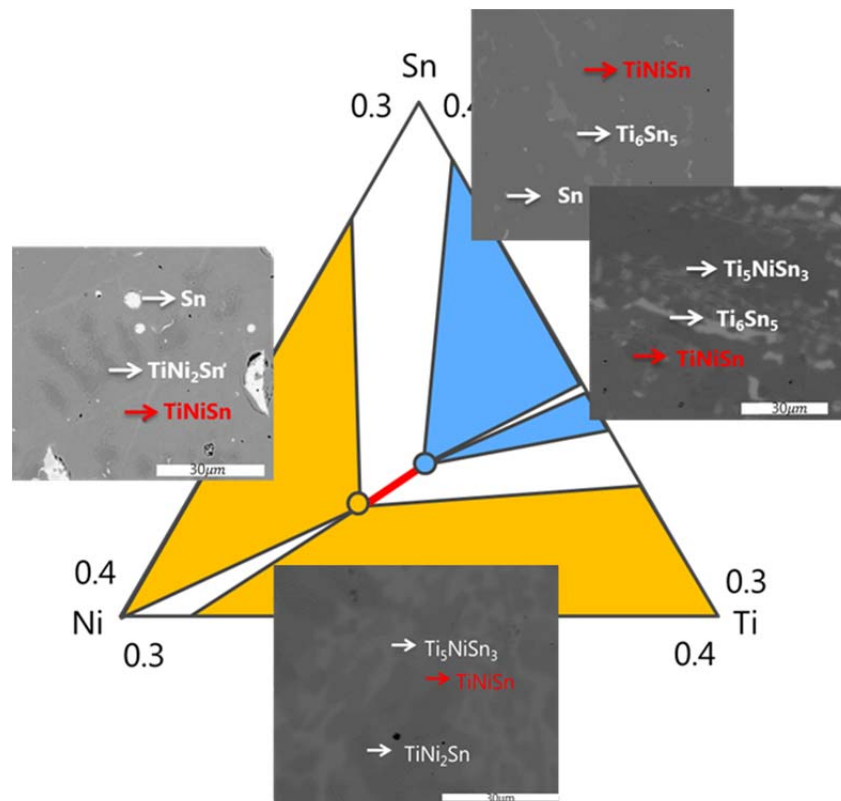


Figure 6: Magnified region of the isothermal section at 1223 K near TiNiSn on the Ti-Ni-Sn ternary phase diagram system with two stable boundary compositions (orange point: “Ni-rich TiNiSn” and blue point: “Ni-poor TiNiSn”) and solubility line (red line). Three-phase regions associated with Ni-rich and Ni-poor TiNiSn are colored in yellow and blue respectively. Each three-phase region is shown together with the corresponding SEM image in which the two secondary phases are indicated in white and the majority thermoelectric TiNiSn phase in red.



Fig. 6 shows a magnified region of the isothermal section at 1223 K on the Ti-Ni-Sn ternary phase diagram determined from experimental data. The phase diagram consists of four three-phase regions and four two-phase regions as suggested by Gürth et al.¹² and confirmed by our analysis. All eight regions contain the thermoelectric TiNiSn thermoelectric phase. Phase-pure TiNiSn is obtained for compositions along its solubility line (red line in Fig. 6) along which the Ni content varies.

The two end points of the solubility line are determined by wavelength dispersive spectroscopy (WDS) using electron probe microanalysis (EPMA) of the elemental composition of the TiNiSn phase in the different three-phase regions. In a three-phase region, the Gibbs phase rule leaves no degree of freedom, i.e. $F = C - P + 0 = 3 - 3 = 0$, where F represents the number of degrees of freedom, C is the number of component elements, P is the number of phases, and the 0 indicates that both temperature and pressure are fixed. Thus in a three-phase region, the Ni content in the Half-Heusler TiNiSn phase is also fixed. The Half-Heusler phase in both three-phase regions connecting to the solubility line on the Ni-rich side exhibit a Ni excess of approximately 6%, i.e. $\text{Ti}_{32.9(2)}\text{Ni}_{34.9(3)}\text{Sn}_{32.2(3)} \approx \text{TiNi}_{1.06}\text{Sn}_{0.98}$ at 1223 K, fixing the Ni-rich end point of the solubility line. These excess Ni atoms have been reported to occupy the vacancy sublattice of the Half-Heusler structure^{13, 14}. Their influence on the transport properties is discussed later in this section.

The Half-Heusler phase in the two three-phase regions on the Ni-poor end of the solubility line exhibits a nearly stoichiometric composition within experimental uncertainty, i.e. $\text{Ti}_{33.4(1)}\text{Ni}_{33.3(2)}\text{Sn}_{33.2(3)} \approx \text{TiNiSn}_{0.99}$ at 1223 K, fixing the Ni-poor end point of the solubility line. Note that the Ti and Sn content in the TiNiSn phase is nearly identical confirming that phase-pure TiNiSn compounds are obtained only along a line extending towards the Ni-rich direction in the isothermal section. The solubility range x in $\text{TiNi}_{1+x}\text{Sn}$ we found ($0 \leq x \leq 0.06$ at 1223 K) is consistent with Gürth et al. ($0.02 \leq x \leq 0.06$ at 1223 K) at the Ni-rich end but deviates on the Ni-poor end, the reason of which is not clear.

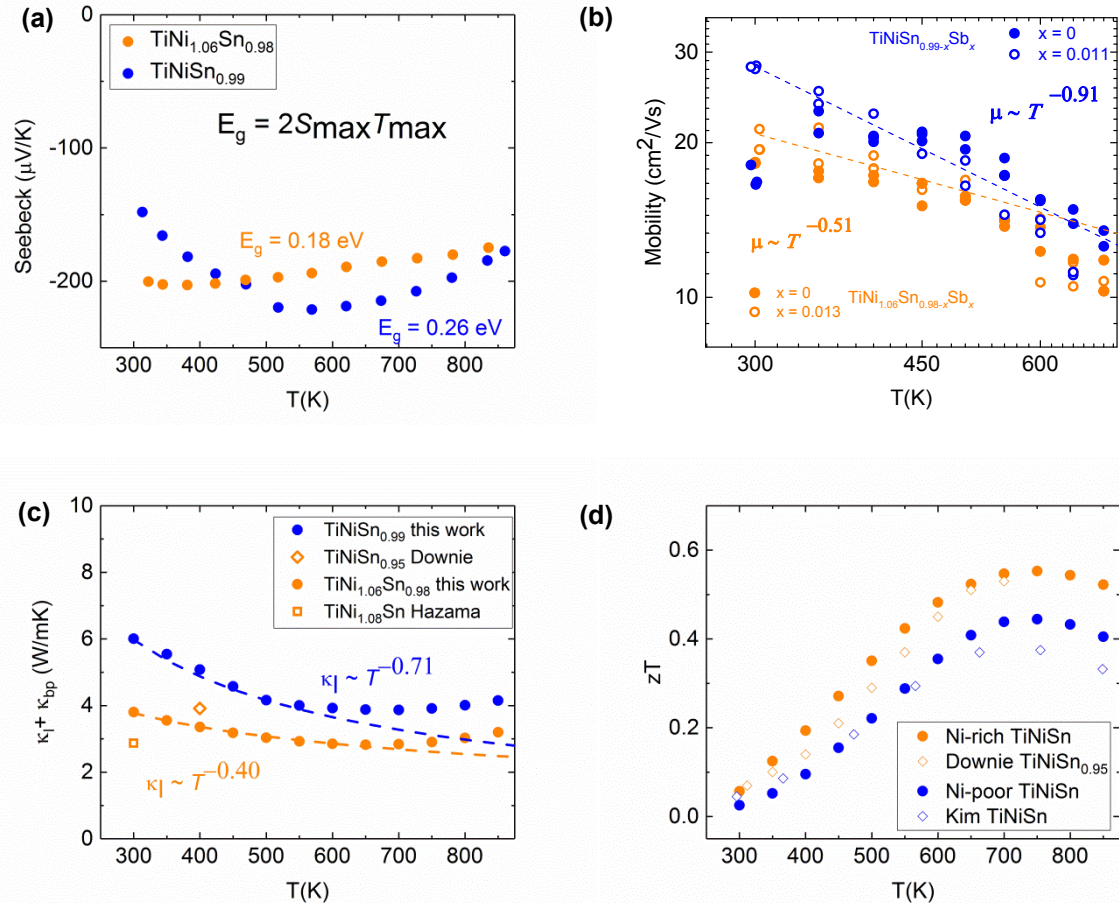


Figure 7. Thermoelectric transport properties of intrinsic TiNiSn (Ni-rich $\text{TiNi}_{1.06}\text{Sn}_{0.98}$ and Ni-poor $\text{TiNiSn}_{0.99}$). Temperature dependence of (a) Seebeck coefficient, (b) electron mobility, (c)



sum of lattice thermal conductivity and bipolar thermal conductivity, (d) figure of merit at TiNiSn stable boundary compositions is shown.^{13, 15} Ni-rich and Ni-poor TiNiSn represents stable boundary composition of $\text{TiNi}_{1.06}\text{Sn}_{0.98}$ and $\text{TiNiSn}_{0.99}$ respectively. Filled symbols represent intrinsic TiNiSn without Sb doping. Empty circles represent TiNiSn doped with Sb ($x = 0.013$ for Ni-rich and $x = 0.011$ for Ni-poor, respectively) to avoid minority carrier scattering near room temperature.

The temperature dependence of the Seebeck coefficient, electron mobility, and the sum of lattice thermal conductivity and bipolar thermal conductivity of both Ni-rich and Ni-poor TiNiSn stable boundary compositions is shown in Fig. 7a, 7b and 7c, respectively. Both samples show negative Seebeck coefficients throughout the whole temperature range, indicating n-type semiconductor behavior. With increasing temperature, the magnitude of the Seebeck coefficient in Fig. 7a increases first and starts decreasing after reaching a maximum, which we expect to be induced by the bipolar effect. From the Goldsmid equation¹⁶, we can estimate the band gap from the maximum value of the Seebeck coefficient and the temperature at which the maximum Seebeck coefficient occurs. We find that for the Ni-rich TiNiSn stable boundary composition, the band gap decreases to 0.18 eV, compared to 0.26 eV for the Ni-poor TiNiSn stable boundary composition. The narrowing of the Goldsmid gap is direct experimental evidence for the presence of new electronic states within the band gap reported earlier based on density functional theory calculations of the electronic band structure of HH with excess Ni.

The temperature dependence of the electron mobility shown in Figure 7b also shows two different slopes at low temperature for the Ni-rich and the Ni-poor samples before the onset of intrinsic carrier excitation. An expression for the temperature dependence of the electronic mobility can be derived within the Boltzmann transport formalism $\mu \sim T^{-\alpha}$ ¹⁷. For most thermoelectric materials above room temperature, the dominant electron scattering mechanism is presumed to be deformation potential scattering caused by acoustic and nonpolar optical phonons often collectively called “acoustic phonon scattering”. Due to minority carriers in intrinsic samples, the temperature dependence of mobility deviates from the decreasing trend near room temperature. Thus mobility data of two more samples with Sb doping ($x = 0.013$ for Ni-rich $\text{TiNi}_{1.06}\text{Sn}_{0.98-x}\text{Sb}_x$ and $x = 0.011$ for Ni-poor $\text{TiNiSn}_{0.99-x}\text{Sb}_x$) are also shown without the influence caused by minority carriers. Before the occurrence of thermal excitation, the electron mobility at the Ni-poor TiNiSn stable boundary composition shows a $T^{-0.91}$ dependence, confirming that acoustic phonon scattering with typical exponents between -1 and -1.5 is important. In contrast at the Ni-rich TiNiSn stable boundary composition, the Hall mobility exhibits a $T^{-0.5}$ dependence typical for alloy scattering presumably due to the additional Ni atoms in the vacancy sublattice¹⁸.

The sum of lattice and bipolar contribution to the thermal conductivity, $\kappa_L + \kappa_{bp}$, is obtained by subtracting the electronic contribution from the total thermal conductivity using the Wiedemann-Franz law. We adopted a Lorentz number calculated from $L = 1.5 + \exp(-|S|/S_0)$ to simplify the estimation of electronic thermal conductivity, where S is the measured Seebeck in $\mu\text{V/K}$ and $S_0 = 116 \mu\text{V/K}$ ¹⁹. The calculated $\kappa_L + \kappa_{bp}$ is shown in Figure 7c. A much suppressed lattice thermal conductivity is found in Ni-rich TiNiSn, which takes a value of about $3.7 \text{ Wm}^{-1}\text{K}^{-1}$ at 300 K compared to $6.0 \text{ Wm}^{-1}\text{K}^{-1}$ for Ni-poor TiNiSn. This is explained by the strong phonon scattering due to alloying effects.

We also notice different lattice thermal conductivity values by Downie et al. ($\text{TiNiSn}_{0.95}$)¹³ and Hazama et al. ($\text{TiNi}_{1.08}\text{Sn}$)²⁰. The value offset among these samples and the Ni-rich $\text{TiNi}_{1.06}\text{Sn}_{0.98}$ in this work could be due to different annealing/pressing temperatures. By mapping these compositions on the Ti-Ni-Sn isothermal section at 1223 K (Figure 6), one finds that Downie and Hazama’s samples are in the Ni-rich three-phase regions ($\text{TiNiSn}_{0.95}$ in three-phase region with coexisting TiNiSn, TiNi_2Sn and Ti_5NiSn_3 ; $\text{TiNi}_{1.08}\text{Sn}$ in three-phase region with coexisting TiNiSn, TiNi_2Sn and liquid Sn). Thus both samples should benefit from the reduction of lattice thermal conductivity due to excess Ni. In Downie’s study a lower annealing temperature (1173 K) is adopted compared to this work (1223 K), whereas in Hazama’s study a high SPS temperature of 1373 K is applied without further annealing. According to our experimentally determined temperature dependent Ni solubility, higher processing temperature leads to larger amount of excess Ni and thus lower lattice thermal conductivity. By mapping compositions back onto the phase diagram, all data are explained systematically successfully.



In summary, Ni interstitials in TiNiSn Half-Heuslers are effective in reducing the band gap and scattering both electrons and phonons. The reduction in thermal conductivity associated with scattering by Ni interstitials is much larger than the reduction in weighted mobility, which leads to higher zT in the Ni-rich TiNiSn (Figure 7d). Thus by selecting one or the other stable boundary composition, Seebeck coefficient, lattice thermal conductivity, and zT could differ by as much as 41%, 58% and 25% respectively even without extrinsic doping, adding much to the confusion in literature. As Kim et al. reported a peak zT value of 0.38 at 750 K and Downie et al. found a peak zT value of 0.53 at 700 K, the large discrepancy (~40%) can be well explained by the relatively narrow yet influential Ni solubility range in the intrinsic TiNiSn phase^{13,15}.

Our phase diagram analysis is also of high relevance when scaling the synthesis of TiNiSn Half-Heuslers to industrial production as the physical properties of the synthesized materials should be robust within a sufficiently large compositional tolerance window to guarantee consistent thermoelectric materials properties. By choosing a nominal composition that lies in one of the four three-phase regions, the amount of Ni interstitials in the TiNiSn Half-Heusler phase can be precisely controlled as well as the type and to a certain extend the amount of secondary phases.

The results discussed in this section were recently accepted for publication in the prestigious scientific journal Energy & Environmental Science (Tang Y. *et al.*, Energy & Environmental Science, DOI: 10.1039/c7ee03062b)

2. Streamline module fabrication

2.1 Develop scalable module platform

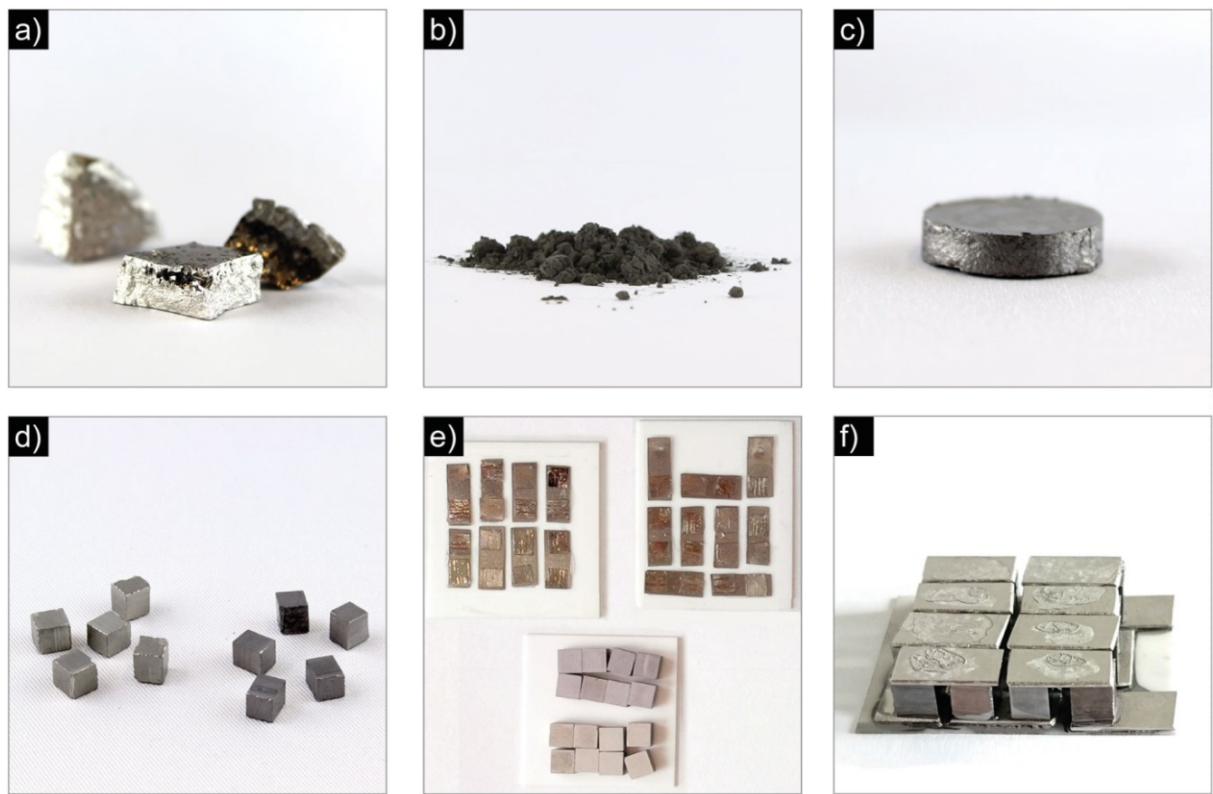


Figure 8: From the raw material to the module. Half-Heusler material after synthesis by melting of the elements (a), after ball milling (b), after spark plasma sintering (c), and after diamond wire sawing into individual legs (d). Components of a 16-leg Half-Heusler thermoelectric module with Ti contacts before (e) and after assembly (f).



During the first phase of the project, we established a fabrication scheme for Half-Heusler thermoelectric modules. To accelerate module development, the synthesis of n-type and p-type Half-Heusler material is outsourced to an external commercial partner that synthesises Half-Heusler material in 200 g batches following protocols developed and specified by Empa. Upon reception, the material quality is validated by X-ray diffraction and thermoelectric transport measurements. We considered two types of p-type material for the baseline process, a member of the family of newly discovered p-type Half-Heusler alloys with the composition $\text{FeTi}_{0.2}\text{Nb}_{0.8}\text{Sb}$ (p1-type) and a member of the family of more traditional p-type Half-Heusler materials with composition $(\text{Ti}_{0.5}\text{Zr}_{0.5})(\text{Fe}_{0.2}\text{Co}_{0.8})\text{Sb}$ (p2-type). As n-type material, we employ $\text{Zr}_{0.4}\text{Hf}_{0.6}\text{NiSn}_{0.98}\text{Sb}_{0.02}$. In the later stage of the project, Zr- and Hf-free n-type Half-Heusler $\text{Ti}_{0.33}\text{Ni}_{0.35}\text{Sn}_{0.32}\text{Sb}_{0.007}$ material described in section 1.3 was also employed.

The as-synthesized Half-Heusler material (Fig. 8a) is crushed with a mortar to sizes <0.1 mm and further processed in a ball mill to obtain powders with a grain size of $1\text{--}10$ μm (Fig. 8b). Particle size distribution is measured with a laser diffraction particle size analyzer. To avoid oxidation, powders are handled, processed, and stored in the glove box. The powders are compacted into discs with diameters of $10\text{--}50$ mm using spark plasma sintering (Fig. 8c). The p1-type and n-type powders are sintered at 50 MPa and 900°C for 1 h, whereas the p2-type powders are processed at 50 MPa and 1000°C . The sintered material is very dense. Its density reaches about 98% of the density of the corresponding single crystal. Since the microstructure of the sintered material (i.e. grain size, grain size distribution, pores, density of sintered body) influences directly the thermoelectric properties, the milling and sintering recipe were optimized (see also thermoelectric performance data in Fig. 5).

After polishing, discs are sawed into individual legs, e.g. with size $4.0 \times 4.0 \times 4.4$ mm³, using diamond wire sawing technology (Fig. 8d). The leg height of 4.4 mm is chosen based on initial modelling results from section 3 in order to obtain maximum output power by establishing a compromise between thermal heat flux across the leg and temperature difference between hot and cold side of the leg. Finally individual pairs of n- and p-type legs are assembled into thermoelectric modules (Fig. 8e and Fig. 8f) such that the contact plates are contacted electrically in series and thermally in parallel.

Establishing contacts that provide electrical and mechanical long-term stability when exposed to steep temperature gradients and repeated thermal cycling is a formidable materials challenge. To obtain a 4×4 module, 16 legs were assembled in a first series of experiments with 17 Ti contact plates using Empa proprietary reactive glue. The glue provides sufficient strength enabling assembly of the module at room temperature. The modules are then transferred to the spark plasma sintering furnace, where the contacts are brazed under pressure and high temperature to bond the Ti plates to the n-type and p-type Half-Heusler legs. At elevated temperature the glue decomposes, leaving only small amounts of carbon residues. In addition, the glue enhances the reactivity at the contact interface leading to stronger bonds. Initial devices were fully functional, but showed limited mechanical integrity under thermal cycling. The main issue with the Ti contacting scheme is the poor ductility of Ti during brazing. Since, under the given conditions, Ti does not form an interlayer with the Half-Heusler material, the obtained shallow-diffusion contacts are not sufficiently stable for long-term operation.

To overcome the disadvantages of Ti brazing, Cu contact plates were investigated as candidates to obtain deep diffusion contacts (Fig. 9a and b). After sintering, the contacts exhibit low contact resistivity and are mechanically very stable. However Cu is alloying with the p1-type material and destroys its thermoelectric properties (Fig. 9c).

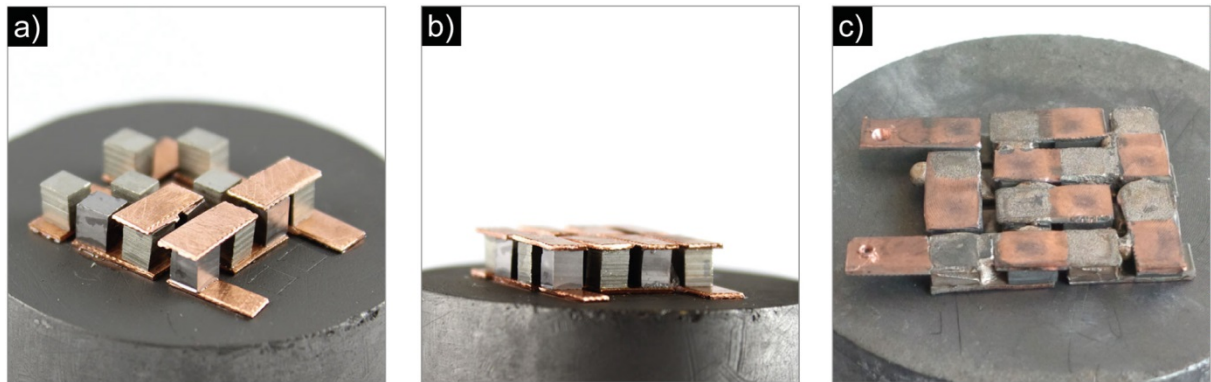


Figure 9: a) Half-Heusler module assembly with Cu contacts, b) fully assembled modules with Cu contacts, c) Half-Heusler module after brazing in the spark plasma sintering furnace.

To circumvent this problem, we investigated Ni contacts as an alternative to Cu contacts. After brazing a Ni plate to the n-type Half-Heusler material, the legs can be broken off the plates easily. We found that the reason for the weak mechanical strength of Ni contacts and the high electrical contact resistance is the formation of cracks as depicted in the scanning electron image in Fig. 10a. In fact Ni brazing on the Half-Heusler materials leads to the formation of a boundary layer that energy dispersive X-ray analysis identifies as having a composition $(\text{Zr}_{0.4}\text{Hf}_{0.6})\text{Ni}_2\text{Sn}$, which is the stoichiometry of the related Full-Heusler compound. Interestingly the crack does not form between the Ni contact and this Full-Heusler boundary layer, but at the interface between the Full-Heusler and the Half-Heusler. We found that brazing Ni contacts is possible when employing a thin Ti powder interlayer that suppresses Ni diffusion into the Half-Heusler phase (Fig. 10b), the diffusion of Ni towards the Half-Heusler can be suppressed. Energy dispersive X-ray analysis of the scanning electron microscopy image in Fig. 10c shows that Ni and Ti form a 10 μm thick interlayer but neither Ni nor Ti diffuses into the Half-Heusler. The advantage of this approach is that brazing is simplified, i.e. the Ni side of the metallized Half-Heusler legs can be brazed directly to Ni contact plates using a standard Ni to Ni brazing.

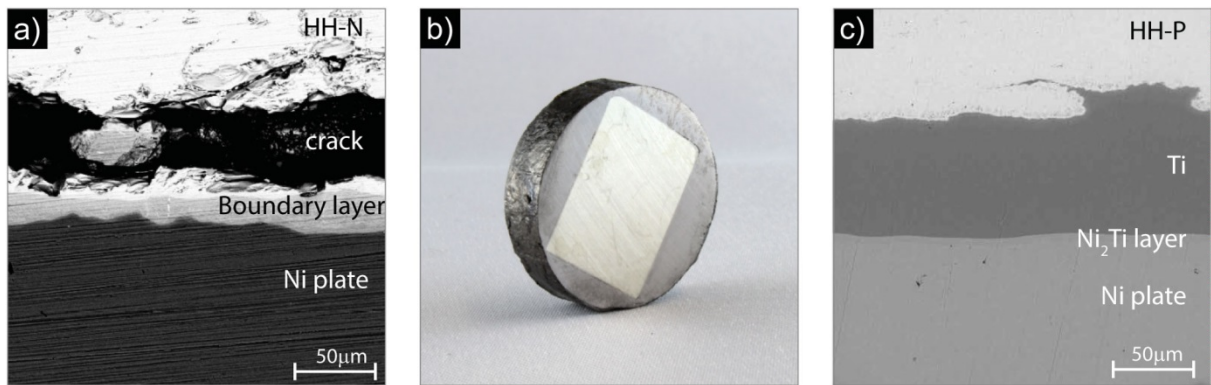


Figure 10: a) Scanning electron microscopy image of a brazing test where a Ni plate is directly brazed to the n-type Half-Heusler material resulting in Ni diffusion into the Half-Heusler and formation of a Full-Heusler boundary layer that cracks upon thermal cycling, b) a disk of p-type Half-Heusler with integrated Ni plate contact brazed with a Ti interlayer, c) electron microscopy image of the contact showing the Ti interlayer that prevents Ni diffusion into the Half-Heusler.

Module fabrication was further streamlined during the second year of the project. A retired vibratory disc mill (Fig. 11a and b) was reactivated at Empa to crush Half-Heusler material into coarse powder $<0.1 \text{ mm}$ so it can be further processed to fine powder in a planetary ball mill. This step replaces the manual mortar step. In addition, an efficient diamond blade saw (Fig. 11c) was acquired which accelerates the cutting of legs from the pellets.

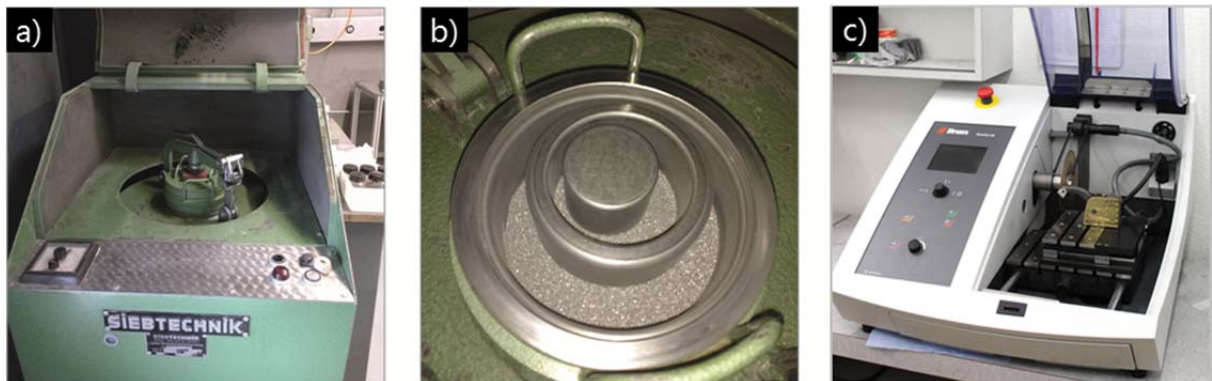


Figure 11: New elements of the scalable module platform. (a) vibratory disc mill, (b) vial filled with sample powder, (c) diamond blade saw.

Half-Heusler pellets with a diameter of 50 mm and height typically between 4 and 6 mm including deep diffusion contacts developed (as mentioned above) are cut into legs and brazed into modules using direct copper bonded ceramic aluminium nitride substrates (Fig. 12a and b) supplied by a third party supplier according to Empa's specifications. The copper on the ceramic substrates not only serves as brazing partner but is also patterned in a way as to interconnect p- and n-type Half-Heusler legs. This solution grants improved mechanical stability also upon thermal cycling and manufacturability. Mechanical abuse tests show that the modules tend to break no longer at the contacts but rather directly across the thermoelectric legs, which demonstrates the high mechanical stability of the contacts.

The performance of the modules (Fig. 12c) is strongly influenced by the chosen brazing solution. Deep diffusion contacts with Ni plates improve the module output power by a factor of 16 compared to the initial solution with shallow diffusion contacts based on Ti plates partially due to a doubling of the open-circuit voltage, a reduction of the internal resistance by a factor close to 8, but also lower thermal resistance and improved thermal coupling to the heating and cooling units provided by the soft Cu on the AlN plates. Ti, in contrast, is rather hard and has a 20-fold lower thermal conductivity. The temperature difference on the legs can be estimated by dividing the open-circuit voltage of the modules by an average Seebeck coefficient for the n- and p-type Half-Heusler materials (neglecting radiative and convective heat losses), leading to an effective temperature difference of 530°C for the embedded Ni and only 270°C for the Ti contacts for a temperature difference of 575°C applied to the module.

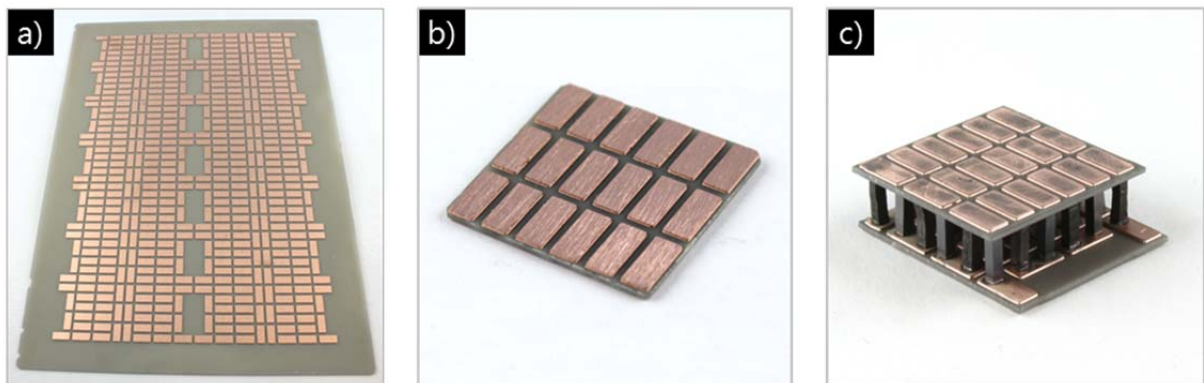


Figure 12: Direct copper bonded aluminium nitride substrate (a) as received, (b) after cutting to module size, and (c) integrated into complete thermoelectric module.

Several modules with different geometries and architectures were fabricated to investigate the interdependencies that rule the behaviour of (1) generated current and voltage, (2) difference of



temperature between the top plate and bottom plate, (3) heat flow, (4) clamping pressure and (5) heat flux-to-electric power efficiency. Fig. 6 depicts some of the fabricated modules. The 16 legs module in Fig. 13a served as a base design for module development where each leg possesses an area of $4 \times 4 \text{ mm}^2$ and a height of 5.5 mm. These modules deliver an open-circuit voltage of up to 0.85 V and 1.54 W with a series resistance of $117 \text{ m}\Omega$ at a temperature difference of 575°C and a clamping pressure of 9 MPa.

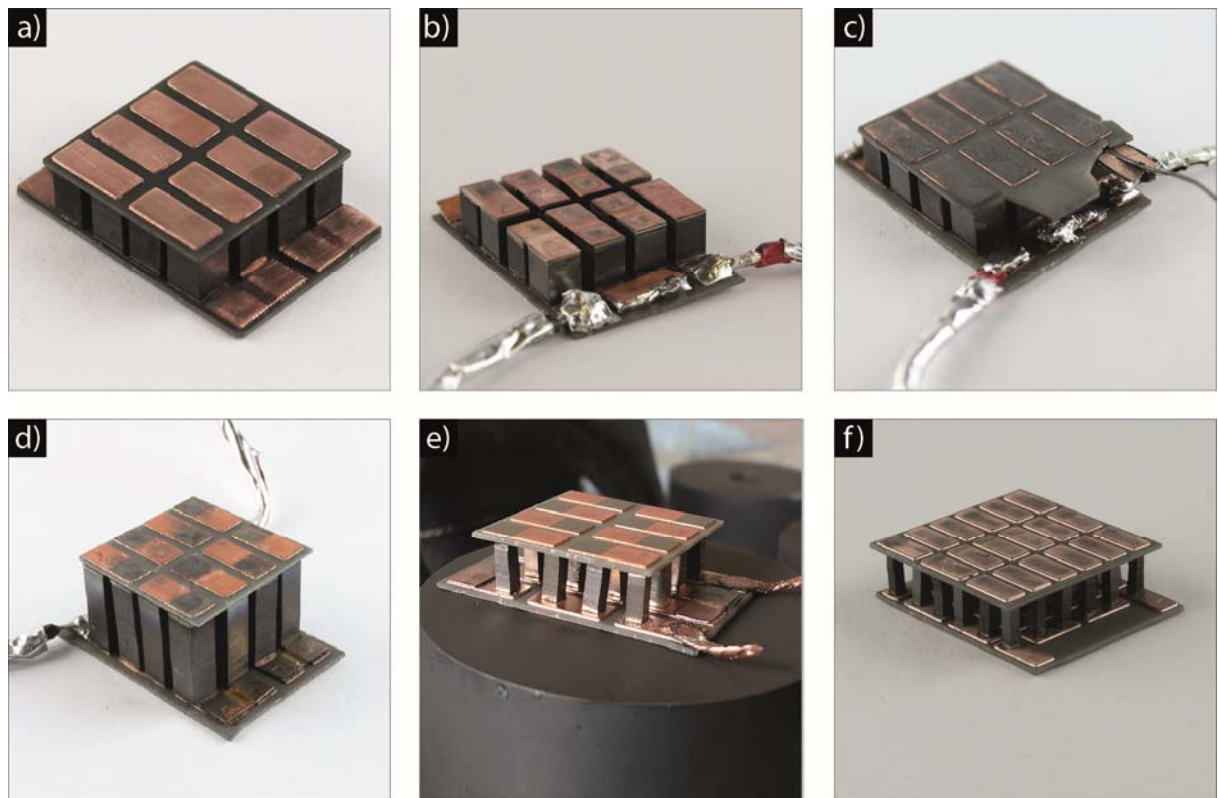


Figure 13: Fabricated module prototypes, a) is the standard 16 legs reference module b) has no top AlN plate, it has a lower open circuit voltage and performance than the standard one, c) has an embedded thermocouple on the top side (right), it allows to check the temperature directly on the leg, d) this module has longer legs thereby increasing its thermal resistance, e) the leg area is smaller, it has a higher performance per area and f) is the most recent design, it has 36 legs for an improved open-circuit voltage and output power. Leg dimensions were optimized using the multi-physics model described in 2.3.

Fig. 13b depicts a module fabricated without an AlN on the hot side. To minimize the thermal resistance on the hot side only a thin copper foil (0.11 mm) was employed as contact between the legs. Sufficient mechanical stability is provided by the AlN plate on the cold side. The thin foil contacts guarantee an optimum heat transmission from the test bench to the module. At a temperature difference of 575°C , an open-circuit voltage of 0.75 V was measured. This value is lower than for the standard module.

In a next iteration shown in Fig. 13c, a thermocouple was integrated directly into the contact layers of a thermoelectric module to measure the temperature at the legs and compare it to the temperature on the outside of the module. With sufficient clamping pressure of typically 9 MPa, only a small difference in temperature below 5°C was observed on the cold side, while the hot side temperature difference was below 10°C .

In Fig. 13d, a module with 3x higher legs is shown. This increases the contribution of the legs to the thermal resistance, but not the contribution of the contacts. At a temperature difference of 575°C, an open-circuit voltage of 0.89 V is measured, while the shorter modules delivered 0.85 V and the maximum achievable open-circuit voltage derived from the Seebeck coefficient and the temperature difference is 1.05 V (neglecting radiative and convective heat losses and temperature drops over the contacts).

Fig. 13e shows a module for which the leg area was reduced to 2x2 mm². The number of legs is the same but the leg area is reduced by a factor of 4. The maximum output power of this module is 0.77 W at a temperature difference of 575°C (see Fig. 14a), which is around half of the 1.54 W that the 16 legs module with 4x4 mm² legs delivers. This means that a module with a fourth of the active material delivers still one half of the power. This can be explained with a study of the electrical resistances. The module has Ohmic power losses due to parasitic resistance R_p , which are proportional to the square of the current $P_{\text{losses}} = R_p \cdot I^2$.

Fig. 13f presents the most recent module development step where the number of 2x2 mm² legs was increased from 16 to 36 to generate a higher open-circuit voltage. For these modules, AlN plates with a different Cu pattern were designed. Fig. 14a depicts the current density-voltage and power-voltage characteristics of this optimized 36 legs module delivering an open-circuit voltage of 2.0 V and a maximum output power of 2.16 W increasing the maximum output power by a factor of ~3 compared the 16 legs module with 2x2 mm² legs whose characteristics are also shown in Fig. 14a.

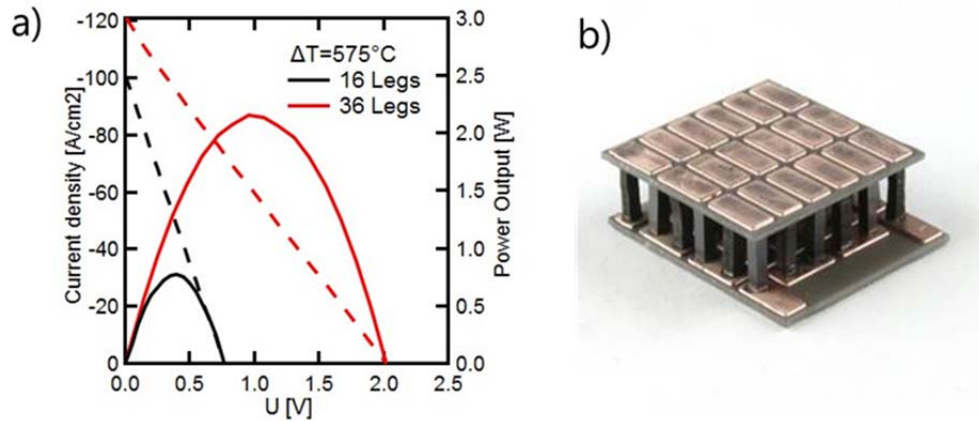


Figure 14: a) Current density-voltage (left axis, dashed line) and power-voltage (right axis, continuous line) of the 16 legs module with 2x2x5.6 mm³ legs compared to the 36 legs module with 2x2x5.6 mm³ legs (shown on the right). The open-circuit voltage increases by a factor of 2.3, while the maximum output power increases by a factor of 3.3.

This module optimization was partially guided by a fully parametrized multi-physics model developed specifically for this purpose which is described in section 2.3. To validate this model, materials properties of the thermoelectric materials integrated into the modules had to be reassessed by cutting samples for thermal and electric conductivity measurements as well as the determination of the Seebeck coefficient from the pellets that were used to fabricate modules.

Within this model, five different Half-Heusler materials were analysed including n-type and p-type Half-Heusler material from the baseline, the newly developed Hf- and Zr-free n-type Half-Heusler, as well as n- and p-type Half Heusler materials with the best reported performance from literature^{11,21} identified in the SFOE report "Potential of thermoelectrics for waste heat recovery"²³. The compositions and material abbreviations used for the next paragraphs are summarized in Tab. 2.

**Table 2: Half-Heusler Materials used in the fabrication of modules**

Material	Composition	Designation
<i>p-type Half-Heusler</i>	$\text{FeTi}_{0.2}\text{Nb}_{0.8}\text{Sb}$	“FeNbSb”
<i>n-type Half-Heusler</i>	$\text{Zr}_{0.4}\text{Hf}_{0.6}\text{NiSn}_{0.98}\text{Sb}_{0.02}$	“HfNiSn”
<i>n-type Half-Heusler (Zr-, Hf-free)</i>	$\text{Ti}_{0.33}\text{Ni}_{0.35}\text{Sn}_{0.32}\text{Sb}_{0.007}$	“TiNiSn”
<i>n-type Half-Heusler (best)</i> ¹¹	$\text{Ti}_{0.5}\text{Zr}_{0.25}\text{Hf}_{0.25}\text{NiSn}_{0.998}\text{Sb}_{0.002}$	„Schwall n-type“
<i>p-type Half-Heusler (best)</i> ²¹	$\text{FeNb}_{0.9}\text{Hf}_{0.1}\text{Sb}$	“Fu p-type”

The measured thermal and electrical transport properties as well as the figure of merit and the maximum possible efficiency calculated from the measured baseline materials data using the method proposed by Kim et al.²² are shown in Fig. 15 and compared to the best-in-class materials from literature in Fig. 16.

From Fig. 15a and b it can be seen that the p-type baseline material FeNbSb has a much higher thermal conductivity and a higher electrical conductivity than the Zr- and Hf-containing n-type material. The new n-type Zr- and Hf-free n-type material TiNiSn without Zr and Hf has a 40% higher thermal conductivity than the standard n-type HfNiSn which would reduce the performance of a thermoelectric module. However, the electrical conductivity of TiNiSn is 70-85% higher leading to a smaller inner resistance and finally an overall increase in module performance as we will see in the following. The Seebeck coefficient shown in Fig. 15c is similar for both n-type materials and overall slightly higher than for the p-type. As a consequence of those three materials properties, the figure-of-merit of the baseline materials HfNiSn and FeNbSb shown in Fig. 15d is very similar. This is due to the high thermal conductivity of the p-type material being compensated by its high electrical conductivity. The figure of merit is significantly higher for the new Zr- and Hf-free n-type material TiNiSn due to the large difference in electrical conductivity. The same behaviour is observed for the engineering figure of merit in Fig. 15e calculated using the approach proposed by Kim et al.²² and discussed in detail in the SFOE report “Potential of thermoelectrics for waste heat recovery”²³. Here a cold side temperature of 30°C is assumed and the temperature of the hot side is swept from 30°C up to 570°C. Using this approach the maximum efficiency of the three materials was derived from the engineering figure of merit and is shown in Fig. 15f. While our standard baseline materials FeNbSb and HfNiSn reach an efficiency of 4% and 5% respectively at 570°C on the hot side, the new Zr- and Hf-free n-type material TiNiSn allows to achieve an efficiency of up to 6.5%. It should be pointed out that these materials are straight out of the non-optimized and not-drift-corrected baseline process (zT values for initially optimized baseline process values can be found in Fig. 5c and Fig. 7d) and are not yet representative for best-in-class Half-Heusler materials. But as we will show below, substantial performance gains can be achieved by optimizing the module design before the final material optimization.

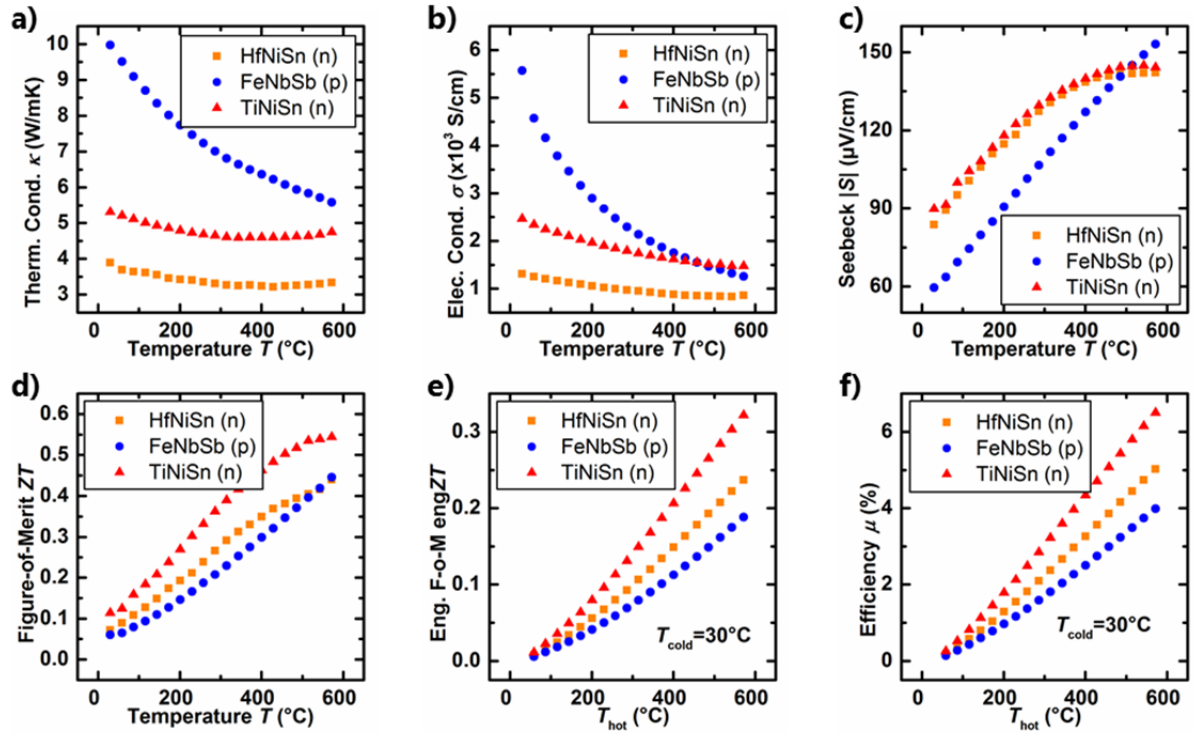


Figure 15: Transport properties of n- and p-type thermoelectric Half-Heusler materials used for module fabrication. a) Thermal conductivity, b) electrical conductivity, c) Seebeck coefficient and d) figure of merit as a function of temperature. e) Engineering figure of merit and f) theoretical efficiency as a function of hot side temperature, the cold side is set to 30°C.

Fig. 16 compares our Half-Heusler materials to the so far best performing Half-Heusler materials reported and described in literature^{11, 21} to provide an estimate for the additional performance gains that may be achieved through materials optimization. For this comparison, the doped n-type material $\text{Ti}_{0.5}\text{Zr}_{0.25}\text{Hf}_{0.25}\text{NiSn}_{0.998}\text{Sb}_{0.002}$ from Schwall *et al.*¹¹ and p-type $\text{FeNb}_{0.9}\text{Hf}_{0.1}\text{Sb}$ from Fu *et al.*²¹ were chosen. From Fig. 16a it can be seen, that our p-type material possesses a thermal conductivity about 20% higher than for the Fu p-type. The Zr- and Hf-containing Schwall n-type material has up to 45% lower thermal conductivity than our n-type material TiNiSn which is beneficial to maintain a high temperature differential between the hot and cold side of the thermoelectric module. The electrical conductivity shown in Fig. 16b is comparable for both p-type materials decreasing with increasing temperature. The TiNiSn shows the same behaviour, but has the same high electrical conductivity as p-types at 600°C which improves the thermoelectric performance. The Schwall n-type shows increasing electrical conductivity with increasing temperature but at rather low values compared to our new n-type. Fig. 16c shows that the Seebeck of both best materials is significantly higher with 30-50% for the p-type and 40-100% for the n-type. The Seebeck is temperature-dependent and so the difference between best and our material changes. It has to be remarked that in the higher temperature range around 570°C, the best reported material is only 40% higher than our Zr, Hf free n-type. Fig. 16d and e reveal very high values for the figure of merit and engineering figure of merit for the Schwall n-type and Fu p-type resulting from low thermal conductivity of the n-type, high electrical conductivity of the p-type, and very high Seebeck coefficient in both materials. With a figure of merit above 1.0 at 600°C, the calculated maximum efficiencies for the best materials are a factor of 2 higher than for the materials of our baseline process (Fig 15f) demonstrating the untapped potential of this materials class within this project.

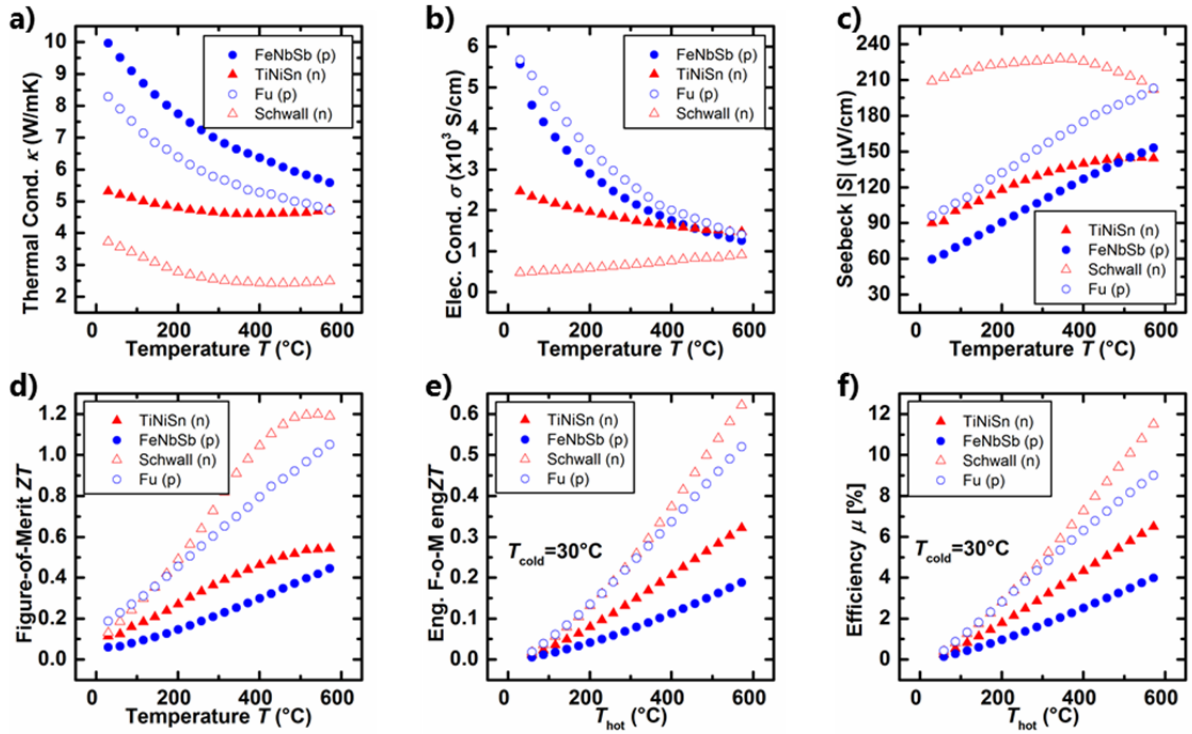


Figure 16: Transport properties of the thermoelectric p-type and n-type Half-Heusler materials of our materials baseline compared to the best performing materials reported in literature^{11, 21}. a) Thermal conductivity, b) electrical conductivity, c) Seebeck coefficient and d) figure of merit as a function of temperature. e) Engineering figure of merit and f) theoretical efficiency as a function of hot side temperature, the cold side is set to 30°C.

The materials properties of the best materials reported in literature discussed in this chapter were also used as input for the multi-physics model discussed in 2.3 to assess the potential performance gains on module level with these materials compared to the baseline materials of this project, with which the model was validated experimentally.

To validate the multi-physics models discussed in 2.3, modules with 4x4 legs (leg area 2x2 mm²) were built and tested on the test bench. Both modules, FeNbSb/HfNiSn and FeNbSb/TiNiSn, were tested at $\Delta T = 575^\circ\text{C}$, 1500 N clamping force, and under vacuum. Detailed setup conditions are shown in Tab. 3. Using voltage sweeps from 0.0 to 2.0 V, the current and power output of the modules was measured. From the resulting open-circuit voltage and short-circuit current, the internal resistance was calculated, which is not only influenced by the electrical conductivity and the contact resistance but also by the mechanical integrity of the module (e.g. cracks in the legs cause an increase in the internal resistance of the module).

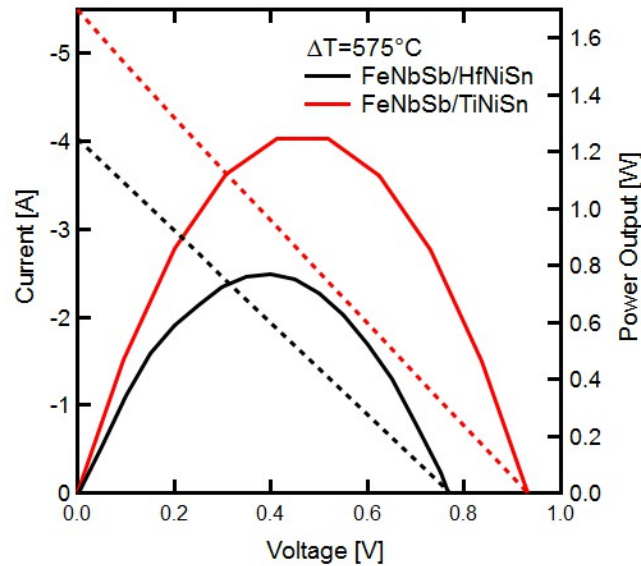


Figure 17: Measured current-voltage and power-voltage curves of modules with 16 legs ($2 \times 2 \text{ mm}^2$) containing different n-type materials. The measurement was performed at ΔT of 575°C .

The results are shown in Fig. 17 and Tab. 3. The current-voltage curves (dotted lines) show that in the FeNbSb-TiNiSn module with the new Zr- and Hf-free n-type material up to 40% more current flows compared to the FeNbSb/HfNiSn module with the Zr- and Hf-containing n-type material. Consequently, the internal resistance is lower for the FeNbSb-TiNiSn module with a value of 0.168Ω compared to 0.185Ω for the FeNbSb-HfNiSn (see Tab. 3). The reason behind is the higher electrical conductivity of the new n-type material (see again Fig. 15b). A low internal resistance leads to a higher current since less energy is dissipated as Ohmic losses. The bell-shaped curve (continuous) shows the module power output in dependence of the applied voltage revealing two main characteristics regarding thermoelectric performance of the module. The open-circuit voltage U_0 is 0.94 V for the FeNbSb/TiNiSn module and therefore significantly higher than for the FeNbSb/HfNiSn module with 0.76 V . The reason for this remains unclear (possibly hysteresis effects). From the values of the Seebeck coefficient in Fig. 15c, a comparable open-circuit voltage is expected (compare also Fig. 26). The maximum matched power output (P_{\max}) is 0.77 W for the FeNbSb/HfNiSn module and 1.20 W for the FeNbSb/TiNiSn module.

Table 3: Comparison of FeNbSb/HfNiSn and FeNbSb/TiNiSn modules measured on the test bench.

	FeNbSb/HfNiSn	FeNbSb/TiNiSn
Total leg area	0.64 cm^2 (16 legs)	0.64 cm^2 (16 legs)
Leg height	4 mm	4 mm
Conditions	$\Delta T = 575^\circ\text{C}$ ($T_h = 625^\circ\text{C}$, $T_c = 50^\circ\text{C}$) , $F = 1500 \text{ N}$, $p = 1.2 \text{ mbar}$	
P_{\max} ($P_{\max}/\text{leg area}$)	0.77 W ($1.20 \text{ W}/\text{cm}^2$)	1.20 W ($1.88 \text{ W}/\text{cm}^2$)
U_0	0.76 V	0.94 V
R_i	0.185Ω	0.168Ω

2.2 Development of net shape manufacturing technique

A net shape manufacturing process was developed with the aim to sinter Half-Heusler powder directly into individual legs. For this, a hardware and software upgrade was installed on the spark plasma sintering tool enabling process control through the read-out of a thermocouple. Custom-designed graphitic carbon pressing tools (Fig. 18a) enabling the simultaneous fabrication of 5 cylindrical thermoelectric legs with a diameter of 5 mm and variable height were successfully tested in the spark plasma sintering furnace (Fig. 18b).

Half-Heusler legs fabricated by the net shape manufacturing techniques are shown in Fig. 18c. While the legs look ideal for module manufacturing at first sight, careful inspection of Fig. 18c reveals uneven top surfaces and rims caused by powder escaping into the space between the die and the punch during sintering. Before module integration, these rims need to be polished off for each leg individually, which is a relatively time consuming and delicate task. Indeed, extensive post processing steps are a general challenge for additive manufacturing techniques and have a tendency to compensate the advantages when compared to traditional subtractive manufacturing techniques.

While the net shape manufacturing technique was proposed in order to streamline module development in the lab, diamond wire sawing remains the more efficient pathway. Although relatively time consuming on our lab-setup, where only one cut at a time can be performed, diamond wire sawing on industrial scale is a very efficient and rapid technique that is easily parallelized to perform multiple cuts with the same wire and results in minimal kerf losses. These advantages make it the technology of choice for cutting mono- and multicrystalline silicon wafers for the photovoltaic market. Market leader for diamond wire sawing is the Swiss company Meyer Burger.

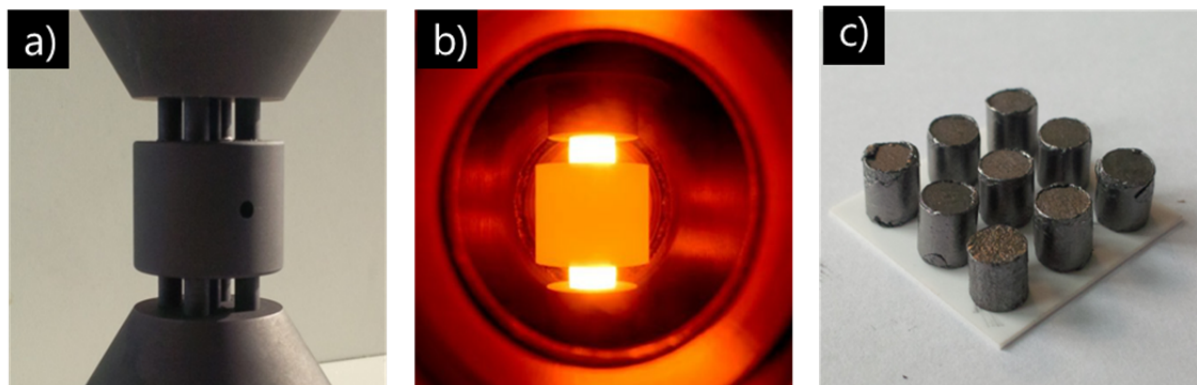


Figure 18: a) Custom-designed graphitic carbon pressing tools enabling the simultaneous fabrication of 5 cylindrical thermoelectric legs, b) spark plasma sintering furnace, c) Half-Heusler thermoelectric legs fabricated with the net shape manufacturing technique.

We also attempted in unifying all three manufacturing steps of the module, i.e. sintering, shaping, and brazing, into one single step. To implement this additive manufacturing strategy for thermoelectric modules, we developed a compressible matrix, in which holes are drilled which are subsequently filled with Half-Heusler powder. In a second step the Half-Heusler material is compacted together with the sacrificial matrix, which is then removed.

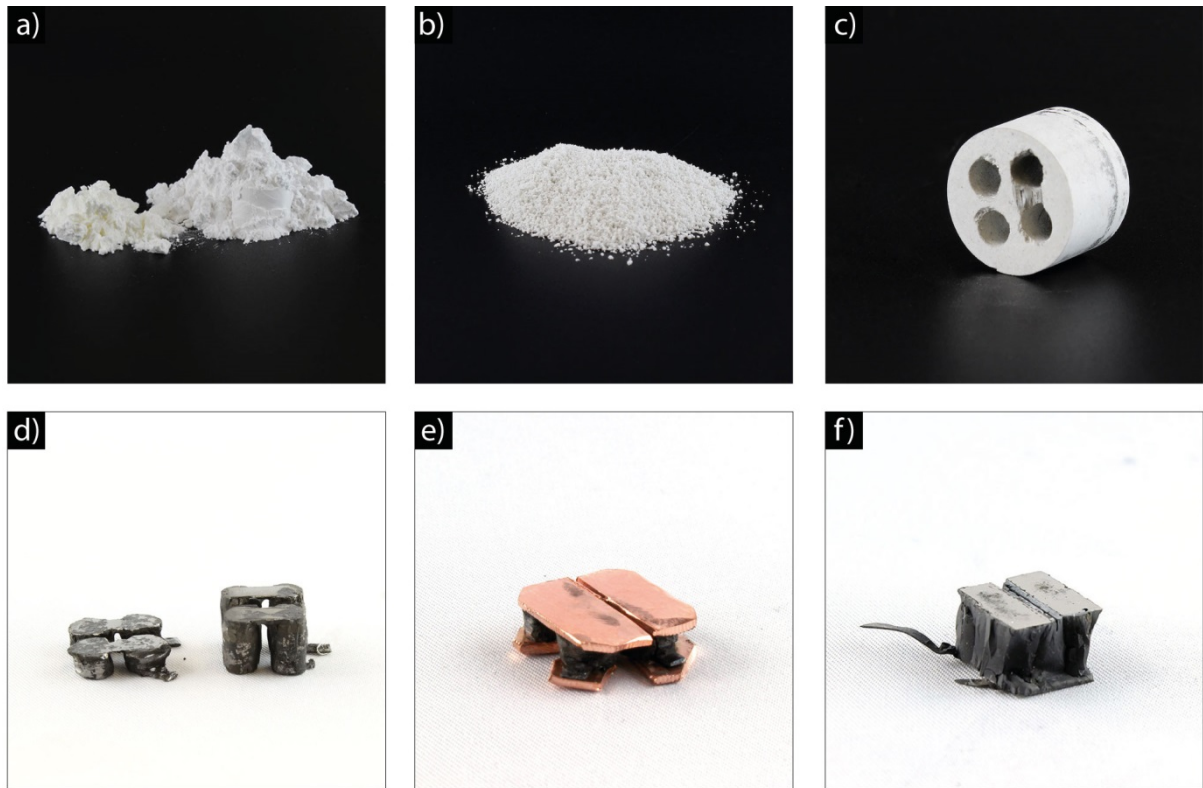


Figure 19: a) Dextrine and AlO_2 powders are prepared as a b) moist powder which can be pressed into the shape of a c) sacrificial matrix in which holes are drilled. By filling the matrix with p- and n-type powder and connecting the cylinders with Ti plates, d) thermoelectric modules can be sintered in one step. e) To lower the thermal resistance it is possible to braze Cu plates to the modules. f) Alternatively, the matrix can be made from Y-stabilized ZrO_2 .

The sacrificial matrix consists of dextrine and AlO_2 powder ($<10\text{ }\mu\text{m}$ powder size) in a ratio (w/w) 1:4 to 1:3 (Fig. 19a). The ratio will determine the compressibility of the matrix during the sintering since dextrine decomposes at 293°C . In a next step, water is added to make viscous slurry. The slurry is partially dried and compressed several times with a mortar, and then passed through a 0.5 mm sieve to achieve a moist powder (Fig. 19b). Using teflon tools, the powder is pressed (3 MPa) into the matrix shape. In the final step, the matrix (Fig. 19c) is filled with p- and n-type Half-Heusler powder and holes are connected with Ti plates. The modules are sintered at 980°C under a pressure of 50 MPa . The residuals of the matrix can be removed easily. In Fig. 19d two net shape modules are shown that have been fabricated with different dextrine: AlO_2 mixing ratios. More dextrine (1:3 compared to 1:4) has been used for the module which is more strongly compressed (left). To lower the thermal resistance additional Cu plates can be brazed onto the modules (Fig. 19e). The matrix can also be shaped using Y-stabilized ZrO_2 powders. After sintering, however, removing the ZrO_2 turns out to be difficult (Fig. 19f).

At the current stage of this investigation, the performance of the net shape modules is still relatively low. Strategies to reduce Ohmic losses described below that proved effective in the standard modules have however not yet been implemented in these modules. Yet the presented technique opens up many possibilities to optimize device performance and leaves room to test a variety of module structures (e.g. tubes with alternating p- and n-type rings etc).

2.3 Modelling assisted thermoelectric module design

In order to provide design principles for thermoelectric modules and identify and eliminate performance bottle necks, a 3D multi-physics model within the Comsol environment was built and validated by comparison to experiment. Before discussing the Comsol model, we discuss an analytical model that gives a good estimation for the optimum number of legs that should be integrated into a module.

Fig. 20 depicts the schematics of a thermoelectric generator (TEG) attached to a load with resistance R_L . The TEG is modelled as a voltage source U_0 with an internal resistance R_S . Through the load resistance R_L flows an electrical current I , with a voltage U built up through it.

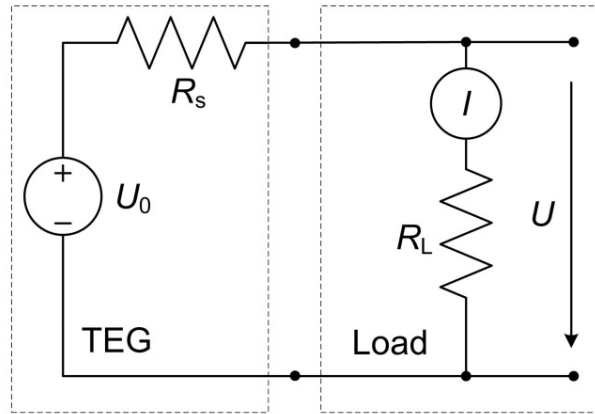


Figure 20: Schematics of the TEG on the left side with a load attached on the right side. The voltage source has a potential U_0 and an internal resistance R_S . The current I flows through the load resistance R_L . The voltage at the load side is U .

The load power $P_L = U \cdot I$ can be calculated knowing the open circuit voltage U_0 (which can be easily measured on the module test bench); the current is inversely proportional to the series resistances $I = \frac{U_0}{R_S + R_L}$ and the voltage $U = U_0 \cdot \frac{R_L}{R_S + R_L}$ follows a potential divider scheme. Therefore the load power is equal to $P_L = U_0^2 \cdot \frac{R_L}{(R_S + R_L)^2}$. It can be derived that the peak power P_{\max} condition is met when the source resistance matches the load resistance $R_L = R_S$, the equation can be thus rewritten as:

$$P_{\max} = U_0^2 \cdot \frac{R_S}{(R_S + R_S)^2} = \frac{U_0^2}{4 \cdot R_S} = \frac{U_0^2}{4 \cdot (R_{\text{legs}} + R_{\text{contacts}})}$$

The source resistance R_S is composed of the resistance of the legs R_{legs} added to the sum of all resistances R_{contacts} resulting from the contact between the legs and the wiring required to connect the module to the equipment that measures its performance. The open circuit voltage is temperature dependent and can be estimated with the help of the measured Seebeck coefficient S_n and S_p of the n-type and p-type material, respectively.

$$P_{\max} = \frac{U_0^2}{4 \cdot (R_{\text{module}} + R_{\text{wiring}})} = \frac{\left(N_{\text{legs}} \cdot \int_{T_c}^{T_h} |S_n(T)| + S_p(T) dT \right)^2}{8 \cdot \left(\left(\frac{1}{\sigma_n} + \frac{1}{\sigma_p} \right) \cdot \frac{N_{\text{legs}} \cdot L_{\text{leg}}}{A_{\text{leg}}} + R_{\text{contacts}} \right)}$$

R_{legs} is proportional to the number of the legs N_{legs} and leg height L_{leg} and it is inversely proportional to leg area A_{leg} and electrical conductivity σ_n and σ_p of the leg material. The voltage generated by a p- and n-type leg pair from our baseline process with a hot side temperature of 600°C and a cold side

temperature of 30°C is typically about 131 mV. This means that in the best case a 4x4 and 6x6 legs module will generate an open circuit voltage of 1.048 V and 2.358 V respectively.

To achieve the maximum output power for a module an optimization of the number of legs for a given area of the module was performed. Fig. 21 depicts the leg configuration in a 4x4 legs module. For the calculation a square module area with side length a is assumed. The assembly process of a module requires a minimum spacing between the legs, this distance is the variable d that can vary depending on the assembly method employed.

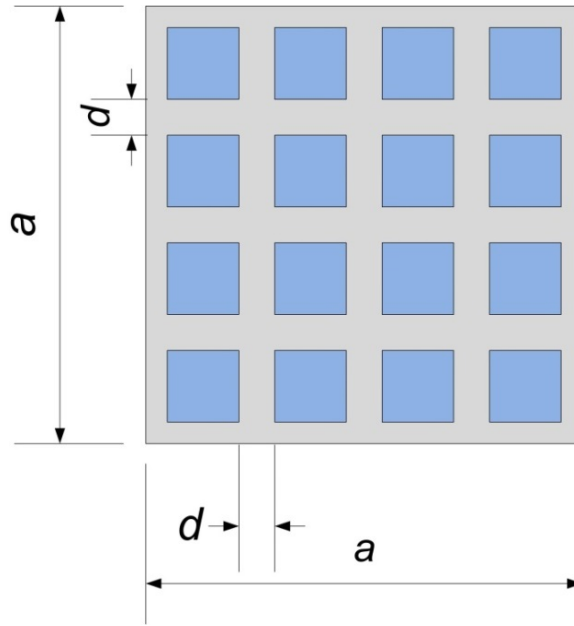


Figure 21: Schematics of a 4x4 legs module with side length a and leg spacing d .

The third variable is the number of legs N_{legs} . Using a mean value of the electrical conductivity for the n-type material σ_n and for the p-type material σ_p the resistance of the legs of the module can be expressed as follows:

$$R_{\text{legs}} = \left(\frac{1}{\sigma_n} + \frac{1}{\sigma_p} \right) \cdot \frac{N_{\text{legs}} \cdot L_{\text{leg}}}{2 \cdot A_{\text{leg}}}$$

the height L_{leg} of the leg is independent from the other variables but the base area A_{leg} of the leg is a function of a , d and N_{legs} as follows:

$$A_{\text{leg}} = \frac{1}{N_{\text{legs}}} \cdot \left(a - \sqrt{N_{\text{legs}}} \cdot d \right)^2$$

The maximum power output is then given by

$$P_{\text{max}} = \frac{\left(N_{\text{legs}} \cdot \int_{T_c}^{T_h} |S_n(T)| + S_p(T) dT \right)^2}{16 \cdot \left(\left(\frac{1}{\sigma_n} + \frac{1}{\sigma_p} \right) \cdot \frac{N_{\text{legs}} \cdot L_{\text{leg}}}{\frac{2}{N_{\text{legs}}} \cdot \left(a - \sqrt{N_{\text{legs}}} \cdot d \right)^2} + R_{\text{contacts}} \right)}$$

Employing a fixed a and a fixed d , it is possible to find the optimal number of legs.

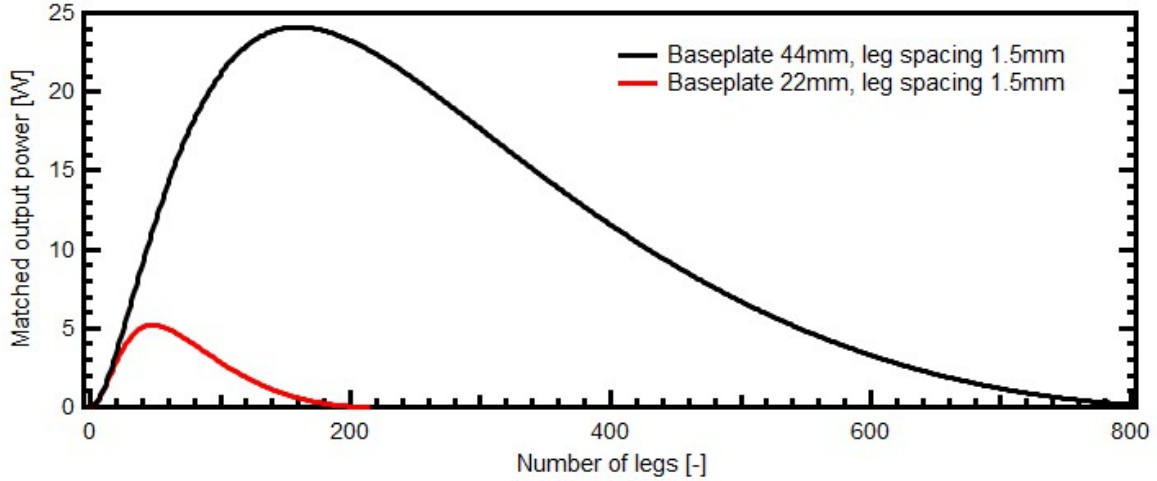


Figure 22: Output power as a function of number of legs for module base width of 22 mm and 44 mm respectively and a leg spacing of 1.5 mm

The number of legs to reach maximum output power can be evaluated from Figure 22 assuming a heat flux source sufficiently powerful to establish a temperature difference of 575°C across the module. For a module base width of 22 mm and 44 mm the number of legs corresponding to maximum, i.e. matched output power at a temperature difference of 575°C is 50 and 130 legs respectively.

The model incorporates the exact geometric details and measured physical properties for all materials including the layer sequence in the contacts (see section 2.1). For rapid screening through physical and geometrical property spaces, the model is fully parametrized. The module is embedded into a virtual test bench which can either impose a constant hot side and cold side temperature and adjusts the heat flux accordingly or fixes the heat flux and the cold side temperature and determines the resulting hot side temperature.

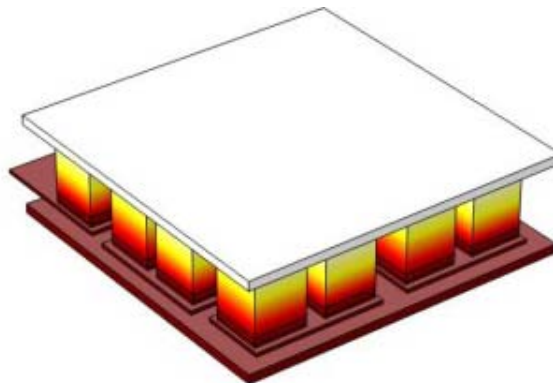


Figure 23: Temperature distribution modelled for a thermoelectric generator.

Thermoelectric material properties are taken from measurements with temperature dependent Seebeck coefficient (S), thermal and electrical conductivity (κ , σ) as described in section 2.1. The working principle is seen by looking to the heat transport equation which is solved for each node:

$$\rho C_p \frac{dT}{dt} - \nabla \cdot (\kappa \nabla T) = \frac{j^2}{\sigma} - ST\sigma(\nabla V + S\nabla T)$$



The left side of the equation describes conductive heat transport in a closed system. The right side represents the heat source from joule heating ($\frac{j^2}{\sigma}$) and heat sink due to the thermoelectric effect ($ST\sigma(VV + SVT)$). Since the model completely neglects radiative heat losses, it assumes that there is no heat transfer to the surroundings. At an upper operating temperature of 600°C this leads to an error involved in this method. The introduction of an empirical scaling parameter connected to the module voltage corrects this error and guarantees a solution of the differential equations with a reasonable relative resolution and within an acceptable time frame.

To validate the model and adjust the voltage scaling parameter, experimentally measured current-voltage characteristics of several module designs were compared to simulated modules. Fig. 24a and b show the comparison between measured and uncorrected modelled output data for a 16 legs module exposed to a temperature difference of 575°C. The value of the simulated current-voltage curve in a) differs by +16% at 0.4 V to the measured current response. A similar behaviour can be seen in the corresponding power output estimation. The predicted matched maximum output power of 0.83 W is 16% higher than the measured 0.70 W.

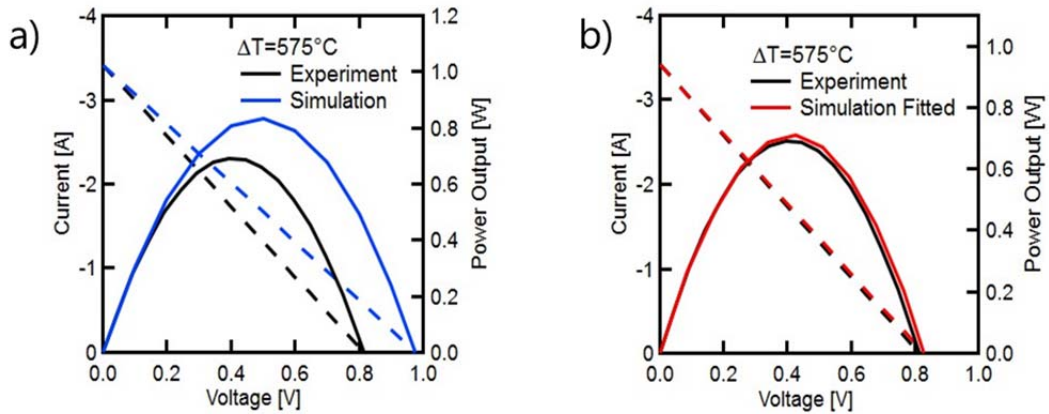


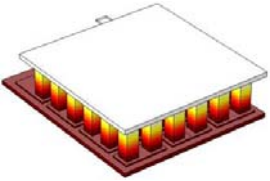
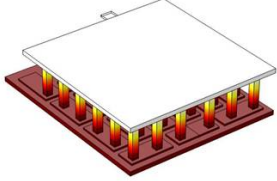
Figure 24: Modelled and measured current-voltage and power-voltage curves for 16 legs modules (4x4 mm² individual leg area) at ΔT of 575°C without (a) and with voltage scaling factor (b) factor taking into account radiative heat losses.

The deviation in power output occurs mainly due to the higher calculated voltage resulting from the higher temperatures on the hot side due to the lack of radiation heat losses in the model. By scaling the voltage with a factor of 0.85 a good approximation of the current voltage and power-voltage curves can be observed (compare Fig. 24a and b). Almost identical slopes indicate a comparable inner resistance. The corrected module voltage leads to a power output estimation within an error of +2% for results predicted by the simulation.

Due to the parametric nature of the model, parameters such as “leg area”, “leg height” and “leg count” can be varied to gain a better understanding of their impact on module power output depending on voltage, current, heat flow, and electric and thermal resistances. As a reference module, a 36 legs module with 2x2 mm² leg area is chosen which, as we will show, offers the best compromise in terms of performance, manufacturability, and mechanical robustness.

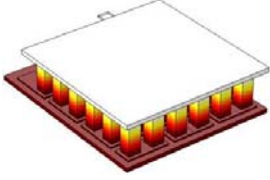
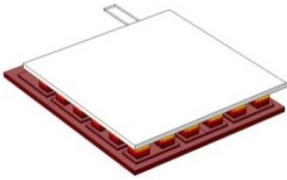
Reducing the leg area of a 36 leg module by a factor of 4 (from 2x2 mm² to 1x1 mm² per leg), decreases the heat flux by almost a factor of 4 as well (see Tab. 4). Interestingly, the current reduces by only a factor of 2 due to the increased electrical resistance of the smaller legs. Therefore current scales with electrical resistance not the leg area if voltage is kept constant. Applying a constant ΔT of 575°C, the voltage remains identical for both modules, leading to an overall reduction in module power output by a factor of 2.

**Table 4: Variation of the parameter “leg area”**

		
Total leg area	1.44 cm ²	0.36 cm ²
Leg height	4 mm	4 mm
$P_{\max} @ \Delta T$	3.3 W @ 575°C, T_c : 30°C 1 V, 3.3 A, 2.3 W/cm ²	1.6 W @ 575°C, T_c : 30°C 1 V, 1.6 A, 4.5 W/cm ²
U_0	2.1 V	2.1 V
$\dot{Q}_{\text{module, top}}$	113 W _{th} @ 3.3 W _{el}	31 W _{th} @ 1.6 W _{el}
R_i	0.35 Ω	0.72 Ω

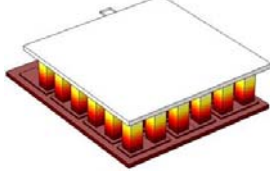
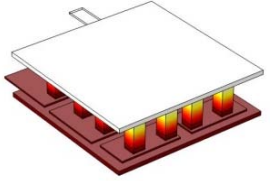
Reducing the leg height from 4 mm to 1 mm leads to a significant increase in heat flow (see Tab. 5). Consequently the temperature difference across the thermoelectric material, while remaining constant on the extremities of the module, decreases. This can be concluded from the decreased open-circuit voltage U_0 . The reduction of the leg height also leads to a reduction in electrical resistance from 0.35 Ω to 0.26 Ω due to a shorter overall current path in the resistive leg materials. Overall the decreased electrical resistance does not compensate the smaller ΔT . Consequently a decrease in power output by 10% is observed.

Table 5: Variation of the parameter “leg height”

		
Total leg area	1.44 cm ²	1.44 cm ²
Leg height	4 mm	1 mm
$P_{\max} @ \Delta T$	3.3 W @ 575°C, T_c : 30°C 1.0 V, 3.3 A, 2.3 W/cm ²	3.0 W @ 575°C, T_c : 30°C 0.8 V, 3.8 A, 2.1 W/cm ²
U_0	2.1 V	1.8 V
$\dot{Q}_{\text{module, top}}$	113 W _{th} @ 3.3 W _{el}	342 W _{th} @ 3 W _{el}
R_i	0.35 Ω	0.26 Ω

Reducing the number of legs from 36 to 16 legs leads to the expected decrease in module voltage and heat flow (see Tab. 6). The area of each individual leg is kept constant here. The decreased leg number is therefore directly proportional to the heat flow through the module and the module voltage. The maximum matched output power decreases substantially by a factor of 3. The electrical resistance decreases compared to the reference case. But the voltage loss dominates, thus reducing output power. In other words, there is a trade-off between voltage gain vs. the added resistance resulting from the larger number of legs.

**Table 6: Variation of the parameter “leg count”**

		
Total leg area	1.44 cm ² (36 legs)	0.64 cm ² (16 legs)
Leg height	4 mm	4 mm
$P_{\max} @ \Delta T$	3.3 W @ 575°C, T_c : 30°C 1.0 V, 3.3 A, 2.3 W/cm ²	1.1 W @ 575°C, T_c : 30°C 0.45 V, 2.6 A, 1.8 W/cm ²
U_0	2.1 V	1.0 V
$\dot{Q}_{\text{module, top}}$	113 W _{th} @ 3.3 W _{el}	50 W _{th} @ 1.1 W _{el}
R_i	0.35 Ω	0.2 Ω

From above results the following conclusions can be drawn

1. The current in the module is directly related to the module's internal resistance and generated voltage.
2. A large ΔT is in our case more favourable than a large heat flow.
3. It is favourable to design modules providing higher voltage as long as internal resistance does not dominate. Ohmic losses may significantly limit module performance due to the high current densities (>80 A/cm² at the maximum power point for the reference 36 legs module!!).

Based on these conclusions, the number of legs was increased from 16 to 36 and the area of individual leg was reduced to decrease the heat flux and obtain a higher ΔT .

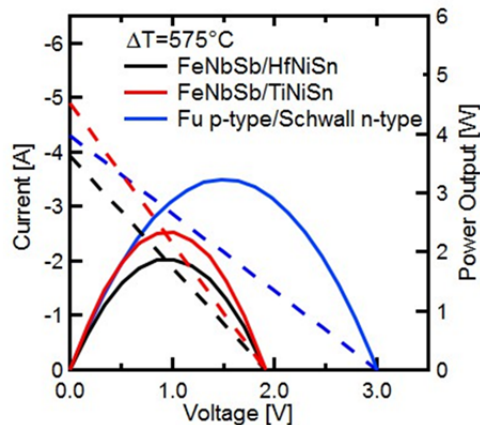


Figure 26: Simulated power output for modules with Zr- and Hf-containing (black), Zr- and Hf-free (red) n-type baseline material in conjunction with p-type baseline material as well as best reported Half-Heusler thermoelectric materials (blue) according to Schwall *et al.*¹¹ (best n-type), C. Fu *et al.*²¹ (best p-type)

After the computational optimization of the module platform with $Zr_{0.4}Hf_{0.6}NiSn_{0.98}Sb_{0.02}$ n-type material, also modules with Zr- and Hf-free n-type material $Ti_{0.33}Ni_{0.35}Sn_{0.32}Sb_{0.007}$ were investigated numerically

using the multi-physics model. Figure 26 and Table 7 show the performance of $\text{Ti}_{0.33}\text{Ni}_{0.35}\text{Sn}_{0.32}\text{Sb}_{0.007}$ (red) compared to the Hf-containing (black) standard n-type material $\text{Zr}_{0.4}\text{Hf}_{0.6}\text{NiSn}_{0.98}\text{Sb}_{0.02}$ both in combination with p-type $\text{FeTi}_{0.2}\text{Nb}_{0.8}\text{Sb}$. Basis for the simulation was materials transport properties from Fig. 15 and 16 discussed in section 2.1. This materials data was incorporated into a simulation of a 36 legs module with a leg size of $1.75 \times 1.75 \text{ mm}^2$ (total leg area 1.1 cm^2) and a temperature difference of $575 \text{ }^\circ\text{C}$ with cold side temperature of $30 \text{ }^\circ\text{C}$ imposed. The simulation results show an increase in maximum power output by 25% from 1.87 to 2.33 W when changing from the Hf-containing to the $\text{Ti}_{0.33}\text{Ni}_{0.35}\text{Sn}_{0.32}\text{Sb}_{0.007}$ n-type material. The power gain is mainly due to the improved electrical conductivity and therefore reduced overall module resistance. This can be seen in the higher current flowing at short-circuit condition in the I-V plot in Fig. 26. In addition, the blue curves in Fig. 26 show the simulated performance for the same simulated 36 legs module using the materials data for the best reported Half-Heusler materials according to M. Schwall et al.¹¹ (Schwall n-type), C. Fu et al.²¹ (Fu p-type). It can be seen that the power output is further increased by almost 40% from 2.33 to 3.20 W even though the module resistance increases from 0.39 to $0.69 \text{ }\Omega$. The reason for that is a substantially larger Seebeck coefficient that leads to an increased open circuit voltage of 3.00 V.

Table 7: Comparison of the simulated 36 legs modules

	FeNbSb/HfNiSn	FeNbSb/TiNiSn	Fu p-type/Schwall n-type
Total leg area	1.1 cm^2 (36 legs)	1.1 cm^2 (36 legs)	1.1 cm^2 (36 legs)
Leg height	4 mm	4 mm	4 mm
Conditions	$\Delta T = 575 \text{ }^\circ\text{C}$ ($T_H = 605 \text{ }^\circ\text{C}$, $T_C = 30 \text{ }^\circ\text{C}$)		
P_{\max} ($P_{\max}/\text{leg area}$)	1.87 W (1.70 W/cm^2)	2.33 W (2.12 W/cm^2)	3.20 W (2.91 W/cm^2)
U_0	1.91 V	1.92 V	3.00 V
$\dot{Q}_{\text{module, top}}$	82 W_{th} @ 1.87 W_{el}	94 W_{th} @ 2.33 W_{el}	76 W_{th} @ 3.20 W_{el}
R_i	$0.49 \text{ }\Omega$	$0.39 \text{ }\Omega$	$0.69 \text{ }\Omega$

Above considerations assume a fixed ΔT of $575 \text{ }^\circ\text{C}$ and, if necessary, infinite heat flux to maintain this temperature difference. In a real system, the heat flux may be limiting. In a water cooled system, the heat flux is limited by the capability of the hot side heat exchanger to extract heat from the exhaust gas stream. To match the module design to the heat exchanger developed in this project by Autoneum (see section 3.2), the 3D multi-physics model for the thermoelectric modules was extended by including the heat transfer coefficient determined for the heat exchanger designed by Autoneum in a 3D simulation taking into account the exhaust gas stream parameters extracted from a 1D model developed by Empa's Advanced Powertrain Technologies Laboratory (see section 3.2). Fig. 27 summarizes the working principle.

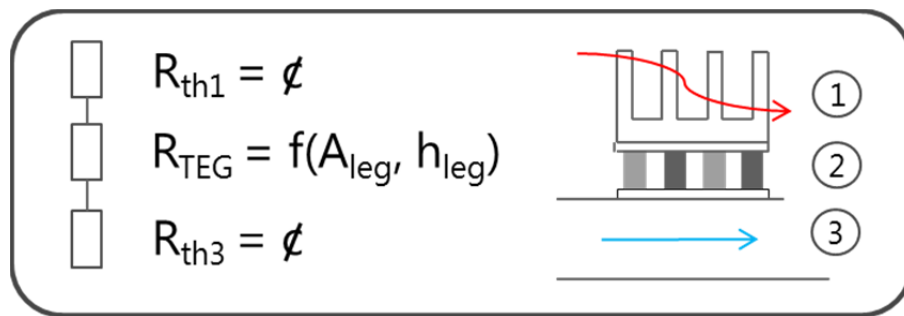


Figure 27: Working principle of the extended multi-physics model. Heat transfer coefficients extracted for the hot side and cold side heat exchangers are coupled thermally in series to the thermoelectric module simulation.

This extended model is capable of calculating the optimum module configuration for a given heat exchanger pair to obtain maximum matched output power as a function of leg area, leg height, leg



number given a specified set of thermoelectric materials. Inspection of Fig. 28, which provides output power data as a function of leg area and leg height for a 36 legs module, reveals that for a large leg height and a small leg area, the benefits resulting from the low heat flow and consequently high temperature difference is compensated by the increasing electrical resistance. For short legs with large leg area, the power output also drops significantly due to the large heat flux through the module and resulting small temperature difference even if the electrical resistance is small. Optimum performance is obtained for a leg area near 1.1 cm^2 and a leg height of 4-5 mm as implemented in the modules described in section 2.1.

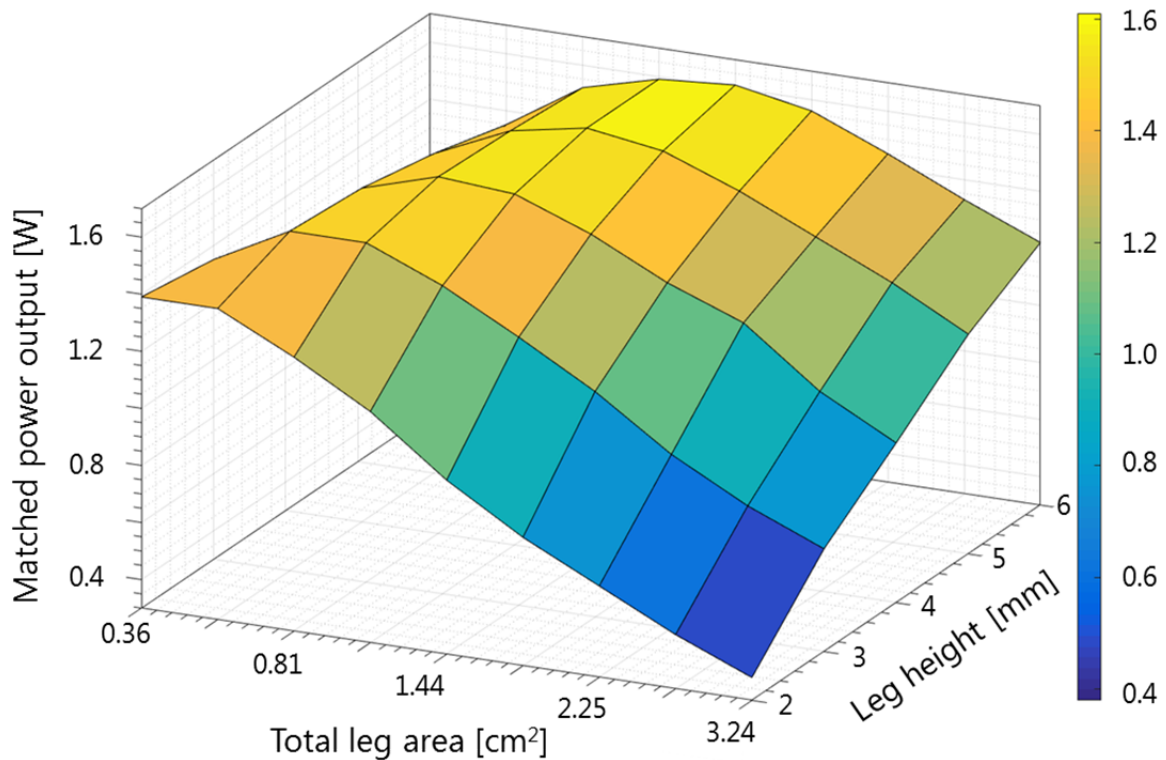


Figure 28: Simulated matched electrical output power as a function of leg area and leg height for a 36 legs Half-Heusler module.

The results obtained with the VW Touran on the dynamometer with the heat exchanger described in chapter 3.2. are in good agreement with the simulation. Module 1 and 2 in the after-catalyst heat exchanger were built with Zr- and Hf-free n-type $\text{Ti}_{0.33}\text{Ni}_{0.35}\text{Sn}_{0.32}\text{Sb}_{0.007}$ and p-type $\text{FeTi}_{0.2}\text{Nb}_{0.8}\text{Sb}_{0.007}$, a total leg area of 1.1 cm^2 (36 legs) and a leg height of 4 mm to fit the calculated optimal power output determined by simulation (Fig. 28). To allow further investigation of actual module and heat exchanger performance module 3, 4 and 5 have been built with the same materials but with a smaller total leg area of 0.81 cm^2 (36 legs) at the same leg height of 4 mm. Module 5 suffered an early failure and is not taken into account for further analysis. As can be seen from Fig. 29, the modules with the smaller legs did not perform as well as the first two modules showing a reduction in maximum matched power output of 25%. This is not only due to the fact that these modules are located further downstream in the exhaust and have seen a lower temperature difference. The open-circuit voltage, from which the temperature difference can be determined, shows a decrease of 7% between the first and last module in the heat exchanger even though a smaller amount of heat is conducted from the hot side via the smaller legs. The decreased leg area leads further to an increased module resistance and to an up to 20% decreased current, explaining the reduced power output. At a constant exhaust gas temperature at the heat exchanger inlet of 635°C , 575°C at the exit and a cold side temperature of 90°C , the average temperature difference at the thermoelectric modules is 410°C . As expected this temperature difference is not constant. The first module sees a hot side temperature difference of 430°C , while the last module only sees 390°C due to the 60°C temperature drop in the exhaust gas along the heat exchanger. This lead to a measured average maximum matched power output of 1.65 W for module 1



and 2. Looking at the surface plot in Fig. 28 the expected maximum matched power output per module with corresponding geometry was expected to be around 1.5 W. This modules' power output and current-voltage curves are shown in Fig. 29 (red). The simulation result for the Modules 1 and 2 were obtained with an exhaust gas temperature of 635 °C, a hot side heat transfer coefficient of 833 W/m²K, a cold side heat transfer coefficient of 2400 W/m²K, and a cold side temperature of 70 °C. For the simulation of Modules 3 and 4 the hot side gas temperature has been reduced to 575°C according to the measurement taking into account the further downstream position. The heat transfer coefficients on hot and cold side remained at the above stated values. The results show a slightly under estimated power output with a decreased open circuit voltage indicating a lower ΔT than measured. Further and detailed dynamometer results including the maximum matched power output of the thermoelectric modules during a World Harmonized Light Duty Vehicles Test Cycle (WLTC) are presented and discussed in detail in section 4.2.

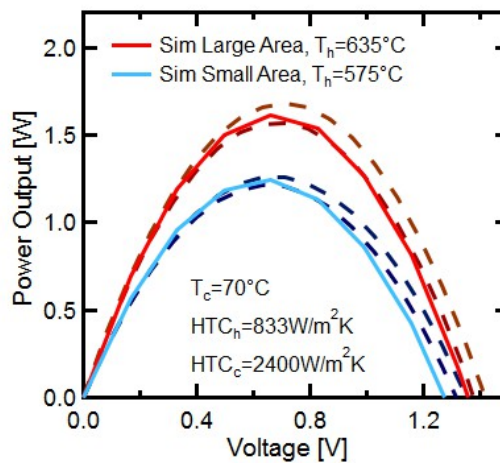


Figure 29: Measured and simulated power output in heat exchanger for modules 1 and 2 (dark red dotted, total leg area 1.1 cm², 36 legs) with corresponding simulation (red) as well as power output for the small area modules 3 and 4 (dark blue dotted, total leg area 0.81 cm², 36 legs) with corresponding simulation (blue).

In analogy to the simulation at fixed hot and cold side temperature, a simulation with the best reported Half-Heusler materials according to M. Schwall et al.¹¹ (Schwall n-type), C. Fu et al.²¹ (Fu p-type) is performed, to assess the power output potential. Fig. 30 shows the simulated power output curve of a 36 legs module in the after-catalyst heat exchanger with a total leg area of 1.1 cm² and a leg height of 4 mm. The boundary conditions (exhaust gas temperature, cold side temperature, and heat transfer coefficients) are the same as for the modules with 1.1 cm² total leg area in the heat exchanger simulation case in Fig. 29 above. The module has not been specifically matched for this task but shows nevertheless an increase in power output of 33% from 1.65 W to 2.20 W. For the low thermal and electrical conductivity of the best n-type and p-type materials, an even higher power output is expected with an optimized leg area.

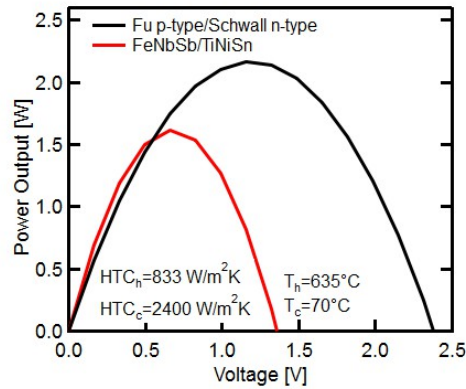


Figure 30: Simulated power output for 36 legs modules in the after-catalyst heat exchanger with best reported Half-Heusler materials according to M. Schwall et al.¹¹ (Schwall n-type), C. Fu et al.²¹ (Fu p-type) in black and modules using baseline FeNbSb/TiNiSn material in red.

2.4 Module test bench upgrades

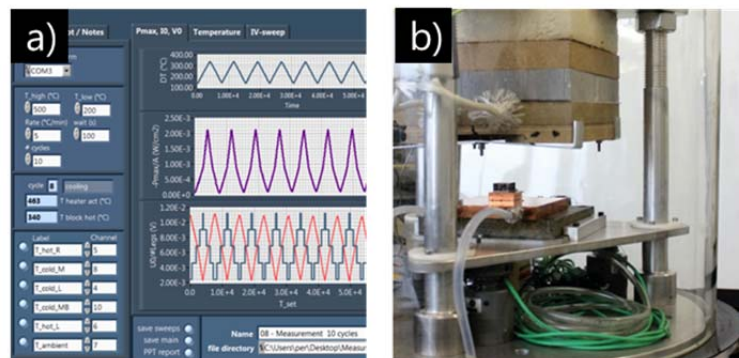


Figure 31: Upgraded thermoelectric module test bench, a) automated measurement software, b) module test bench equipped with automatic heating control.

In order to facilitate standardized module characterization, the thermoelectric module test bench developed in a previous SFOE project was equipped with an automatic heating control. A LabVIEW software solution (Fig. 31a) was programmed controlling the temperature ramping of the furnace and monitoring the power output of the thermoelectric module as a function of time and/or as a function temperature. For temperature measurements, thermocouples are installed at several points of the test bench (Fig. 31b). Standardized reports are generated automatically. The program also allows observing the effects of other external parameters such as contact pressure or convective gas flow across the module. Gas tightness was further improved to allow measurements under argon atmosphere. Fig. 31c shows typical output current and power density vs output voltage curves of a Half-Heusler module.

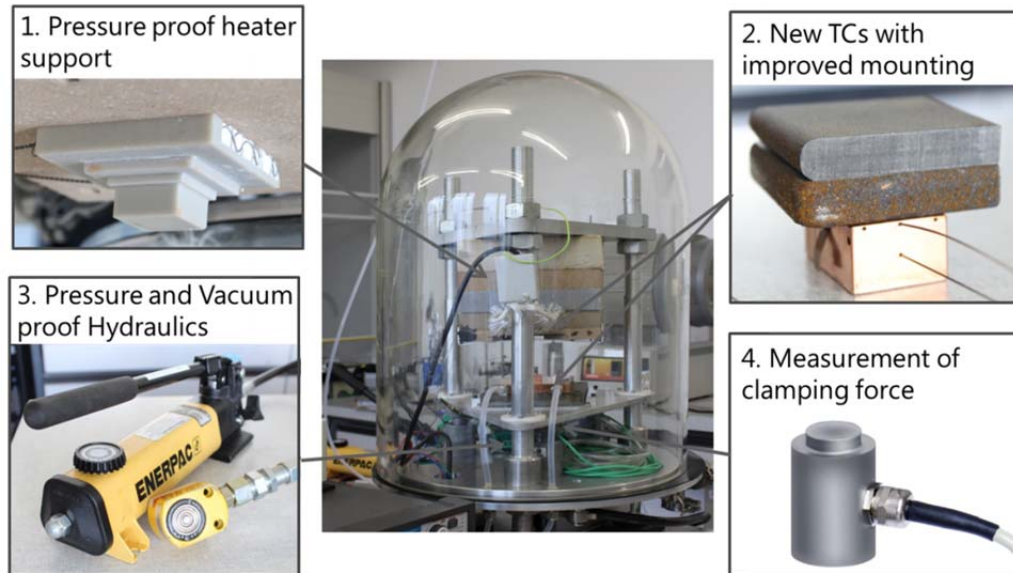


Fig. 32: Upgrades to module test bench in the second year.

The module test bench was further upgraded during the second project year to allow reproducible measurements of electrical module power output and heat flux across the modules (Fig. 32). The AlN heater block was rebuilt to ensure uniform clamping pressure on the heater block and the thermoelectric modules. Thermocouples are placed in precisely fitted drilling holes in the AlN heater and the copper cooling block to improve temperature sensing precision and reproducibility. The hydraulic piston was upgraded with a solid PTFE seal to maintain better vacuum and avoid leaking of hydraulic fluid into the evacuated area. To quantify the applied clamping force in real time a pressure sensor was integrated on top of the hydraulic piston.

3. Thermal Design and Vehicle Integration

3.1 Module integration into exhaust gas manifold

The highest temperatures in the exhaust manifold of internal combustion engines are around 850°C for diesel and 1000°C for gasoline engines. The exhaust manifold collects the gases from the individual cylinder and guides them to the downstream systems. These are in general a turbocharger (not in every vehicle) and the exhaust after treatment system, nowadays present in every vehicle.

To use the benefits of thermoelectricity at the exhaust manifold, it is necessary to redesign the manifold with a high and low temperature area between which the thermoelectric modules can be installed. The outer manifold walls can be used as the high temperature surface providing the hot side for the thermoelectric elements. Fig. 33 shows a typical manifold design of a 4-cylinder passenger car engine.

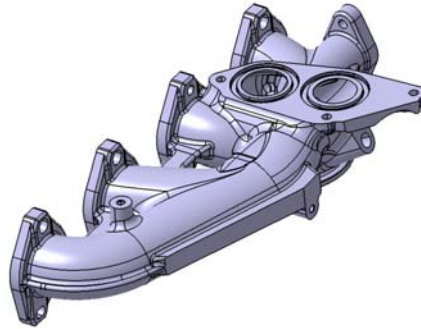


Figure 33: Typical exhaust manifold of 4-cylinder diesel passenger car engine.

During the second year of the project, different solutions and concepts mainly focusing on the feasibility of prototypes and the possibilities of industrialisation have been evaluated. One main issue was to find a proper design for the exhaust system, maximizing the contact area of thermoelectric modules taking into account space and weight restrictions of a modern powertrain configuration. Another aspect of the analysis is the feasibility of material selection and serial production.

From the analysis in section 2.3, it is apparent that the electric power output of the thermoelectric modules depends on the temperature difference between the cold and the hot side as well as on the heat flux through the elements. In the first project year, simulations have shown that only active cooling by water is able to sustain the necessary heat fluxes. In order to get the maximum temperature difference, it is necessary to integrate a cooling circuit to keep the cold side at a temperature level as low as possible. Therefore it is on hand to use the cooling water circuit of the engine. On the hot side, on the surface of the exhaust manifold, temperatures are expected to reach 800°C.

In the concept studies, the possibility to integrate the cooling system on the exhaust manifold was investigated, which is a challenge from the production point of view. Another option is the implementation of separate parts for manifold and cooling systems. This solution was selected for the prototype due to its simplicity and feasibility. The design layout is presented in Fig. 34. This prototype was produced and installed on the test vehicle for measurements. Results are reported in section 4.1

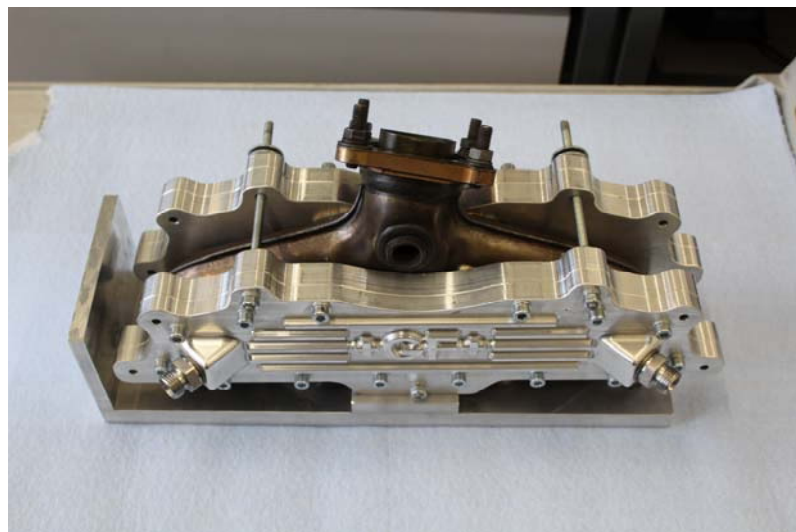


Figure 34: The design layout of the exhaust manifold with TE modules

3.2 Design and construction of heat exchanger for integration after exhaust gas manifold and impact on engine performance

In order to assess the energy that can be recuperated from the heat contained in the exhaust gas exiting a combustion engine, four different light-duty vehicles with typical state-of-the-art powertrains were selected: a small and a larger gasoline engine, a small and a larger diesel engine (Tab. 8). For these vehicles, chassis dyno measurements were performed at Empa to provide input data for the overall energy balance modelling.

Table 8: Experimental data of vehicles tested at Empa

	GA14	GA20	DI15	DI20
Fuel	Gasoline	Gasoline	Diesel	Diesel
Injection	Indirect	Direct	Direct	Direct
Displacement (cm ³)	1368	1997	1496	1995
1st enrolment	02.2014	03.2014	10.2014	09.2014
Mass (kg)	1360	1810	1250	1810
Emission code	Euro 6b	Euro 6b	Euro 6b	Euro 6b

Each of the vehicles was tested with two velocity profiles that represent standard driving cycles: Worldwide Harmonized Light Vehicles Test Cycle (WLTC) and New European Driving Cycle (NEDC), shown in Fig. 35. During the experiment, exhaust gas mass flow and temperature were measured at the end of the pipe, and data from the engine control unit were recorded.

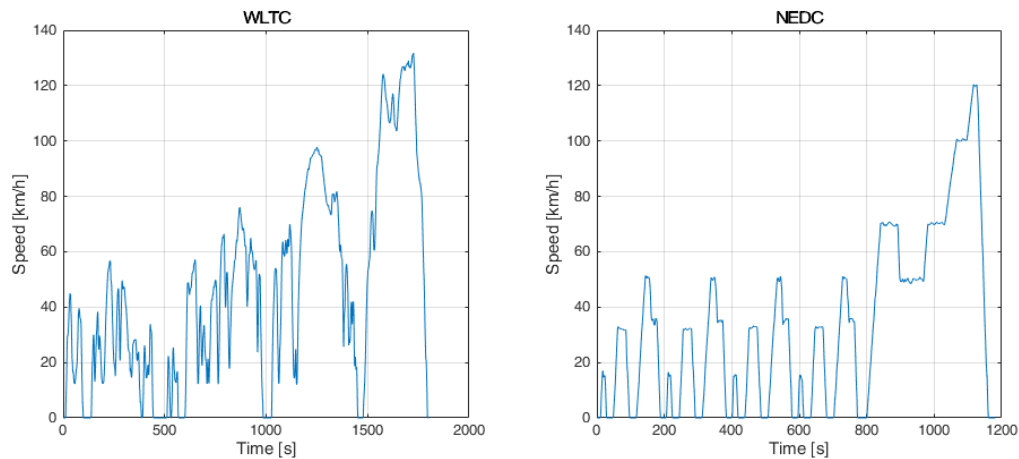


Figure 35: Velocity profile of the measured driving cycles

Two different locations were investigated for the installation of thermoelectric generators: at the manifold, and after the catalytic converter, as shown in Fig. 36.

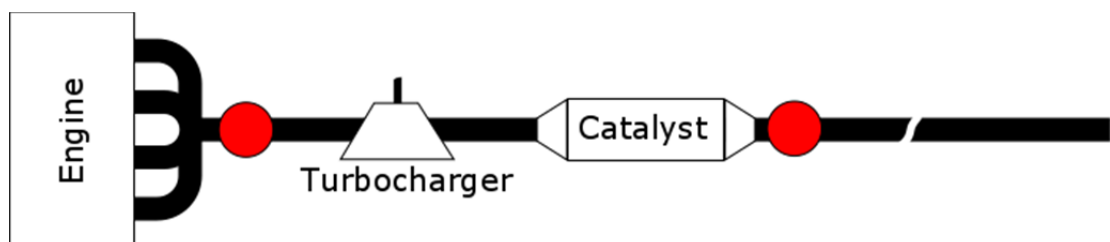


Figure 36: Locations for thermoelectric generators (red) evaluated in the model



The gas temperature at the manifold is not available from the car sensors and therefore has to be simulated. An engine model was developed to determine the manifold temperature along the driving cycle and as a function of the vehicle characteristics. The engine model uses the driving cycle speed, car characteristics, and literature diagrams to simulate the temperatures from the experimental data.

The results for the simulations for the WLTC cycle are summarized in Fig. 37. The gasoline engines produce exhaust gas at higher temperatures (some peaks are over 800 °C) than diesel engines (remains below 500 °C). For all considered engines, the highest temperatures occur in the second half of the cycles, where high engine loads occur.

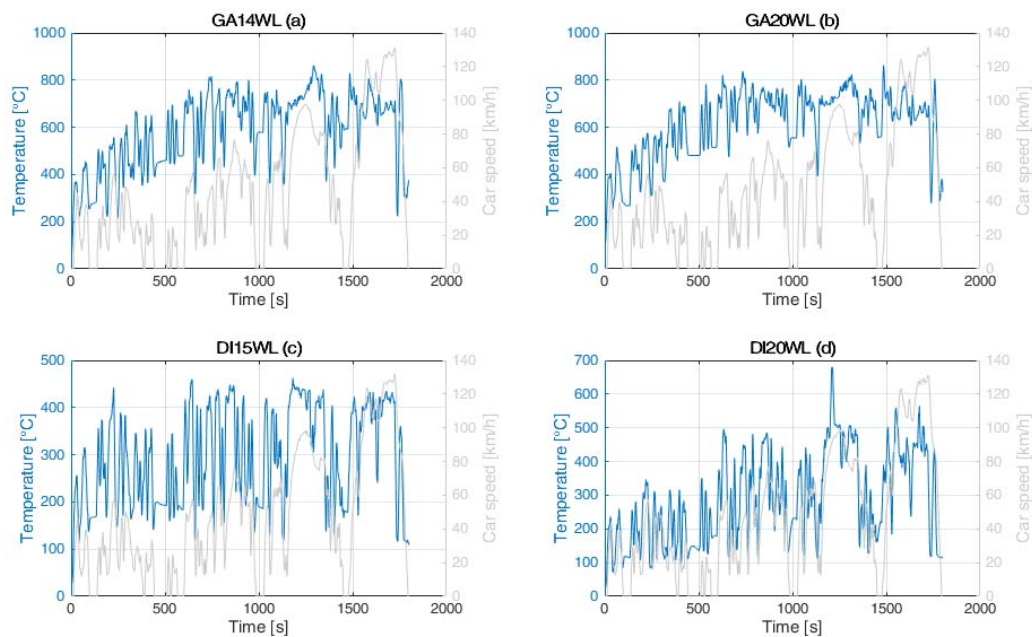


Figure 37: Simulated gas temperatures at the manifold during WLTC cycle, (a) gasoline 1.4 I, (b) gasoline 2.0 I, (c) diesel 1.5 I, (d) diesel 2.0 I.

The gas temperature after the catalytic converter was simulated based on the measured temperatures measured at the tail pipe. Convective and radiative heat transfers inside the pipe and to the environment were considered. After the catalytic converter, the temperatures of the gasoline engines are below 700 °C, while the ones of the diesels are below 400 °C, as shown in Fig. 38. Interestingly, over the three meters of exhaust pipe, the temperature of the exhaust reduces by 400 °C for the gasoline vehicles and 200 °C for the diesel vehicles. Measured exhaust gas flow is the lowest for the gasoline vehicles (around 0.01 kg/s). Diesel vehicles produce almost twice as much mass flow. Consequently, the resulting heat flow carried by the exhaust gas is comparable for all four vehicles.

A transient 1D model has been developed to study the influence of various parameters (such as geometry, flow parameters, etc, Fig. 39). The model is designed to be flexible and can be adapted to different engine and vehicle configurations. All simulations are run with a thermoelectric generator area of 30 x 30 cm² assuming materials characteristics corresponding to typical performance values of Half-Heusler materials.

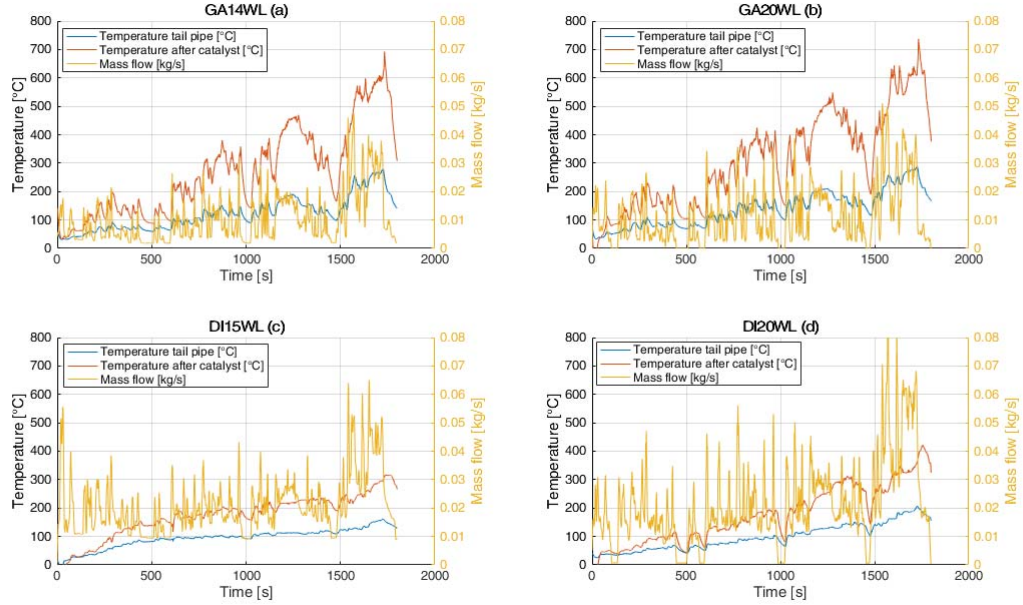


Figure 38: Simulated gas temperatures after the catalytic converter during WLTC cycle, (a) gasoline 1.4l, (b) gasoline 2.0l, (c) diesel 1.5l, (d) diesel 2.0l

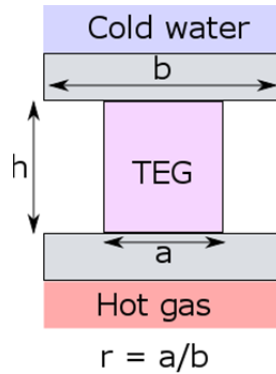


Figure 39: Generic model to simulate heat flow across thermoelectric generator (TEG).

The model takes into account the heat transfer from the hot exhaust gas to the hot side of the thermoelectric generator modelled as convective heat transfer from gas to a pipe wall. The Dittus-Boelter equation is used to compute the Nusselt (Nu) number. Reynolds (Re) and Prandtl (Pr) number are computed from the exhaust flow conditions (temperatures, mass flow, etc).

$$Nu = 0.023 * Re^{0.8} * Pr^{0.3}$$

$$Re = \frac{vL}{\nu}$$

$$Pr = \frac{c_p \mu}{\lambda}$$

Here ν is the kinematic viscosity, μ dynamic viscosity, λ thermal conductivity, c_p specific heat, v speed respectively of the exhaust gases, and L the characteristic dimension of the pipe (here 0.02 m). The temperature dependence of the gas properties was considered and taken from literature²⁵. Conduction through the thermoelectric generator element was modelled using a typical value for the thermal



conductivity of Half-Heusler materials (~ 4 W/K/m) neglecting any additional thermal resistances in this first iteration for simplicity. With this assumption, the model yields an upper bound for the performance potential of the system. Finally, the convection heat transfer from the thermoelectric generator to the cooling water was modelled using again the Dittus-Boelter equation, this time using the Reynolds and Prandtl number of water.

The results of the simulations for the gasoline 2.0 l car during the WLTC cycle, assuming a 30×30 cm² Half-Heusler based thermoelectric generator installed at the manifold, are presented in Fig. 40. The temperature on the cold side of the thermoelectric generator is almost equal to the cooling water temperature because of the good heat transfer on the cold side. On the hot side however, the temperature on the thermoelectric generator is much lower than the temperature of the gas. This is a consequence of the relatively low heat transfer between the hot gas and the pipe in the absence of additional fins and limits overall system performance. In addition, the cooling circuit causes strong cooling of the entire module in this case, where the overall thermal conductivity of the thermoelectric generator is relatively low. Heat transfer from the exhaust gas side to the thermoelectric generator needs to be improved by the incorporation of additional fins and the overall thermal conductivity of the thermoelectric generator matched to the cold and hot side heat exchangers to avoid a bottleneck in heat flow and maximize electrical output power. Nevertheless, in the current configuration without fins, the heat flowing across the thermoelectric generator can be relatively high reaching 3500 W in the second part of the cycles, resulting in an electrical power output 150 W. The trade-off between heat flux and temperature gradient will need to be optimized in the second project phase to improve the electrical output power further.

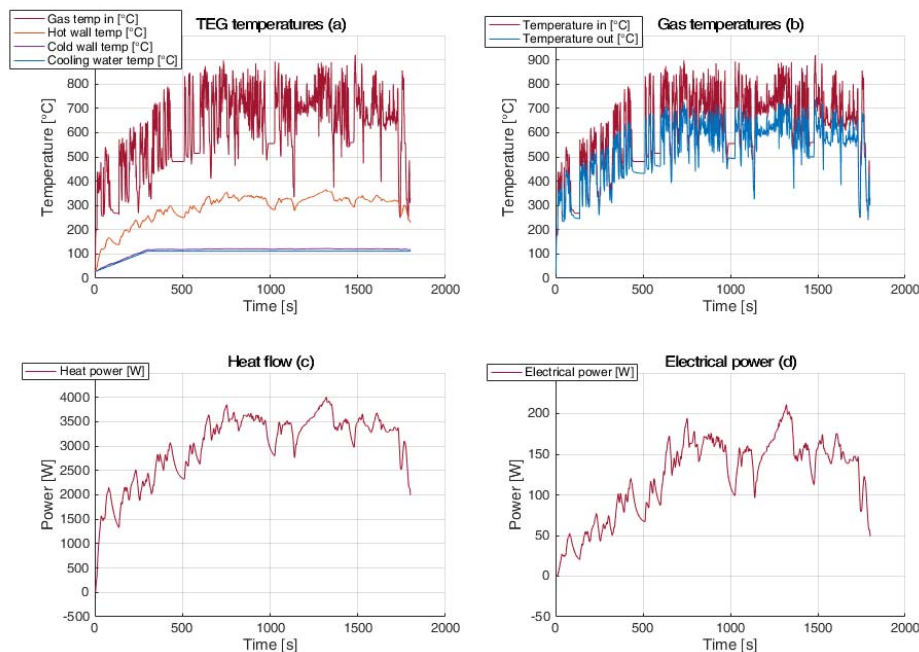


Figure 40: Results from simulation along the WLTC cycle of thermoelectric generator integrated into the manifold of a 2.0 l gasoline vehicle. (a) temperatures at different points of the thermoelectric generator system, (b) hot gas temperatures at manifold inlet and outlet, (c) heat flow through thermoelectric generator, (d) electrical power output from thermoelectric generator.

If a thermoelectric module of 30×30 cm² is installed at the manifold of the 2.0 l gasoline, the simulations show that up to 65 Wh of electricity can be recuperated from the exhaust during the full WLTC cycle.

The following paragraphs are taken from our publication, Durand *et al.*²⁴



TEG optimal dimensions

Given the thermoelectric material the thermal conductivity of the TEGs is fixed. The free parameters left for modifying the TEGs' thermal resistance are the length of the elements (in the direction of the heat flow) as well as the surface coverage.

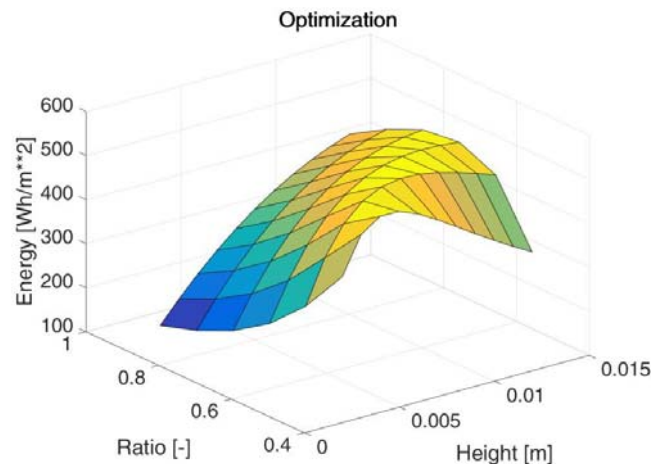


Figure 40: Influence of height and surface coverage ratio on recovered energy (gasoline 2.0 l, WLTC)

Results of the simulation at the manifold for the gasoline 2.0 l are presented in Fig. 40. Simulations show that increasing the height of thermoelectric legs, which increases the thermal resistance and consequently the temperature gradient across the thermoelectric module, improves the energy output in the height range between 3 and 6 mm. Moreover, reducing the surface coverage ratio a/b , i.e. increasing the spacing between the legs of the thermoelectric module, yields a higher electrical energy output. Note that the mechanical integrity of the module imposes constraints on the intervals accessible to these geometrical parameters. The result in Fig. 35 can be explained by the differences in heat transfer on cold and hot side. In fact, in the configuration investigated here, the convective heat transfer process from the exhaust gas to the thermoelectric generator is much weaker than the analogous process from the thermoelectric generator to the cooling water circuit. Additional fins in the exhaust gas pipe have been considered to match these two processes.

Further simulations show that the speed of the water in the cooling circuit of the vehicle has almost no influence on the system performance representing additional evidence that the cooling system is not limiting. On the other hand, the water temperature affects the electrical output power as it directly influences the conversion efficiency.

In order to generate maximum electrical output power, the temperature difference and heat flux across the thermoelectric generator must be optimized. Heat flux is maximized for a thermoelectric module with maximum overall thermal conductivity. However, this situation leads to a very low temperature gradient across the thermoelectric module and consequently low conversion efficiency. Conversely, a module with minimum overall thermal conductivity results in a high temperature gradient, beneficial to reach high efficiency, but results in small heat flux and consequently low electrical output power. The trade-off is apparent. With increasing thermal resistance, temperature difference across the modules increases, while the heat transferred decreases. Given the efficiency characteristics of the thermoelectric generators, the optimum energy recovery is reached where temperature difference and heat transferred are both at moderate levels.

This trade-off behavior is similar for all vehicles according to the measurements and associated simulations used in this study at both locations; however the optimal geometric dimensions vary as well as the amount of the recuperated energy.

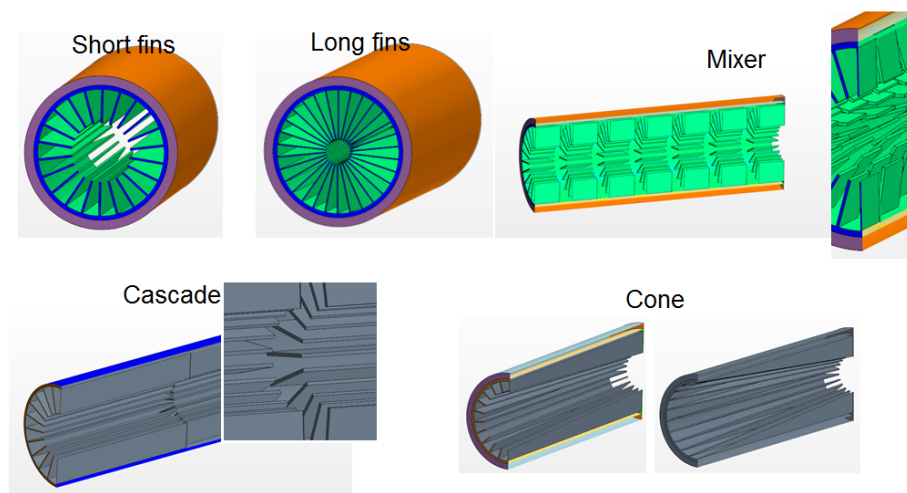
**Table 9: Optimal dimensions of TEG and energy generated during a WLTC**

Vehicle	Downstream after-treatment system		Manifold	
	Optimal dimension of leg length, coverage	Total electric energy recuperated	Optimal dimension of leg length, coverage	Total electric energy recuperated
Gasoline 1.4 l	8 mm, 60%	69 Wh/m ²	7 mm, 50%	557 Wh/m ²
Gasoline 2.0 l	9 mm, 60%	105 Wh/m ²	7 mm, 50%	643 Wh/m ²
Diesel 1.5 l	9 mm, 60%	13 Wh/m ²	8 mm, 50%	75 Wh/m ²
Diesel 2.0 l	8 mm, 60%	23 Wh/m ²	8 mm, 50%	93 Wh/m ²

Results of the optimizations are presented in Table 9: the optimal leg length is almost the same for all examined vehicles at one location (about 8 – 9 mm downstream the after-treatment system and 7 – 8 mm at the manifold). Optimal coverage ratio depends also only on the location of the module, around 60% after the after-treatment system and 50% at the manifold. The amount of energy recuperated should the thermoelectric generator elements be installed in the exhaust manifold is roughly 5 times higher than in the downstream of the after-treatment system. The energy to be recuperated in the gasoline exhaust is approximatively 5 times more in respect to the recuperated energy in the diesel exhaust.

Thermoelectric generator prototype (downstream of after-treatment system)

In this section, only the thermoelectric converter intended to be integrated downstream of the exhaust manifold and after-treatment system (ATS) will be discussed. The convective heat transfer process from the exhaust gas to the TEG was found to be much weaker than the analogous process from the TEG to the cooling water circuit. As a consequence, the implementation of fins in the exhaust pipe has been proposed to increase heat transfer from the exhaust gas to the TEGs. Using a 3D flow model, Autoneum evaluated different fin designs with respect to their thermal resistance for two given heat exchanger configurations – an optimal (cylindrical) design and a prototype heat exchanger designed at Empa intended for testing.



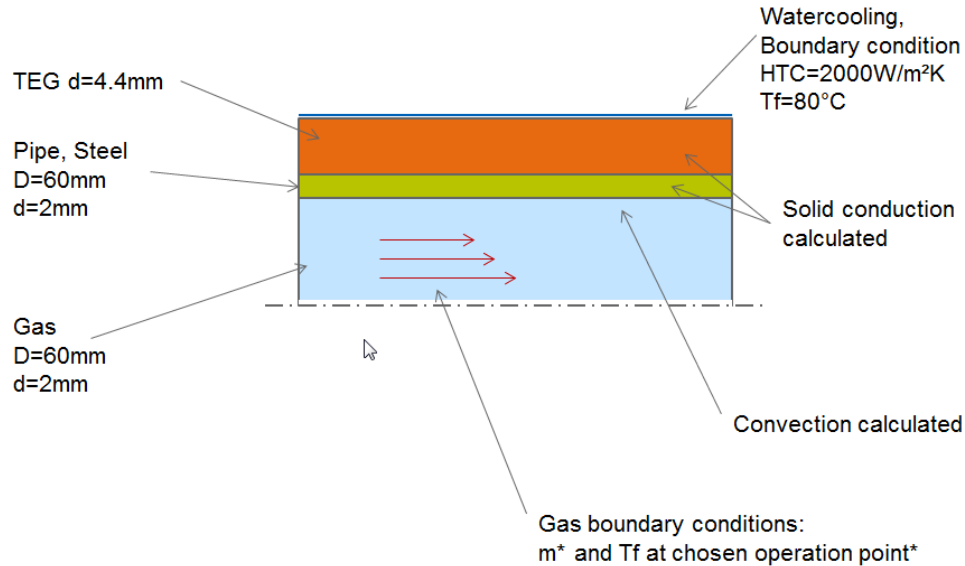


Figure 41: Fin configurations on optimal heat exchanger evaluated by Autoneum (top), physical parameters and boundary conditions used for simulation (bottom).

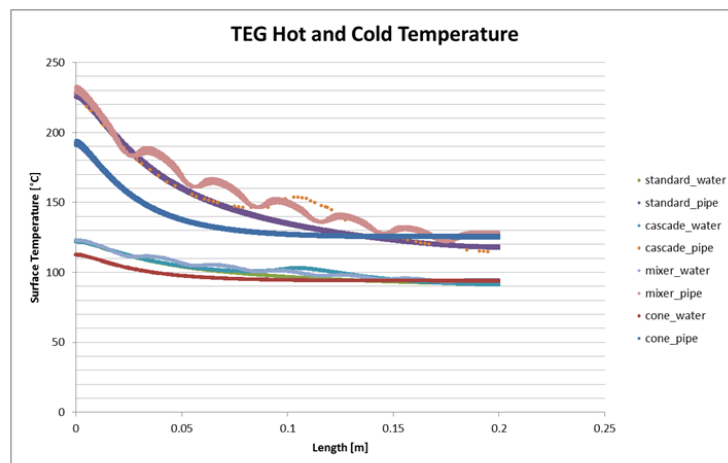


Figure 42: Temperature distribution for the various fin designs along the optimal heat exchanger during the steady-state phase in the WLTC (50 km/h, 900 – 970 s cycle time, operating point: $T_f = 576^\circ\text{C}$, $m^* = 0.09\text{ kg/s}$)

Due to manufacturability limitations, especially during the prototyping stage, the optimal heat exchanger, as predicted by the simulations, was changed. According to the optimization of the thermoelectric module dimensions, a different prototype heat exchanger has been designed and manufactured at Empa instead (Figures 43 and 44). As the development of the thermoelectric elements has not yet been finalized and thus requiring frequent modifications, the heat exchanger was designed as a modular unit that allows simple exchange of modules and fins. Moreover, emphasis has been put on keeping the thermal mass of the heat exchanger as low as possible and minimizing thermal losses by insulating the open hot surfaces and avoiding thermal conduction between the hot and cold components, forcing heat to pass through the thermoelectric elements. The fins have been produced at Empa according to Autoneum's specifications (see below).



Figure 43: Heat exchanger and TEG in disassembled state with all components displayed.

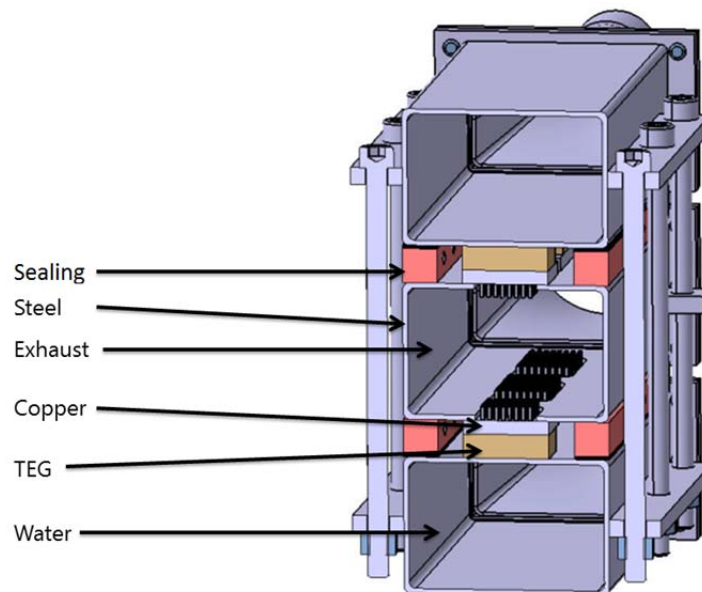


Figure 44: Cross-sectional view of the schematic representation of the heat exchanger and the TEGs. The exhaust gas channel is sandwiched between two cooling water ducts. The thermoelectric elements are located in the interstitial space, the "plenum". Copper fins protrude into the exhaust gas channel to improve heat transfer to the thermoelectric elements.

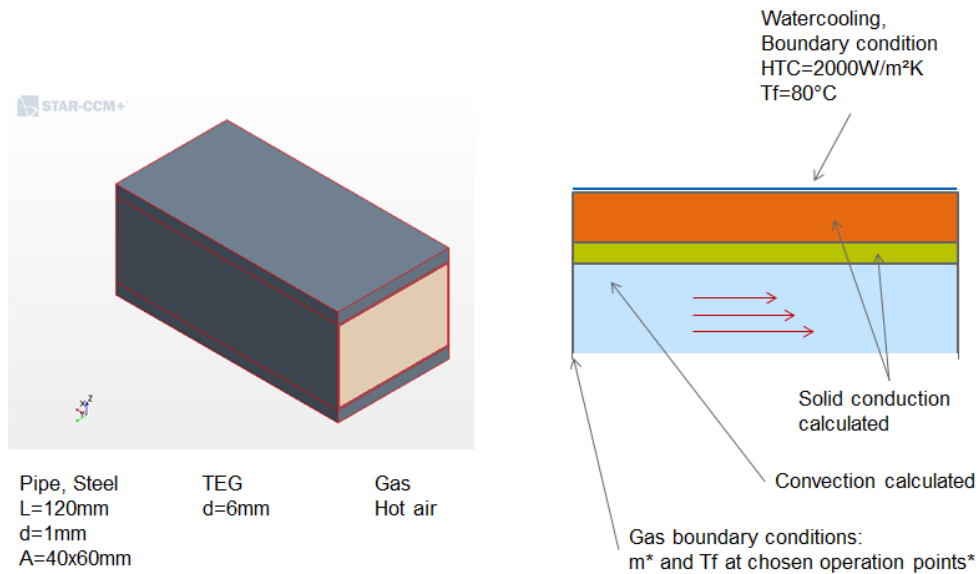


Figure 45: Physical parameters and boundary conditions used for simulation.

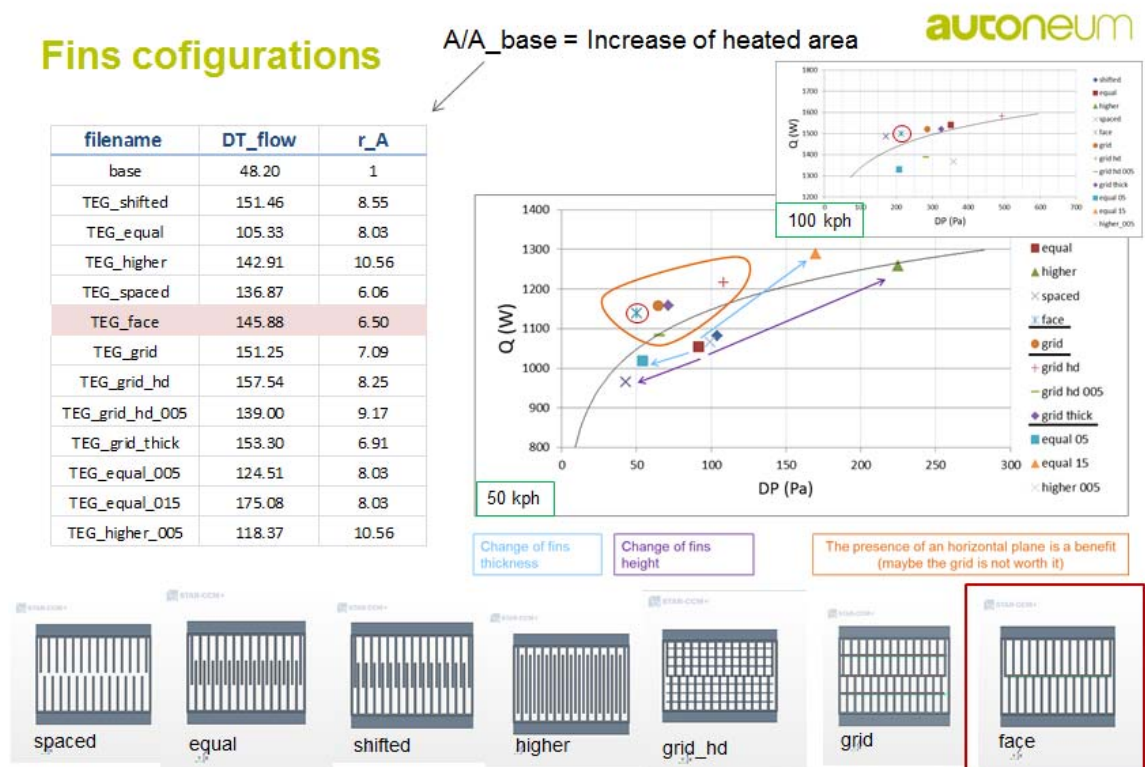


Figure 46: Evaluation of fin designs under steady-state conditions at 50 km/h and 100 km/h.

From Figure 47, it can be seen that when a single face connects the fins, improved results can be achieved under both regimes investigated (50 km/h and 100 km/h steady-state conditions). However, concerning the fin design it should be kept in mind that there are different optima depending on the gas velocity. In the higher-speed (100 km/h) and also higher exhaust gas velocities domain, the spaced configuration is superior, while the horizontal surface configuration is more efficient in the lower-speed domain (50 km/h).

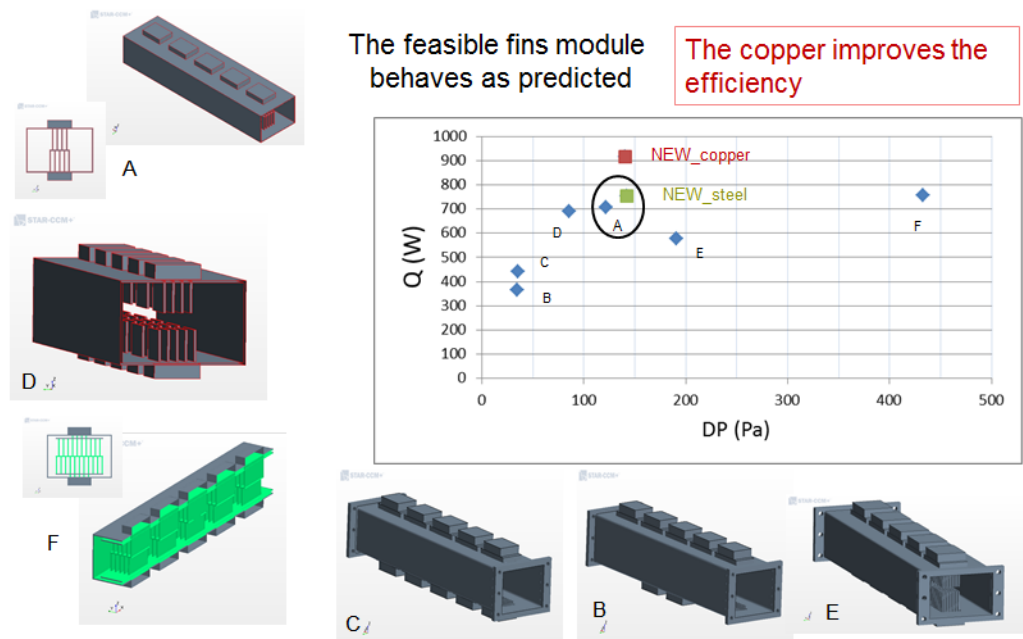


Figure 47: Results of simulations for enhancing heat transfer from the exhaust gas to the TEGs by fins avoiding excessive increase of the flow through resistance.

The blade fins are better than the fins with square section (needles). In the prototype configurations, the first module is the one with the highest difference in temperature and the difference in power obtained is proportional to the better distribution along the stream-wise coordinate.

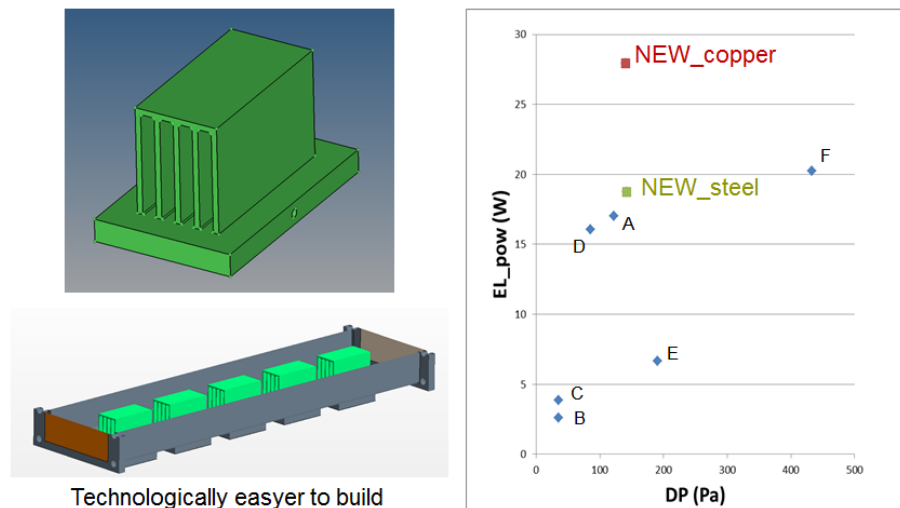


Figure 48: Final fin configuration made of copper for Empa heat exchanger prototype following optimization evaluation performed by Autoneum.

The size and weight of the TEG are appropriate for vehicle applications although related considerations have not been taken into account in the current project phase. Due to that and ease of operation, the thermoelectric generator was mounted next to the vehicle on the dynamometer. However, this further increases its distance from the manifold, leading to lower exhaust gas temperatures than initially expected in the simulation. On top of that, the airflow from the blower in front of the dynamometer further intensified the heat dissipation from the exhaust gas pipe. So the recuperated energy by the TEGs in this series of experiments is lower than in the reality.



3.3 Module integration into heat exchanger downstream of exhaust gas manifold and the related thermal management and packaging space assessment of total exhaust gas system

Parasitic heat dissipations relevant to the performance of the thermoelectric converter have been assessed and can be categorized as follows:

Piping

Heat loss occurs along the exhaust gas pipe from the engine to the thermoelectric converter. Since the thermoelectric converter is currently not integrated into the vehicle, the pipe is more exposed to external influences (e.g. air flow) and its length is considerably increased. As a preventative measure, the pipe has therefore been insulated.

Experiments have shown that the initial design of the cooling water ducts needs further improvement. For a required coolant flow rate of 0.4 L/min in the downstream after-treatment system configuration, the cross-sectional area of the ducts is too large. To prevent this problem in future applications, the dimensions of the cooling water ducts must be optimized and adapted to the required cooling load.



Figure 49: The diverted exhaust gas pipe connected to the TEG is encircled. In this image, the cooling water circulation has been disconnected.

Casing

Conduction through the casing as well as radiation from the hot to the cold side of the heat exchanger leads to a reduction in the temperature gradient as well as the heat conducted across the thermoelectric elements. Ideally, all heat exchanged between the exhaust gas and the cooling water should be channeled through the thermoelectric elements to maximize their efficiency. Parasitic heat transfer from the hot to the cold side has been assessed in specific experiments by removing all thermoelectric elements and placeholder dummies and measuring relevant temperatures and heat fluxes. Corrective measures may be taken accordingly.



Figure 50: Side view of the heat exchanger: Note the insulation covering the hot exhaust gas pipe to prevent parasitic heat transfer to the cooling water through the bolts.

The heat exchanger is designed to minimize thermal conduction by decoupling the hot exhaust gas pipe from the cooling water ducts. The assembly is held together by bolts on either side of the heat exchanger that provide the necessary clamping force on the thermoelectric elements. In the design of the heat exchanger special attention was paid to these issues. In particular, the bolts (Fig. 43, 44 and 50) have been designed in order not to conduct any heat from the hot to the cold side. The bolts only come into contact with the upper and lower cooling water ducts. Additional insulation prevents exposure of the bolts to radiation from the hot exhaust gas pipe (Figure 50).

Leakage

The sealing of the thermoelectric elements from the hot exhaust gas side is a major challenge. Insufficient sealing leads to intrusion of exhaust gas into the “plenum” where the elements are placed. A reduction of the temperature gradient across the thermoelectric elements can be expected. During test runs, a temperature drop up to 40° C at the hot side of the TE elements was observed due to leaks. The design of targeted sealing in this environment with severe temperature alternations is necessary.

Oxidation of thermoelectric modules

Using the thermoelectric modules at high hot side temperatures leads to high power output but bears the risk of strong oxidation if the modules are directly exposed to air. On the test bench, the modules are usually tested under vacuum but when they are mounted to the exhaust of a car for example, air is present containing oxygen, which reacts with the Half-Heusler materials to form an oxide layer. The higher the temperature, the more severe the oxidation reaction. Fig. 51a shows a broken module after a measurement at high temperature and ambient atmosphere. When air reaches the legs, their surface becomes oxidized. The thickness of the resulting oxide layer increases with time and increases the internal resistance of each leg due to its insulating nature.

To prevent air from reaching the exposed module legs, a commercial ceramic paste was used as filler (Fig. 51b). Two filling levels were used, namely partially encapsulated, where only the outermost row of legs was covered with paste, and fully encapsulated, where all the space between the legs was filled. The modules with different protection level were placed on the test bench and heated up to 500 °C under vacuum. Reaching the top temperature, the test chamber was filled with air and the internal resistance and power output was measured in dependence of air exposure time. Fig. 51c and d show the results of this measurement. The formerly low internal resistance of the unprotected module (bare) increases immediately from the moment on that air enters the system. It increases further with time due to oxidation of the legs until it passes 1 Ω which causes a power loss down to less than 20 % of its initial value in only 40 min.

The importance of an oxidation protection becomes clear when comparing the bare to the partially encapsulated module. The initial internal resistance of 0.13Ω is kept over 30 min of extensive heating under air. The ceramic protection around the outer legs inhibits oxidation by sealing the module. The fully encapsulated module starts at higher internal resistance probably due to lower contacting quality but it clearly shows that the ceramic paste prevents oxidation for an even longer time. The power loss could therefore be avoided by both, partial and full encapsulation. It is concluded that such a ceramic encapsulation around the outer leg row is sufficient to prevent power loss resulting from oxidation, as long as the ceramic paste fully separates the legs from air.

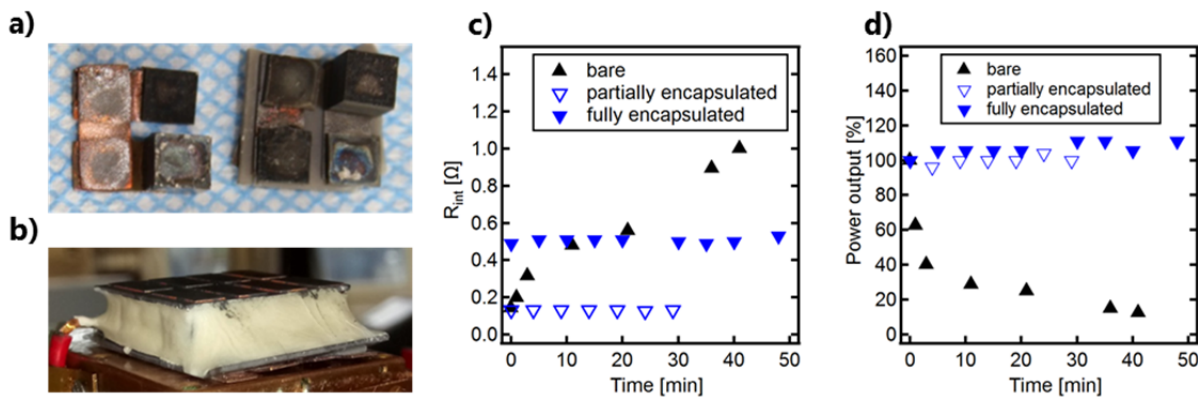


Figure 51: Oxidation protection; a) oxidized and broken module legs after exposure to air at high temperatures, b) module encapsulated with protective ceramic paste c) internal resistance and d) power output as a function of time of bare, partially and fully encapsulated modules.

3.4 Design water cooling circuit

The ability of the thermoelectric converter to generate electrical power is dependent on the presence of a temperature gradient that is applied to the thermoelectric elements. In the annual report 2016, air cooling resulted in insufficient heat fluxes for this application. Therefore, the prototype was implemented with water cooling. To simulate real-world conditions, the cooling water flow through the heat exchanger is established by connecting the thermoelectric converter to the Empa cooling water network with a temperature control unit (Model 90S, Regloplas AG, St.Gallen). To maximize the temperature gradient across the thermoelectric elements and to compensate for the lower-than-expected hot side exhaust gas temperature (see Task 3.2), the temperature of the cooling water was set to 50°C instead of a more realistic 90°C in typical vehicle situation.

4. Evaluation and validation

4.1 Adaptation of chassis dynamometer system, performance evaluation under standard driving cycles, energy balance assessment for thermoelectric system integrated into exhaust gas manifold

An existing vehicle from the inventory of Empa's Automotive Powertrain Technologies Laboratory (see Table 10) was adapted to supply engine exhaust heat to the thermoelectric modules integrated into the exhaust manifold. To generate a temperature gradient across the thermoelectric modules, cooling water is supplied to the manifold via a cooling circuit as shown in Fig. 34 in counter-flow configuration connected to a temperature control unit (see Task 3.4). The experiments involved measurements of module power output at constant vehicle speed of 100 km/h and over the WLTC.

**Table 10: Technical data of the vehicle used for the experiments at Empa**

Manufacturer	Volkswagen
Model	Touran 2.0 ecofuel
Fuel	CNG
Injection	Indirect
Displacement	1984 cm ³
Rated power	80 kW (@ 5400 rpm)
Rated torque	160 Nm (@ 3500 rpm)

Table 11: Electric power output of the four Half-Heusler modules mounted on the exhaust manifold for the constant speed (100 km/h) test.

Constant 100 km/h	Module 1	Module 2	Module 3	Module 4	Mean
Mean power [W]	1.1	0.7	0.3	0.6	0.7
Power density [kW/m ²]	1.9	1.2	0.5	1.1	1.2

Shown in Table 11 are module power output values for the four Half-Heusler modules mounted on the exhaust manifold of the VW Touran driving at a speed of 100 km/h on the dynamometer. Each module consists of 36 legs, each with area $1.75 \times 1.75 \text{ mm}^2$. The four modules perform quite differently, probably due to variations in contact pressure under these harsh thermal and vibrational conditions. Module 1 performs comparably well, with an output power of 1.1 W corresponding to a power density of 1.9 kW/m^2 (module area 5.7 cm^2). Module 3 produces the lowest power output. The following discussion is based on the output power value of module 1 as there is no scientific reason, why this value could not be achieved also by the other three modules mastering the engineering challenges.

Maximum open-circuit voltage values for these Half-Heusler modules can be estimated from the Seebeck coefficients given in Fig. 15c. At hot side temperatures of 520°C measured on the manifold close to the modules, the Seebeck coefficient for p-type and n-type Half-Heusler is about $140 \mu\text{V/K}$ and $-140 \mu\text{V/K}$, respectively. At cold side temperatures of about 90°C , the Seebeck coefficient is $75 \mu\text{V/K}$ for the p-type and $-100 \mu\text{V/K}$ for the n-type. This results in an average Seebeck coefficient of about $230 \mu\text{V/K}$ per p-n pairing. Thus at a temperature gradient of about 430°C , a 36 legs Half-Heusler module delivers a maximum open-circuit voltage of 1.8 V. From inspection of Fig. 52, it can be seen that module 1 reaches a maximum open-circuit comparable to this value, albeit at higher hot side temperature. The temperature drop between thermoelectric legs and point of temperature measurement is difficult to assess in this configuration.

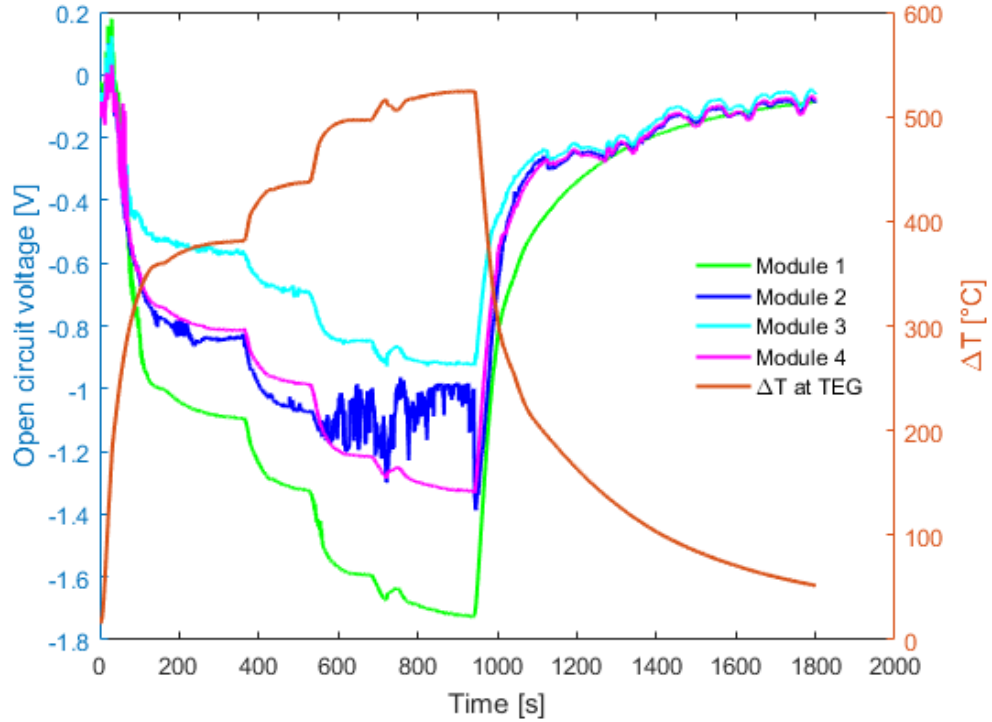


Figure 52: Open-circuit voltages and temperatures differences between the cold and hot side of thermoelectric modules during a constant driving cycle (100 km/h, 120 km/h, 140 km/h and 150 km/h)

Table 12: Electric energy and power output of each Half-Heusler module mounted on the exhaust manifold over the WLTC.

WLTC	Module 1	Module 2	Module 3	Module 4	Mean
Total energy [kJ]	1.4	0.8	0.2	0.7	0.8
Mean power [W]	0.8	0.4	0.1	0.4	0.4
Power density [kW/m ²]	1.4	0.7	0.1	0.7	0.7

Output power and energy collected over the full WLTC cycle, are summarized for each module in Table 12. The average power output is 0.8 W for module 1 over the 30 min of the WLTC cycle, corresponding to a power density of 1.4 kW/m². These values, averaged over the WLTC cycle, correspond to almost 75% of the values measured during steady-state operation at 100 km/h. Over the full WLTC cycle a total electric energy of 1.4 kJ is recuperated for module 1.

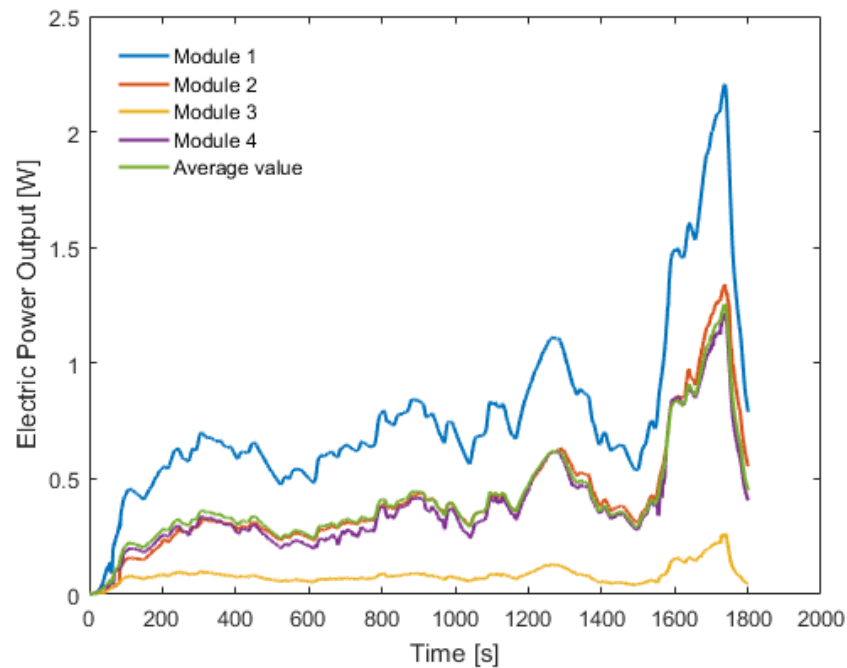


Figure 53: Transient electric power output of each thermoelectric module mounted on the exhaust manifold during the WLTC.

The transient electric power output of each thermoelectric module mounted on the exhaust manifold is plotted over the full WLTC in Figure 53 and correlates positively with measured exhaust gas temperatures. The generated electric power varies significantly during the WLTC cycle. During the first 600 s, the power generated is very low. Later in the cycle and with increasing engine loads, the generated power output increases, peaking at 2.2 W for module 1 right before the final deceleration phase.

Figure 54 displays the efficiencies of the thermoelectric modules, defined as the ratio of the generated electric power produced by the module to the thermal power through the module. The thermal power through the modules is calculated according to Eq. (0) and Eq. (0). The efficiency is found to be positively correlated to the temperature difference between the hot and cold side of the TEG. The efficiency is in particular low when the temperature difference is below a certain threshold, as observed during the first half of the cycle. The highest efficiency is found right before the last deceleration phase of the WLTC cycle, peaking at 2.8%. It is clear from these results, that the WLTC, although adopted by the automotive industry, is a very unfavorable test protocol for thermoelectrics, as high temperatures are only reached during the last phase.

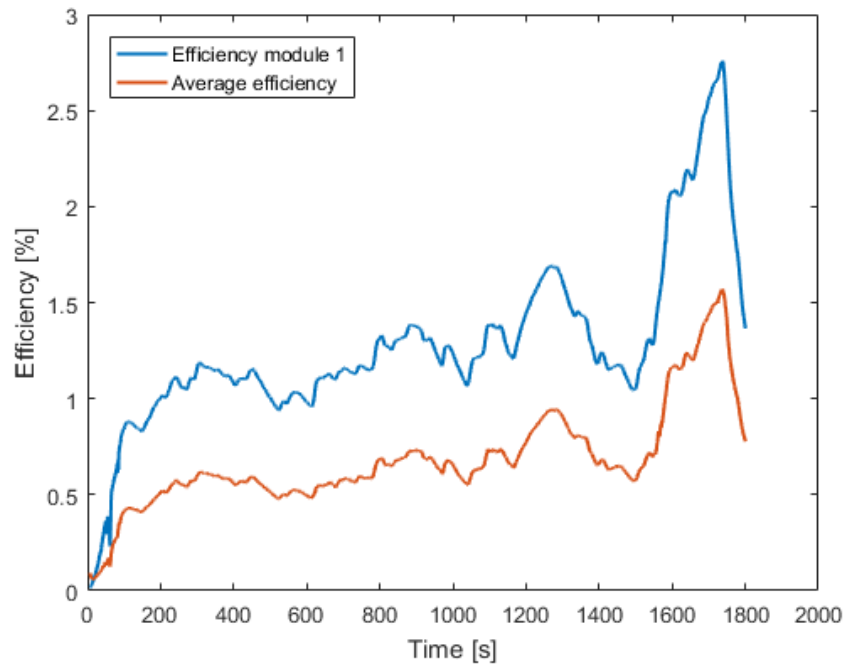


Figure 54: Efficiencies of TEG modules mounted on the exhaust manifold for the WLTC cycle

4.2 Adaptation of engine or car test stand system, performance evaluation under standard driving cycles, energy balance assessment for thermoelectric system integrated downstream of exhaust gas manifold

The thermoelectric modules integrated into the heat exchanger mounted after the catalytic converter are again supplied with exhaust gas heat from a vehicle described in Table 10 on a dynamometer. To generate a temperature gradient, cooling water is supplied to the heat exchanger via a cooling circuit in counter-flow configuration connected to a temperature control unit (see Task 3.4) and introduced into the heat exchanger in a counter-flow configuration (see Task 3.2). A schematic of the test rig setup is shown in Figure 55. Depending on the experiment, the heat exchanger is equipped with fully functional thermoelectric modules and/or dummies. The material for the dummies has been selected to match the thermal conductivity of the Half-Heusler material used for the thermoelectric modules. Temperature and pressure sensors in all relevant locations ensure that a subsequent analysis and energy balance calculation can be performed. The experiments involved measurements of module power output at constant vehicle speed of 100 km/h and over the WLTC.

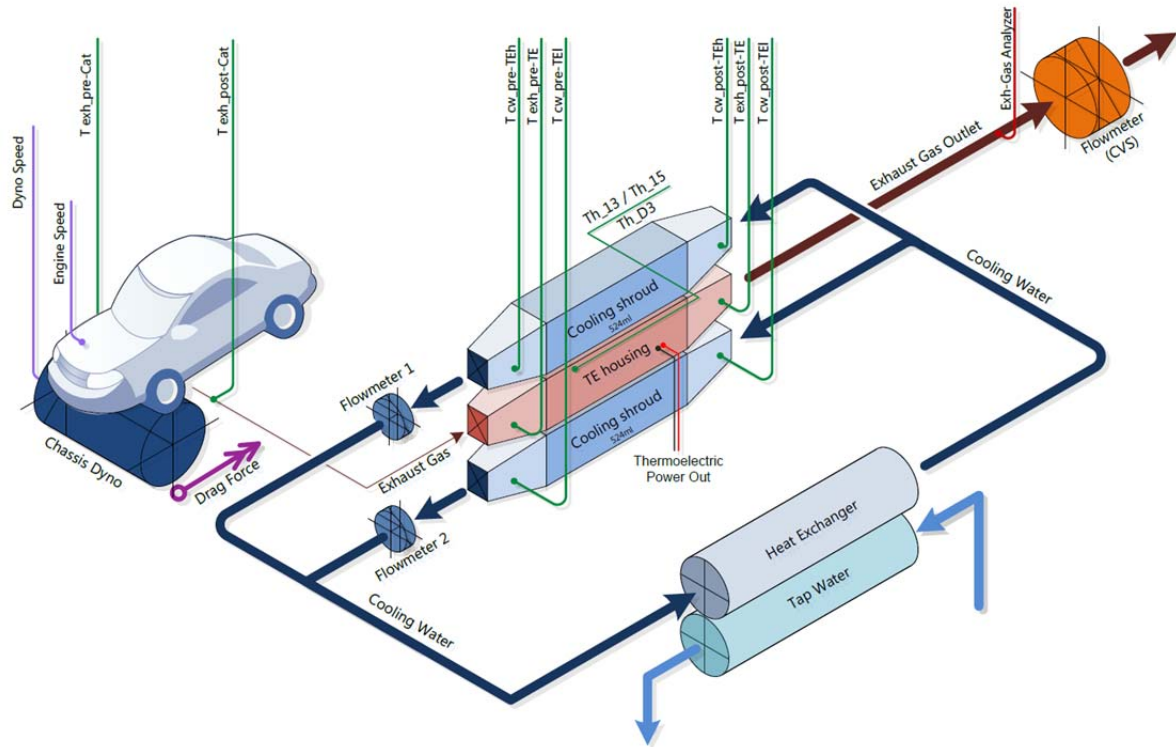


Figure 55: A schematic representation of the test rig configuration. The labeled lines depict the sensor data being logged.

Table 13: Measurement data for constant driving conditions recorded on the test rig (VW Touran, 100 km/h)

Temperature	Inlet [°C]	Outlet [°C]	ΔT [°C]	\dot{Q} [W]
Exhaust gas	635	575	60	2158
Thermoelectric module	520 (hot side)	90 (cold side)	430	728

Tab. 13 shows the measured temperature values for the constant driving condition. The exhaust gas temperatures correspond to a vehicle speed of 100 km/h. The exhaust gas mass flow corresponds to 120 km/h in order to compensate the temperature loss of 125 °C due to the additional piping that was introduced between the exhaust gas after-treatment system and the thermoelectric generator assembly for practical reasons. The exhaust temperature drops by 60 °C over the full length of the TEG assembly. The TEG assembly during this measurement consists of four Half-Heusler modules and six dummies with the comparable thermal conductivity. So the temperature drop in the exhaust gas is typical for ten modules. The exhaust gas loses a thermal power of 2158 W, when flowing through the entire TEG assembly according to Eq. (0), where the exhaust gas mass flow, the specific heat of the exhaust gas, and the temperature difference between inlet and outlet are required to calculate the heat flux extracted by the TEG assembly.

$$\dot{Q}_{ex} = \dot{m}_{ex} C_p \Delta T_{ex} \quad (0)$$



This includes losses to the environment, heat transferred through the thermoelectric modules as well as heat transferred directly to the cooling water. One third of the heat lost by the exhaust gas is transferred through the thermoelectric modules. The thermal power through an individual thermoelectric module is the sum of the heat transfer rates through all legs which are connected in parallel as shown in Eq. (0).

$$\dot{Q}_{TEG} = \sum_{i=1}^{36} \frac{\Delta T_{TEG}}{R_i} \quad (0)$$

The heat transfer rate through one leg is calculated as the ratio of the temperature difference between the hot side and cold side of the thermoelectric module to the equivalent thermal resistance of the n-type or p-type leg as shown in Eq. (3).

$$R_i = \sum_{j=1}^7 \frac{h_j}{\lambda_j(T_{TEG}) A_j} \quad (0)$$

The equivalent thermal resistance of the n-type or p-type legs is computed based on the serial connection of all layers composing the module including the AlN ceramic plates.

Under these circumstances, the heat flowing through ten modules is estimated to be 728 W. The difference between the exhaust gas temperature and the hot side of the thermoelectric module indicates the potential of an improved design of the heat exchanger. A further improved design of the heat exchanger fins has the potential to increase the hot side temperature of thermoelectric modules and decrease the gap to the inlet exhaust gas temperature.

Table 14: Electric energy and power output of each Half-Heusler module for the constant speed (100km/h) test.

Constant 100 km/h	Module 1	Module 2	Module 3	Module 4	Mean	Total (10 modules)
Mean Power [W]	1.6	1.7	1.3	1.2	1.45	14.5
Power Density [kW/m ²]	2.8	3.0	2.3	2.1	2.55	2.55

Shown in Tab. 14 are module output power values for four modules mounted on the heat exchanger integrated into the exhaust gas system of the VW Touran driving at a speed of 100 km/h on the dynamometer (temperature difference corresponding to 100 km/h, mass flow corresponding to 120 km/h). Modules 1 and 2 consist of 36 legs with area 1.75 x 1.75 mm². Within production variation of the modules, modules 1 and 2 perform comparably well, with an output power of 1.6 and 1.7 W. Output power without piping correction would be 50% of these values only. Modules 3 and 4 consist of 36 legs with area 1.5 x 1.5 mm². Also for these modules, within production variations of the modules, the module perform comparable well, with an output power of 1.3 and 1.2 W. Note that the lower output power for module 3 and 4 is not only due to the lower temperature difference available downstream of the heat exchanger assembly, but also due to the smaller sub-optimal leg area, as predicted from Fig. 28 and Fig 29. The four thermoelectric modules deliver an averaged power output of 1.45 W corresponding to a power density of 2.8 kW/m² (module area 5.7 cm²). Should all ten thermoelectric modules be installed, an average of 14.5 W of electricity can be generated. These 14.5 W generated by the 728 W heat flowing through the modules results in an efficiency of 2.0%.

**Table 15: Electric energy and power output of each TEG module for the WLTC cycle.**

WLTC	Module 1	Module 2	Module 3	Module 4	Mean	Total (10 modules)
Total Energy [kJ]	1.0	0.9	0.6	0.5	0.75	7.5
Mean Power [W]	0.6	0.5	0.3	0.3	0.43	4.3
Power Density [kW/m ²]	1.0	0.8	0.6	0.5	0.73	0.73

Output power and energy collected over the full WLTC cycle, are summarized for each module in Tab. 15. The average power output for 10 modules is 4.2 W over the 30 min of the WLTC cycle corresponding to an energy density of 0.7 kW/m². These values averaged over the WLTC cycle correspond to about 30% of the values measured during steady-state operation at 100 km/h, thus much lower than for the case, where the modules were integrated into the exhaust manifold, where a value of almost 75% was observed. Note however that these values are not corrected for the temperature drop, resulting from the additional piping, which converges to about 150 °C during the second half of the WLTC. Consequently higher output is expected for a thermoelectric generator assembly mounted directly after the exhaust gas after-treatment system. Over the full WLTC cycle a total electric energy of 2.2 Wh or 7.5 kJ is recuperated without correction.

The transient electric power output of each thermoelectric module is plotted over the whole WLTC in Fig. 56. In general, the four modules behave similarly, which are positively correlated to the exhaust gas temperature upstream of the modules (as shown in Fig. 56). The more upstream the module is located (Module 1), the more electric power the module generates during the WLTC. The average power curve lies almost in the middle of all those lines. On the other hand, the generated electric power varies significantly during the WLTC cycle. During the first 600 s, the power generated is very low. Later in the cycle and with increasing engine loads, the electric power generated increases, peaking at 2.4 W right before the last deceleration phase.

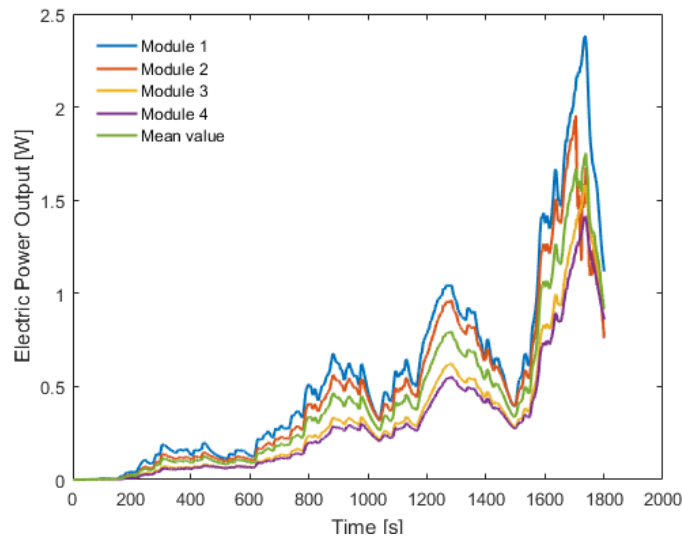


Figure 56: Transient electric power of each TEG module for the WLTC cycle

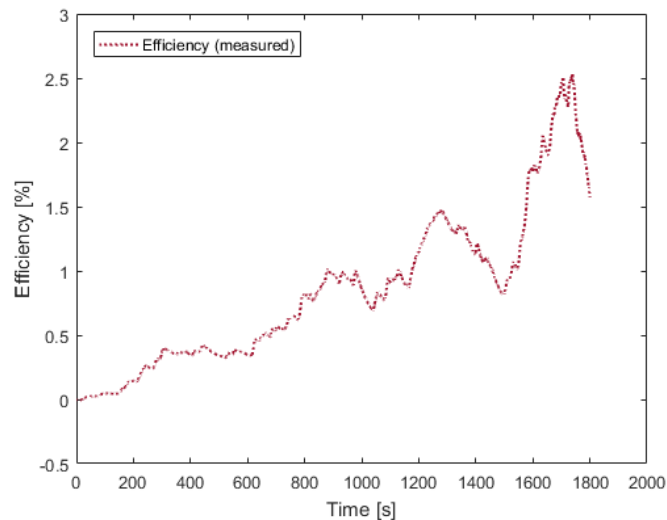


Figure 57: TEG module efficiency for the WLTC cycle

Figure 57 displays the efficiency of the thermoelectric modules, which is defined as the ratio of the generated electric power to the thermal power through the module. The thermal power through the module is calculated according to Eq. (0) and Eq. (0). The efficiency is found to be positively correlated to the temperature difference between the hot and cold side of the module. The efficiency is in particular low when the temperature difference is below a certain threshold, as shown in the first half of the cycle. The highest efficiency is found right before the last deceleration phase in the WLTC, peaking at 2.5%. Here again it becomes clear, that the WLTC, although adopted by the automotive industry, is a very unfavorable test protocol for thermoelectrics, as the high temperatures are only reached during the last phase.

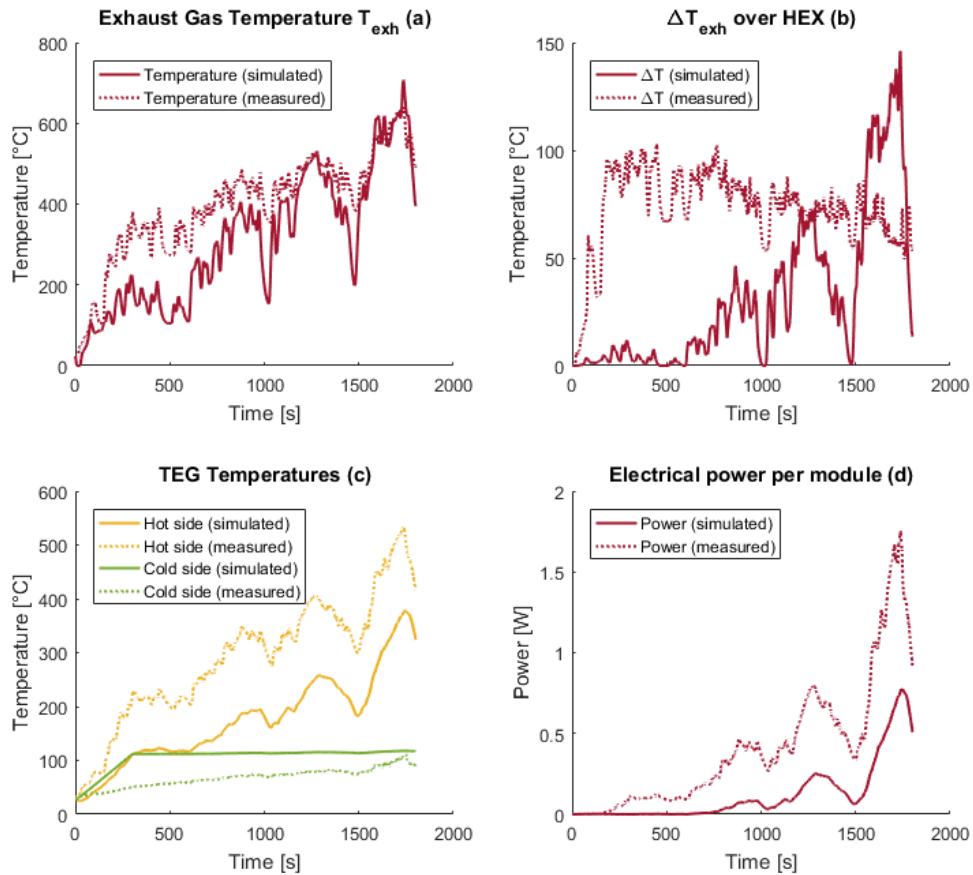


Figure 58: Comparison of the thermoelectric module performances to the simulations from section 3.2

The simulation and experimental results for a TEG system downstream the ATS of the gasoline 2.0 l car during a WLTC are presented in Fig. 58. The results show that the thermoelectric modules performs, in general, as expected. Nevertheless, deviations from the simulations were noticed. As displayed in Fig. 58a, the exhaust gas temperatures are very low at the beginning of the cycle, but increase with the engine load. This effect is less pronounced in the real experiments. It has been previously reported²⁴ that the simulation models perform best under stationary conditions and less adequate during transient periods. In particular, the heating-up of the heat exchanger part is not included in the simulations. This can be noted in Fig. 58a, where there is a clear discrepancy in the first 500 s of the WLTC. After the exhaust gas system has been brought to operating temperature, the simulation corresponds very well to the measured results. The same phenomenon can be used to explain Fig. 58b, where the temperature loss over the heat exchanger varies strongly between the simulated and measured values. In Fig. 58c, the better response of experiments compared to simulations is attributed to two effects: firstly, the introduction of fins in the exhaust gas pipe has significantly improved the heat transfer efficiency. Secondly, the higher exhaust gas temperature itself implies an increase as well. In the simulations, the strong heat transfer of the thermoelectric modules to the cooling water leads to temperatures of the modules' cold side almost equal to the cooling water. Although the cold side of the modules has a lower temperature than simulated due to a lower influx temperature of the cooling water (50 °C in the experiments vs. 100 °C in the simulations). In fact, the actual temperature difference between cooling water and the cold side of the modules was slightly higher in the measurements than in the simulations.



4.3 Comparison of performance of thermoelectric system integrated into exhaust manifold and downstream of exhaust manifold

Table 16: Comparison of output power of Half-Heusler modules integrated into the exhaust manifold and downstream of exhaust manifold

	Integrated into exhaust gas manifold (best module)			Integrated downstream of exhaust gas manifold (average over modules)		
	100 km/h	WLTC average	WLTC peak	100 km/h	WLTC average	WLTC peak
Output power [W]	1.1	0.8	2.4	1.45*	0.43**	2.2**

*corrected for temperature reduction in exhaust gas due to additional piping

**not corrected for temperature reduction in exhaust gas due to additional piping, values will be higher if correction is applied.

At constant vehicle speed of 100 km/h, the thermoelectric modules deliver a mean power of 1.1 W per module when integrated at the manifold, and 1.45 W (corrected for additional length of piping) when integrated downstream of the exhaust gas manifold. In general, exhaust gas temperatures are higher at the manifold, so this result is somewhat unexpected. However, the substantially higher steady-state performance of the thermoelectric module downstream of the exhaust gas manifold can be attributed to the much better heat transfer by the fins protruding into the exhaust gas channel and the use of copper as heat transfer medium. This indicates a potential for improving the thermal design of the exhaust manifold. This will increase the hot side temperature seen by the thermoelectric modules, and consequently leads to higher electric power output. When measured over the WLTC, the average power output delivered by the modules mounted onto the manifold is almost twice as high as the power output delivered by the modules mounted onto the heat exchanger downstream of the manifold, while peak power values reached at the end of the WLTC are comparable. This can be partially explained by the higher thermal inertia for the system mounted downstream of the manifold, as it takes longer to heat up parts further away from the engine, in particular also due to additional piping that was introduced to facilitate mounting. Note however that the data measured for the thermoelectric modules mounted after the exhaust after-treatment system over the WLTC was not corrected for the additional piping that was introduced for practical reasons (caused a temperature drop of 125°C at 100 km/h steady-state, but more detailed analysis is required to correct the transient WLTC data).

Under the hypothesis that the installation of the thermoelectric modules does not additionally burden the overall energy balance (of the engine and the vehicle), a simple assessment can deliver fuel consumption. Based on the obtained results, the energy recuperated by ten thermoelectric Half-Heusler modules when integrated downstream of the exhaust gas manifold over the WLTC cycle is 7.5 kJ (Task 4.2). Without the thermoelectric modules this energy would be generated by the alternator installed on the engine belt having a rather low efficiency (30% conversion from fuel to mechanical power, and another 50% for conversion from mechanical power to electricity). Thus the thermal energy saved with the thermoelectric modules is roughly 50 kJ. During the WLTC, the vehicle consumes roughly 1.5 kg of compressed natural gas (CNG) fuel, corresponding to a fuel energy of 69.7 MJ. This leads to a fuel consumption saving with ten thermoelectric modules of approximately 0.1%. Should only the high load part be taken into account, then the fuel savings are higher. As shown in Fig. 53 and 56, and summarized in Tab. 16, the peak power in the high load area reaches values in excess of 2 W for a single module, thus 20 W for ten modules, which leads to an energy recuperation with ten modules of 10 Wh or 36 kJ during 30 min. In this case, the thermal energy saved amounts to 206 kJ. Assuming a total fuel energy consumption of 50 MJ, the fuel saving potential is about 0.5%.

It is important to emphasize, that these values are determined for only ten installed modules and higher values are expected for additional modules or larger area modules installed into the heat exchanger, e.g. also in the vertical walls of the heat exchanger assembly. The temperature drop along the heat exchanger will increase in this case as more thermal energy is extracted. In addition,



integrating the best thermoelectric Half-Heusler materials reported in literature into the modules as discussed in Fig. 26, an additional increase in power output of 30-40% can be expected. Note again, that the estimation above used output values that were not corrected for the additional piping that was introduced for practical reasons.

We would also point out again that the relatively short Worldwide Harmonized Light Vehicles Test Cycle (WLTC) (30 min transient profile starting from cold start) is a very unfavorable testing protocol for thermoelectric generators or any waste heat recovery system as system temperatures never reach steady-state conditions. Waste heat recovery system would immediately benefit from conditions reflecting long-distance operation. While the transient WLTC cycle was developed by the UN ECE GRPE (Working Party on Pollution and Energy) for light vehicles, steady-state engine dynamometer cycles exist for heavy-duty vehicles, such as the World Harmonized Stationary Cycle (WHSC) which prescribes an engine preconditioning step before the start of the cycle (hot start).

Outlook

The present project managed to establish within a relatively short project time of 2 years a first bridge between materials science and vehicle integration. The project consortium consisted of partners that provided both a market push (materials science perspective) and a market pull dynamics (automotive OEM product development perspective). It is a challenge to bridge these two perspectives in such a small project, especially because additional industrial partners with complementary competences at intermediate stages of the product value chain would be necessary to map out a complete roadmap and techno-economic analysis for product development. In particular additional industrial partners on the level of scaling of materials synthesis, milling, and sintering, leg cutting and polishing as well as scaling of module assembly would be necessary to provide modules in sufficient numbers to design and build a full-scale product demonstrator. During the project duration, Empa established several national and international contacts to such entities, which are interested to enter the field, provided that a full value chain exists, i.e. customer entity for each successive intermediate product. Negotiating the legal framework for handling intellectual property for such a potentially trans-European or even transcontinental project becomes a substantial additional challenge.

While outcomes of the project on the level of materials science and overall energy assessment are published in scientific journals and were presented at international scientific conferences, results on module level are under consideration for a patent publication. Yet another outcome of the project are the numerical modelling tools, which are of interest to several industrial entities, to match module performance to a given heat exchanger environment. Ideally also the properties of the heat exchanger are modelled as in this project. But as these calculations were performed on different numerical platforms and by different partners of the project consortium, it is not straightforward to integrate both components into a single stand-alone modelling tool.



Acknowledgements

We thank the Swiss Federal Office of Energy for financial support of this project, Dr. Lukas Martin, ETH Zürich, Institute for Geochemistry and Petrology for support in electron probe microanalysis, the group of Dr. Christian Leinenbach, Empa Dübendorf, Advanced Materials Processing Lab, for making available the arc melting furnace in the initial phase of the project, Dr. Hans Rudolf Elsener, Empa Dübendorf, Joining Technology and Corrosion Lab, for making available the vacuum furnace in the initial phase of the project and providing guidance for developing the brazing technology for Half-Heusler modules, and Prof. Jeffrey G. Snyder, Northwestern University, for stimulating discussions on the phase diagram and transport properties of Half-Heusler materials. We further thank Prof. Lidong Chen, Chinese Academy of Sciences, Shanghai Institute of Ceramics, China, for providing reference modules for our test bench, Prof. Tiejun Zhu, Zhejiang University, China for preparing samples by levitation melting synthesis, Dr. Masashi Mikami, National Institute of Advanced Industrial Science and Technology, Japan, for reference materials data, and Prof. Yoichi Nishino, Nagoya Institute of Technology, Japan, for reference materials.

References

- 1 Culp, S. R., Poon, S. J., Hickman, N., Tritt, T. M. & Blumm, J. Effect of substitutions on the thermoelectric figure of merit of half-Heusler phases at 800 °C. *Applied Physics Letters* **88**, 042106, doi:10.1063/1.2168019 (2006).
- 2 Yu, C. *et al.* High-performance half-Heusler thermoelectric materials $\text{Hf}_{1-x}\text{Zr}_x\text{NiSn}_{1-y}\text{Sb}_y$ prepared by levitation melting and spark plasma sintering. *Acta Materialia* **57**, 2757-2764, doi:10.1016/j.actamat.2009.02.026 (2009).
- 3 Schwall, M. & Balke, B. Phase separation as a key to a thermoelectric high efficiency. *Physical chemistry chemical physics* **15**, 1868-1872, doi:10.1039/c2cp43946h (2013).
- 4 Kimura, Y. & Zama, A. Thermoelectric properties of p-type half-Heusler compound HfPtSn and improvement for high-performance by Ir and Co additions. *Applied Physics Letters* **89**, 172110, doi:10.1063/1.2364721 (2006).
- 5 Culp, S. R. *et al.* (Zr,Hf)Co(Sb,Sn) half-Heusler phases as high-temperature (>700 °C) p-type thermoelectric materials. *Applied Physics Letters* **93**, 022105, doi:10.1063/1.2959103 (2008).
- 6 Fu, C. *et al.* High Band Degeneracy Contributes to High Thermoelectric Performance in p-Type Half-Heusler Compounds. *Advanced Energy Materials* **4**, 600, doi:10.1002/aenm.201400600 (2014).
- 7 Fu, C., Zhu, T., Liu, Y., Xie, H. & Zhao, X. Band engineering of high performance p-type FeNbSb based half-Heusler thermoelectric materials for figure of merit $zT > 1$. *Energy Environ. Sci.* **8**, 216-220, doi:10.1039/c4ee03042g (2015).
- 8 *Mineral Commodity Summary 2016*, <<http://minerals.usgs.gov/minerals/pubs/mcs/2016/mcs2016.pdf>> (2016).
- 9 Gürth, M. *et al.* On the constitution and thermodynamic modelling of the system Ti–Ni–Sn. *RSC Adv.* **5**, 92270-92291, doi:10.1039/c5ra16074j (2015).
- 10 Sakurada, S. & Shutoh, N. Effect of Ti substitution on the thermoelectric properties of (Zr,Hf)NiSn half-Heusler compounds. *Applied Physics Letters* **86**, 082105, doi:10.1063/1.1868063 (2005).
- 11 Schwall, M. & Balke, B. Phase separation as a key to a thermoelectric high efficiency. *Physical chemistry chemical physics* : PCCP **15**, 1868-1872, doi:10.1039/c2cp43946h (2013).
- 12 Gürth, M. *et al.* On the constitution and thermodynamic modelling of the system Ti–Ni–Sn. *RSC Adv.* **5**, 92270-92291, doi:10.1039/c5ra16074j (2015).
- 13 Downie, R. A., MacLaren, D. A., Smith, R. I. & Bos, J. W. Enhanced thermoelectric performance in TiNiSn-based half-Heuslers. *Chem Commun (Camb)* **49**, 4184-4186, doi:10.1039/c2cc37121a (2013).



- 14 Xie, H.-H. et al. Interrelation between atomic switching disorder and thermoelectric properties of ZrNiSn half-Heusler compounds. *CrystEngComm* 14, 4467, doi:10.1039/c2ce25119a (2012).
- 15 Kim, S.-W., Kimura, Y. & Mishima, Y. High temperature thermoelectric properties of TiNiSn-based half-Heusler compounds. *Intermetallics* 15, 349-356, doi:10.1016/j.intermet.2006.08.008 (2007).
- 16 Goldsmid, H. J. & Sharp, J. W. Estimation of the Thermal Band Gap of a Semiconductor from Seebeck Measurements. *Journal of Electronic Materials* 28, 869-872 (1999).
- 17 Wang, H., Pei, Y., LaLonde, A. D. & Jeffery Snyder, G. in *Thermoelectrics Nanomaterials Vol. 182* (eds K. Koumoto & T. Mori) 3-32 (Springer, 2013).
- 18 Xie, H. et al. The intrinsic disorder related alloy scattering in ZrNiSn half-Heusler thermoelectric materials. *Scientific reports* 4, 6888, doi:10.1038/srep06888 (2014).
- 19 Kim, H.-S., Gibbs, Z. M., Tang, Y., Wang, H. & Snyder, G. J. Characterization of Lorenz number with Seebeck coefficient measurement. *APL Materials* 3, 041506, doi:10.1063/1.4908244 (2015).
- 20 Hazama, H., Matsubara, M., Asahi, R. & Takeuchi, T. Improvement of thermoelectric properties for half-Heusler TiNiSn by interstitial Ni defects. *Journal of Applied Physics* 110, 063710, doi:10.1063/1.3633518 (2011).
- 21 C. Fu, S. Bai, Y. Liu, Y. Tang, L. Chen, Y. Zhao, and T. Zhu. Realizing high figure of merit in heavy-band p-type half-Heusler thermoelectric materials. *Nat. Comm.* 6, 8144 (2015).
- 22 Kim, H.-S., Liu, W., Chen, G., Chu, C.-W. & Ren, Z., Relationship between thermoelectric figure of merit and energy conversion efficiency. *Proceedings of the National Academy of Sciences of the United States of America* 112, 8205-8210, doi:10.1073/pnas.1510231112
- 23 Battaglia, C., Widmer, R., Helbling, T., Hug, L., Miller, B., Neumann, W., Götze, M., Sägesser, C., Dubois, Y., Potential of Thermoelectrics for Waste Heat Recovery, SFOE project report SI/501211, <https://www.aramis.admin.ch/Texte/?ProjectID=36371>, (2016)
- 24 Durand, T.; Dimopoulos Eggenschwiler, P., Tang, Y., Liao Y., Landmann D., Potential of energy recuperation in the exhaust gas of state of the art light duty vehicles with thermoelectric elements, *Fuels* 224, 271 (2018).
- 25 Frank P. Incropera, David P. DeWitt, Bergman, T. L. & Lavine, A. S. *Fundamentals of Heat and Mass Transfer*. 6th edn, (2006).